Dissertation

submitted to the

Combined Faculties for the Natural Sciences and for Mathematics

of Ruperto-Carola-University of Heidelberg, Germany

for the degree of

Doctor of Natural Sciences

presented by

M.-Sc. Xuewei Cao

born in : Tianjin, P. R. CHINA

Oral examination: Dec 7, 2004

Low-frequency elastic properties
of glasses at low temperatures

——

Investigations with double-paddle oscillators
based on a dc-SQUID readout

Referees: Prof. Dr. Siegfried Hunklinger
           Prof. Dr. Heinz Horner

Within this thesis low frequency measurements on the elastic properties of amorphous solids (a-SiO$_2$ and BK7) at low temperatures using mechanical oscillators were carried out. A main aspect was to develop a novel detection technique for double-paddle oscillators within the environment of a dilution refrigerator. The inductive detection mechanism is based on the high sensitivity of a commercial dc-SQUID. The superiority of the new technique compared to the conventional capacitive detection method was demonstrated in measurements on different glass samples. The resolution was improved more than one order of magnitude already in these first experiments. Using the new technique, the relative change of sound velocity and the internal friction of a-SiO$_2$ and BK7 were investigated in the temperature range form $5\,\mathrm{mK}$ to about $1\,\mathrm{K}$ for several frequencies. The results agree favourably with former measurements on a-SiO$_2$ detected by the capacitive readout. For BK7 slight deviations to former measurements at lowest temperatures were observed.

Niederfrequente elastische Eigenschaften von Gläsern bei tiefen Temperaturen — Untersuchungen mittels mechanischer Double Paddle Oszillatoren und einer auf dc-SQUIDs basierenden Auslesetechnik

Im Rahmen dieser Arbeit wurden niederfrequente Messungen der elastischen Eigenschaften von Gläsern (Quarzglas und BK7) bei tiefen Temperaturen mittels mechanischer Oszillatoren durchgeführt. Hauptschwerpunkt lag hierbei auf der experimentellen Entwicklung einer neuartigen Auslesetechnik für sogenannte Double Paddle Oszillatoren innerhalb eines Verdünnungskryostaten. Der induktive Detektionsmechanismus basiert hierbei auf der hohen Sensitivität von kommerziell erhältlichen dc-SQUIDs. Die Überlegenheit dieser Technik gegenüber der konventionellen kapazitiven Methode wurde durch Messungen an verschiedenen Gläsern demonstriert. Bereits in diesen ersten Messungen konnte die Sensitivität um mehr als eine Größenordnung gegenüber der kapazitiven Technik verbessert werden. Mit Hilfe des neuen Detektionsmechanismus wurden die relative Schallgeschwindigkeitsänderung und die innere Reibung von amorphem SiO$_2$ und BK7 im Temperaturbereich zwischen $5\,\mathrm{mK}$ und $1\,\mathrm{K}$ für mehrere Frequenzen untersucht. Die Ergebnisse an Quarzglas stehen in guter Übereinstimmung mit konventionell durchgeführten Messungen, während für BK7 leichte Abweichungen zu früheren Messungen bei tiefsten Temperaturen beobachtet wurden.

Table of contents

1.   Introduction

Glass was used by man for several thousand years. Nowadays it is used in many fields, such as research, engineering and daily living. The investigation of the properties of these disordered solids is still a topic of growing scientific and technological interest. In the last decades numerous experiments have shown that in particular several low temperature properties of amorphous materials differ significantly from those of pure crystals. The experimental findings of thermal, acoustic and dielectric measurements on glasses below 1 K can be attributed to low-energy excitations due to the irregular structural configurations in this material [Phi81, And72].

A successful theoretical approach to describe the low temperature properties is the so-called standard tunneling model. The model is based on phenomenological assumptions: in disordered solids some atoms or groups of atoms can have several structural configurations which are energetically slightly different from each other. The energetic minima are separated by a potential barrier. At low temperatures the potential barrier cannot be overcome by thermally activated processes. However a transfer from one potential minimum to the other can take place by quantum mechanical tunneling through the barrier. Therefore these systems are called "Tunneling Systems". Disordered solids exhibit a variety of different structural configurations. This leads to the assumption that also the energy splittings are widely distributed. From the assumptions of the standard tunneling model one can deduce predictions on dielectric and elastic properties of the amorphous solid under consideration. In particular, the temperature and frequency dependence of the elastic properties relative change of sound velocity $\delta v/v$ and the internal friction Q^{-1} is given.

First indications for deviations from the expected behaviour resulted from low-frequency dielectric measurements on the borosilicate glass BK7 [Ens89]. Due to the similar behaviour of dielectric and elastic properties experiments with mechanical oscillators were subsequently carried out. In vibrating reed studies on a-SiO$_2$ of Classen *et al.* [Cla91] clear deviations from the standard tunneling model were found. It turned out that a general problem in these experiments is the occurence of nonlinear effects caused by the tunneling systems. When the oscillator is driven at too high excitation levels, i.e. when the strain energy becomes of the order of the thermal energy, the acoustic response becomes nonlinear.

Within this topic many questions still require a further clarification, e.g.: Does one observe deviations from the prediction of the standard tunneling model, which were found experimentally in the elastic properties of quartz glass, also in the other glasses? Are these deviations more or less pronounced in other glasses? Do we find a universal behaviour for the elastic properties of glasses at low temperatures? If yes, where does this behaviour come from? What is the microscopic nature of tunneling systems?

For the closer analysis of these questions, two different glasses were used to measure

the acoustic properties at low temperatures. To enhance the sensitivity and thus to allow measurements at lower excitation amplitudes we have set up a new inductive detection technique for double-paddle oscillators based on a commercial dc-SQUID. The application of SQUIDs is an established approach to detect very small displacements in magnetic fields. They are already used for example in gravitational wave detectors or in measurements of the redshift of γ-radiation in the gravitational field of the earth using Moessbauer spectroscopy.

To compare the novel detection technique to the conventional one, a sample holder is set up which enables us to carry out measurements with double-paddle oscillators and both readout techniques: conventional capacitive technique and inductive readout based on a dc-SQUID.

As first sample amorphous SiO_2 was chosen. For this material measurements on the elastic properties were carried out with the conventional technique over a wide range of frequencies serveral years ago. Therefore a comparison from the experimental results to previous measurements is possible. The second sample is BK7, a standard glass which is widely used in optics. In former measurements slight deviations to a-SiO_2 were observed at lowest temperatures, which could be interpreted as an additional relaxation mechanism, due to the mutual interaction of two-level systems.

In chapter 2 the main assumptions and predictions of the standard tunneling model as well as of some enhanced theoretical approaches are introduced. Chapter 3 contains the description of different mechanical oscillators, in particular the geometry of the double-paddle oscillator. Chapter 4 gives an overview over fundamental methods and the techniques used in our experiments. In chapter 5 the novel developed inductive readout technique for double-paddle oscillator is presented, characterized and compared to the conventional capacitive measurement. First results with this novel technique on the temperature dependence of the elastic properties of two amorphous samples (a-SiO_2 and BK7) below 1 K are presented in chapter 6. In chapter 7 a brief conclusion of the experimental results and an outlook on future experiments is given.

2. Tunneling systems in amorphous solids

In this chapter an introduction to experimental findings and the theoretical background on the low-temperature properties of glasses is presented. At first an overview over some experimental observations is given. These findings can be described by a theoretical model, the so-called "standard tunneling model" (STM). The assumptions and predictions of this phenomenological description are introduced in the following. In the last part of this chapter, measurements on acoustic properties of glasses are presented and compared to the theoretical results. The deviations from experiment and theory give rise to extensions of the standard tunneling model, which are discussed.

2.1 Low temperature properties of glasses

2.1.1 Thermal properties

Specific heat

From the beginning of last century the thermal properties of crystalline solids have already been well understood. According to the Debye model [Deb12], the temperature dependence of the phononic specific heat C_V of a dielectric crystal can be described with only one material parameter, the Debye temperature Θ. In particular, the T^3-dependence of the specific heat at low temperatures is correctly predicted.

As the Debye model describes a solid within an isotopic continuum approximation, it
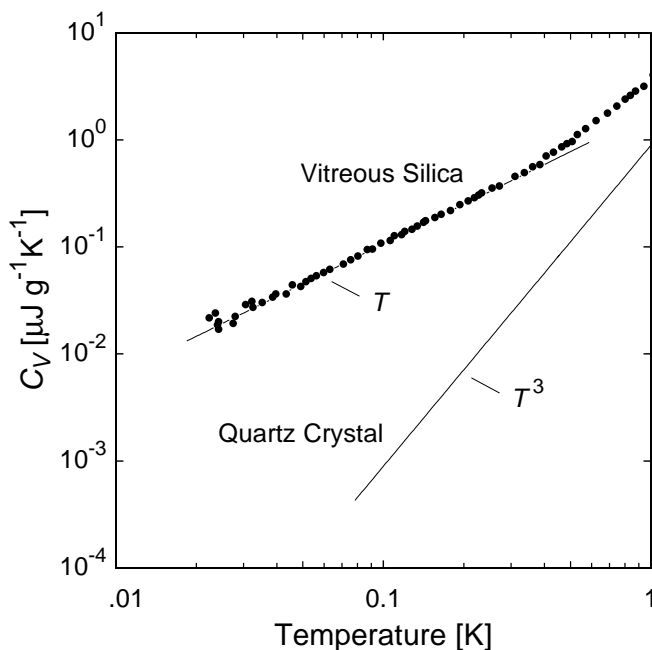
Fig. 2.1: Specific heat of crystalline SiO$_2$ and of vitreous silica below 1 K. Over the whole temperature range the specific heat of the glass is larger than that of the crystal [Hun77].

3

should be also valid for the vibration of disordered solids at low temperature. So disordered
solids should show a similar behaviour for the low-temperature properties.

In 1971, however, a big surprise for many solid state physicists was found by Zeller and
Pohl [Zel71]. The specific heat of the disordered solids shows a behaviour different to the
one of crystals.

Figure 2.1 shows the specific heat for crystalline and amorphous SiO_2 (vitreous silica)
as a function of temperature. The heat capacity of the quartz crystal coincides with T^3 law
as predicted by the Debye model. The specific heat of the vitreous silica is proportional to
the temperature below 500 mK. The absolute value of the specific heat in the amorphous
specimen is well above the one of its crystalline counterpart. The difference is about three
orders of magnitude at 25 mK. This suggests that vitreous silica contains additional low-
energy excitations, which contribute significantly to heat capacity of amorphous solids.

Thermal conductivity

By applying the kinetic theory of gases to the phonon system and assuming a gaslike
interaction between the phonons, the thermal conductivity can be described as

$$\Lambda = \frac{1}{3} \, C_{\mathrm{V}} \, vl. \tag{2.1}$$

C_{V} is the specific heat of the phonon gas per volume, v is the average sound velocity,
and l is the mean free path of the thermal phonons, which is determined by the relevant
scattering processes.

The measurements of the thermal conductivity of quartz crystals and vitreous silica are
shown in figure 2.2. For quartz crystal the phonon scattering is mainly due to the phonon-
phonon interaction in the high temperature limit. The number of phonons and their
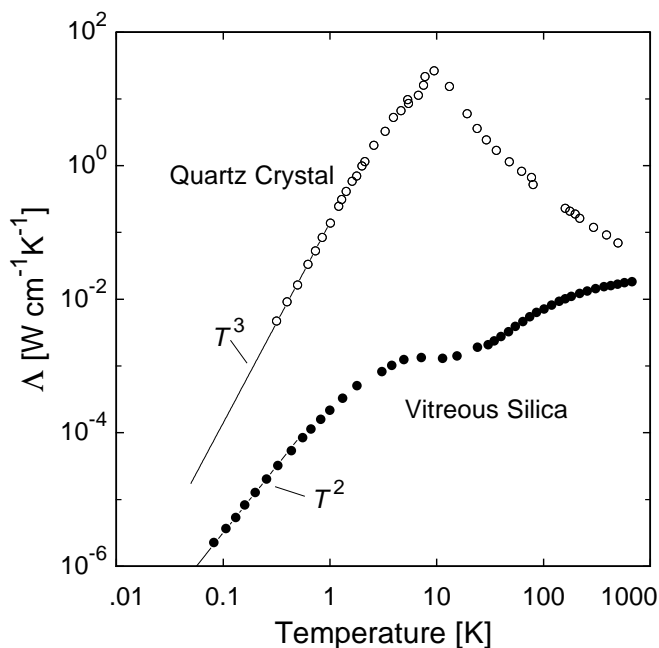
Fig. 2.2: Thermal conductivity of crystalline SiO_2 and of vitreous silica [Zel71].

scattering rate decreases with temperature, resulting in an increasing mean free path. From (2.1) we find an increase in thermal conductivity. With decreasing temperature, thermal conductivity passes through a maximum and decreases afterwards. In the temperature region below the maximum, the so-called Casimir regime, the mean free path l of the phonons becomes so large that it is essentially limited by the scattering at the surfaces of the specimen. So l becomes constant. As the sound velocity v is also constant in this temperature region, the thermal conductivity is proportional to T^3, following the specific heat.

As the Debye model describes a solid within an isotropic continuum approximation, it should be also valid for disordered solids at low temperature. So amorphous materials should show similar low-temperature properties.

The measurements of the thermal conductivity of quartz crystal and vitreous silica are shown in figure 2.2. Over the whole temperature range, the thermal conductivity of the amorphous material is much smaller than the one of its crystalline counterpart. Below 1 K, the thermal conductivity in vitreous silica is roughly proportional to T^2.

The reduction of the thermal conductivity compared to crystalline materials indicates that glasses contain additional scattering mechanisms for phonons which are not present in crystalline materials. These localized low-energy excitations limit the mean free path of phonons [Zel71].

2.1.2   Acoustic properties

Figure 2.3 shows the ultrasonic absorption of the borosilicate glass (BK 7) as a function of the acoustic intensity at 0.48 K. When the acoustic attenuation is small ($< 10^{-7}\mathrm{W/cm^2}$),
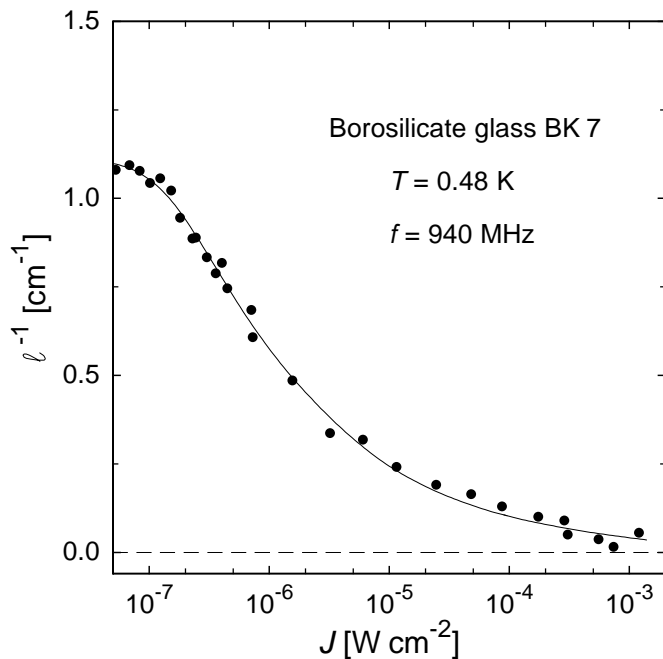
Fig. 2.3: Ultrasonic absorption ℓ^{-1} in borosilicate glass (BK 7) as function of acoustic intensity J at 0.48 K. The solid line is the prediction of the tunneling model [Hun74].

absorption takes place. With increasing acoustic attenuation the ultrasonic absorption l^{-1} decreases and vanishes [Hun74]. This behaviour is due to the resonant interaction of two-level systems and phonons. The occupation number difference of an ensemble of two-level systems in thermodynamical equilibrium is given by

$$\Delta N = N \tanh \frac{E}{2k_{\mathrm{B}}T}, \tag{2.2}$$

where E is the energy splitting of the two-level system, k_{B} is Boltzmann constant and N is the number of two-level system. This equation is nearly fulfilled for small intensities, since resonant absorption can take place when two-level systems are in the ground state. With increasing intensity the two-level systems are not in thermal equilibrium any more. And (2.2) is fulfilled no longer. An increasing number of two-level systems are excited, so that the ground state and the excited state are equally populated finally. The equilibrium of the absorption and the stimulated emission can be reached – the ultrasonic absorption is saturated. This result proofs that the low-energy excitations in glasses can be considered as two-level systems.

2.2 Standard tunneling model

2.2.1 Double well potential

After Zeller and Pohl published their results on the low temperature thermal anomalies of glasses, within the next three years about ten different models were proposed to explain these discoveries [Phi81]. The most successful model among them was the one by Anderson, Halperin, and Varma [And72] and independently by Phillips [Phi72]. It was later named "Standard Tunneling Model" (STM).

The standard tunneling model is phenomenological, based on the assumption that some atoms or groups of atoms in disordered solids have two or even more potential minima, in contrast to crystals, in which the atoms have a single energy minimum. At low temperature, though the atoms or groups of atoms can't overcome the barrier between the two potential minima by thermal activation, they still can reach another potential minimum through the barrier by quantum mechanical tunneling. The wide spectrum of different configations present in disordered solids gives rise to a wide range of possible energy differences.

In figure 2.4 a possible two-dimensional schematic of the structure of amorphous SiO_2 is shown. Compared to crystalline SiO_2, the number of atoms per ring are different and the binding angles are also slightly different. In particular there are pentagonal rings and heptagonal rings. The behaviour of a glass of low temperature is based on the assumption that the localized structural defects can occupy different configurations. In figure 2.4 three different localized structural defects are indicated by A, B and C: a transverse motion (A) [And55], a longitudinal motion (B) [Str61] and a rotation of the oxygen atoms around a certain axis of one silicon atom in a small angle (C) [Vuk72].
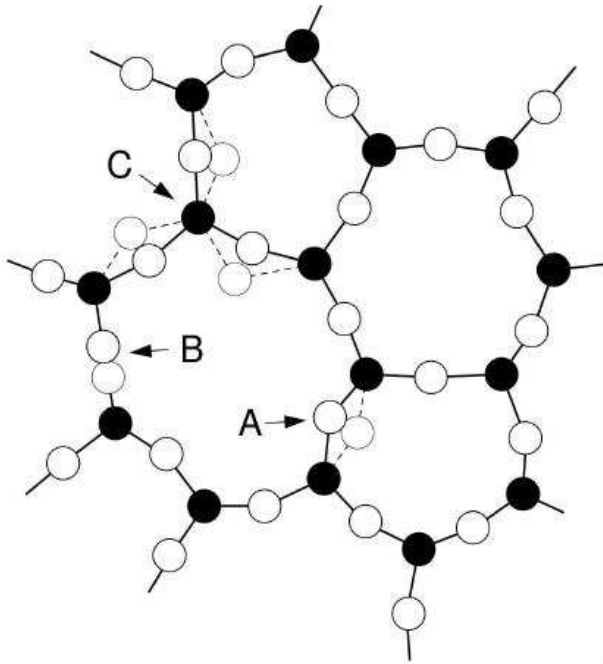
Fig. 2.4: Two-dimensional schematics of the structure of amorphous SiO_2. The full circles represent the silicon atoms, while the oxygen atoms are drawn as open circles. The configurations A, B and C are examples for the system where single atoms may occupy two nearly equivalent equilibrium positions [Hun76].

These configurations can be described phenomenologically by assuming an energy landscape of the form of a double-well potential. In figure 2.5 the potential energy created by the surrounding atoms is shown as a function of a general configuration coordinate. The double-well potential is consisting of two harmonic potentials, separated by a potential barrier. d is the distance between the two wells with regard to this coordinate, m is an effective mass of the particle moving in the double-well potential, and V denotes the height of the barrier between the two minima. As the arrangement of atoms in different configurations is not entirely same, the minima of the single harmonic potentials will in general have a potential difference called asymmetry energy Δ.

$\hbar\Omega/2$ is the energy of the particle at the ground state. Ψ_a and Ψ_b are the wave functions of the ground states of the particle in the left and right well, respectively. Below 1 K only
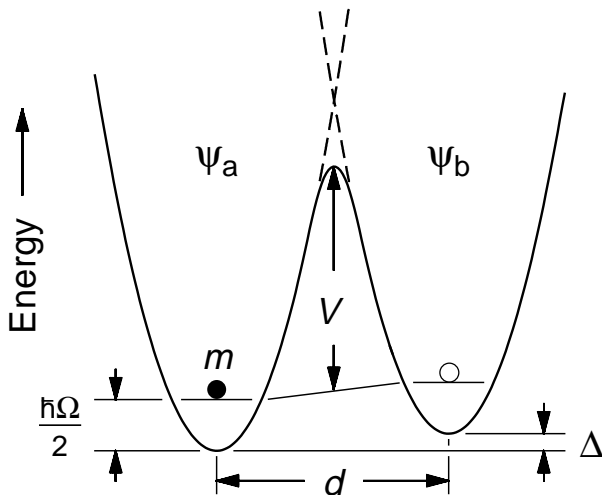
Fig. 2.5: Schematics of a double-well potential. The ground state energy of either single well is $\hbar\Omega/2$. Δ is the asymmetry energy, d the distance between the wells, and V the height of the potential barrier.

the ground states $|\Psi_a\rangle$ and $|\Psi_b\rangle$ can be occupied, because the first excited state is seperated from the ground state by an energy of the order of 10 K. Moreover, the transitions from one well to the other via thermal activation are extremely improbable. As mensioned before, the transitions can take place only by quantum mechanical tunneling processes through the potential barrier. Systems that can be described by a particle in a double-well potential will be called "Tunneling System" (TS).

In the following section the focus lies on a quantum mechanical description of the dynamics of the particle in such a double-well potential. To determine the wave functions and eigenenergies of a system, the stationary Schroedinger equation

$$H\Psi = E\Psi \tag{2.3}$$

has to be solved. Ψ is the wave function of the particle in the double-well potential. H is the Hamiltonian, E is the eigenvalue of the system.

For the ground state, Ψ can be written as a linear superposition of Ψ_a and Ψ_b:

$$\Psi = a\Psi_a + b\Psi_b. \tag{2.4}$$

If we use Ψ_a and Ψ_b as basis, the Hamiltonian governing the dynamics of a system with a double-well potential is

$$H_0 = \frac{1}{2}\begin{pmatrix} \Delta & -\Delta_0 \\ -\Delta_0 & -\Delta \end{pmatrix} \tag{2.5}$$

Δ_0 is the energy splitting due to the tunneling motion. This nondiagonal elements in the matrix indicate the overlap of Ψ_a and Ψ_b, which cause the tunneling of the particle between the two potential minima.

By the diagonalisation

$$H_0' = \frac{1}{2}\begin{pmatrix} E & 0 \\ 0 & -E \end{pmatrix} \tag{2.6}$$

one gets the ground state energy splitting

$$E = \sqrt{\Delta^2 + \Delta_0^2} \tag{2.7}$$

Using the Wentzel-Kramers-Brillouin (WKB) approximation, it is possible to express Δ_0 in terms of the so-called tunneling parameter λ

$$\Delta_0 = \hbar\Omega\,\mathrm{e}^{-\lambda}, \tag{2.8}$$

which can be expressed as

$$\lambda = \frac{d}{2\hbar}\sqrt{2mV}\,, \tag{2.9}$$

and involves three characteristic parameters of double-well potential, which are effective mass of the particle m, height of the potential barrier V and the distance of the wells d.

2.2.2 Tunneling systems in glasses

In a disordered solid the characteristic parameters Δ and λ of a tunneling system have a broad distribution due to its irregular structure. In the standard tunneling model the tunneling parameter λ and the asymmetry energy Δ are assumed to be independent of each other having a uniform distribution

$$P(\Delta, \lambda)\, d\Delta\, d\lambda = \overline{P}\, d\Delta\, d\lambda\,, \tag{2.10}$$

with a characteristic constant value $\overline{P}$ for each glass.

By using (2.7) and (2.8) one can define a new variable

$$u = \Delta_0/E\ . \tag{2.11}$$

Thus, the distribution function P can be expressed as functions of E and u:

$$P(E, u)\, \mathrm{d}E\, \mathrm{d}u = \frac{\overline{P}}{u\sqrt{1 - u^2}}\, \mathrm{d}E\, \mathrm{d}u\ . \tag{2.12}$$

Figure 2.6 shows a plot of the distribution function $P(E, u)$.
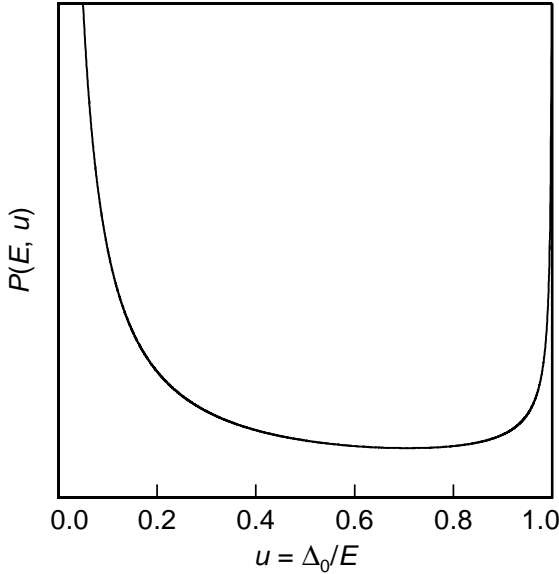
Fig. 2.6: Distribution function $P(E, u)$ as function of $u = \Delta_0/E$

The distribution function is not integrable at $u = 0$. Considering the finite number of two-level systems per unit volume of the sample, $u = u_{\min}$ as the low limit is reasonable. The assumption $u = u_{\min}$ implies a minimum tunneling energy splitting $\Delta_{0,\min}$. So the density of states for tunneling systems is

$$D(E) = \int_{\Delta_{0,\min}}^{\infty} P(E, \Delta_0)\, \mathrm{d}\Delta_0 = \overline{P}\ln\left(\frac{2E}{\Delta_{0,\min}}\right)\,, \tag{2.13}$$

Due to the weak logarithmic dependance on the energy splitting, $D(E)$ is nearly constant. This results in a linear temperature dependence of the specific heat which fits the experimental observation of section 2.1.1.

2.2.3   Interaction of TLSs with phonons

Tunneling systems in disordered solids couple to their environment by interaction with phonons. An external elastic field changes the asymmetry energy Δ. A possible coupling to the tunneling splitting Δ_0 is usually negligible compared to the modulation of Δ [Jae72]. The variation $\delta\Delta$ in the limit of small perturbations should show a linear dependance on the elastic strain e:

$$\delta\Delta = 2\,\gamma\,\delta e \; . \tag{2.14}$$

The proportionality factor is the deformation potential γ, which represents the coupling between tunneling systems and phonons. It can be described as

$$\gamma = \frac{1}{2}\frac{\partial\Delta}{\partial e}. \tag{2.15}$$

Both variables (γ and e) are in general tensors. For simplification, they are considered as scalar quantities.

In the basis of single well states $|\Psi_\mathrm{a}\rangle$ and $|\Psi_\mathrm{b}\rangle$ the following perturbation Hamilton operator is defined for the coupling between phonons and tunneling systems:

$$H_\mathrm{d} = \begin{pmatrix} 1 & 0 \\ 0 & -1 \end{pmatrix} \gamma e \; . \tag{2.16}$$

Transforming this operator to the basis of energy representation, which results from the linear superposition of the initial states $|\Psi_\mathrm{a}\rangle$ and $|\Psi_\mathrm{b}\rangle$, one gets:

$$H_\mathrm{d}' = \frac{1}{E}\begin{pmatrix} \Delta & -\Delta_0 \\ -\Delta_0 & -\Delta \end{pmatrix} \gamma e \; . \tag{2.17}$$

The diagonal elements of H_d' describe the energy shift of the energy splitting due to the perturbation field, while the off-diagonal elements describe the coupling for resonant interaction between the two-level systems and phonons.

Then the total Hamiltonian reads

$$H_\mathrm{tot} = H_0' + H_\mathrm{d}' = \frac{1}{2}\begin{pmatrix} E & 0 \\ 0 & -E \end{pmatrix} + \frac{1}{E}\begin{pmatrix} \Delta & -\Delta_0 \\ -\Delta_0 & -\Delta \end{pmatrix} \gamma e \; . \tag{2.18}$$

The operator shows a formal similarity to the Hamiltonian of a spin 1/2-particle in a static magnetic field with an additional oscillatory magnetic perturbation field. The dynamics of this system is described by the Bloch equations. Their solutions can be applied to the tunneling systems [Hun76].

Instead of the magnetic susceptibility one gets an expression for the contribution of the tunneling systems to the complex elastic susceptibility S, which are discussed in the following section.

Relaxation process

The elastic strain field e modulates the coupling to the asymmetry Δ and the energy splitting E of the two-level systems. The energy modulation δE in the case of small strain follows from (2.17)

$$\delta E = 2\gamma e \frac{\Delta}{E} \ . \tag{2.19}$$

To describe the relaxation processes one considers an ensemble of two-level system with energy splitting E in thermodynamical equilibrium. Applying a distortion to the system causes a nonequilibrium occupation. By absorption and emission of thermal phonons the tunneling systems try to reach their equilibrium occupation. If the energy splitting δE is modulated by an acoustic wave, it will lead to a continous modulation of the energy splitting. The reestablishment of thermal equilibrium takes place with a characteristic time constant τ, the so-called relaxation time. As the value of the relaxation time τ is finite, there is a phase shift between the mechanical stress σ and the elastic strain field e. Therefore one gets

$$e = S\sigma \tag{2.20}$$

with the complex susceptibility S. For simplification the tensor character of these quantities remains unconsidered. Furthermore only the contribution of the tunneling systems to the elastic coefficient is taken into account. The expression can be separated into real and imaginary part,

$$S = S' + iS''. \tag{2.21}$$

The real part S' is connected to the relative change of sound velocity $\delta v/v$ and the imaginary part S'' to the damping of the systems, the so-called internal friction Q^{-1}. Real and imaginary parts are related by the Kramers-Kronig-Relation. Two different processes contribute to $\delta v/v$ and Q^{-1}.

Considering an ensemble of two-level systems with energy splitting E, one gets the following expression for the acoustic susceptibility [Hun76]:

$$S = -\frac{4N}{\rho^2 v^4} \left(\gamma \frac{\Delta}{E}\right)^2 \frac{\partial f}{\partial E} \frac{1}{1 - i\omega\tau} \ . \tag{2.22}$$

N is the number of tunneling systems per unit volume, ρ is the density, v is the sound velocity in the amorphous solid, ω is the perturbation frequency and τ is the relaxation time of the tunneling system. In addition, the Fermi-Dirac-Distribution $f = (e^{E/k_\mathrm{B}T} + 1)^{-1}$ was used in (2.22) as abbreviation for the derivative of the occupation number difference. The denominator $(1 - i\omega\tau)$ is characteristic for the behaviour of a Debye relaxator. Using the relations

$$\frac{\delta v}{v} = -\frac{\rho v^3 S'}{2} \ , \tag{2.23}$$

and

$$Q^{-1} = \alpha \frac{v}{\omega} = \rho v^2 S'' \ , \tag{2.24}$$

with the damping $\alpha \equiv l^{-1}$, one finds for the relative change of sound velocity and the internal friction

$$\frac{\delta v}{v} = \frac{2N}{\rho v^2} \left(\gamma \frac{\Delta}{E}\right)^2 \frac{\partial f}{\partial E} \frac{1}{1 + (\omega \tau)^2} \ , \tag{2.25}$$

$$Q^{-1} = -\frac{4N}{\rho v^2} \left(\gamma \frac{\Delta}{E}\right)^2 \frac{\partial f}{\partial E} \frac{\omega \tau}{1 + (\omega \tau)^2} \ . \tag{2.26}$$

From (2.25) we can see that the main contributions of a Debye relaxator to the change of sound velocity occurs at $\omega \tau = 1$. As $Q^{-1} \propto \omega \tau \left[1 + (\omega \tau)^2\right]$ the damping reaches the maximum also at $\omega \tau = 1$.

Below 1 K the dominant process is the so-called *one-phonon-process*. In this process a transition is induced between the ground and the excited state including an emission or absorption of *one* thermal phonon. This process takes place, as the energy of the phonons in this temperature range is comparable to the energy splitting of the tunneling systems. The calculation of the relaxation rate for the one-phonon-process τ_{d}^{-1}, which is also known as *direct process*, follows from Fermi's golden rule [Jae72]

$$\tau_{\mathrm{d}}^{-1} = \frac{1}{2\pi \rho \hbar^4} \left(\frac{\gamma_{\mathrm{l}}^2}{v_{\mathrm{l}}^5} + 2\frac{\gamma_{\mathrm{t}}^2}{v_{\mathrm{t}}^5}\right) E^3 \left(\frac{\Delta_0}{E}\right)^2 \coth\left(\frac{E}{2k_{\mathrm{B}}T}\right) \ . \tag{2.27}$$

The indices l and t stand for the longitudinal and the transversal phonon branches. The temperature dependence of the relaxation rate is given by the cotangent hyperbola, which reflects the thermal occupation of the phonons. The factor E^3 is composed of two contributions, the phononic quadratic frequency dependence of the density of states following from the Debye model and the proportionality between energy splitting E and quadratic stress e. Due to the factor $(\Delta_0/E)^2$ tunneling systems with the same energy splitting E can possess very different relaxation times τ, as Δ_0 is distributed over a broad regime. From (2.27) one can see that the symmetric systems ($\Delta_0 = E$, $\Delta = 0$) are the fastest, so their relaxation time will be denoted as τ_{min}.

At higher temperatures ($T \geq 1\,\mathrm{K}$) multi-phonon processes become important, as their relaxation rate exhibits a stronger temperature dependence [Dou80]. Neglecting this relaxation channel, one can calculate the relaxation contribution of the tunneling systems to the internal friction from (2.26). To perform the calculation N has to be replaced by the integration over the characteristic parameters Δ and λ of the distribution function $P(\Delta, \lambda)$. From [Hun76] one gets

$$Q^{-1}\big|_{\mathrm{rel}} = \frac{\gamma^2}{\rho v^2} \int\limits_0^\infty \int\limits_0^\infty P(\Delta, \lambda) \left(\frac{\Delta}{E}\right)^2 \frac{1}{k_{\mathrm{B}}T} \operatorname{sech}^2\left(\frac{E}{2k_{\mathrm{B}}T}\right) \frac{\omega \tau}{1 + (\omega \tau)^2} \, d\Delta \, d\lambda \ . \tag{2.28}$$

(2.28) can only be solved numerically but analytic solutions can be found for two limiting cases: $\omega \tau_{\mathrm{min}} \ll 1$ and $\omega \tau_{\mathrm{min}} \gg 1$.

To simplify the discussion one defines a reference temperature $T^\star$. At this temperature the relaxation rate of the *symmetric* systems equals the frequency of the perturbation, i.e. $\omega \tau_{\mathrm{min}} \simeq 1$.

- $T < T^\star$ (low temperature behaviour): in this range $\omega\tau_{\min} \gg 1$ is valid and means that even the fastest tunneling systems are not able to attain thermal equilibrium within a period of the applied field. Only the contribution of the fastest relaxing systems have to be considered and

$$Q^{-1} \propto \tau_{\mathrm{d}}^{-1} \propto \frac{C\,T^3}{\omega} \qquad (2.29)$$

with the *macroscopic coupling constant*

$$C = \frac{\overline{P}\gamma^2}{\rho v^2} \ , \qquad (2.30)$$

which contains all the important parameters of the glass under consideration.

As the systems are too slow the relaxation process does not contribute to the change of sound velocity.

- $T > T^\star$: with $\omega\tau_{\min} \ll 1$, one receives after integration of (2.28):

$$Q^{-1} = \frac{\pi}{2}C. \qquad (2.31)$$

In this regime Q^{-1} is expected to be independent on frequency and temperature.

For the sound velocity one finds a logarithmic temperature dependance

$$\left.\frac{\delta v}{v}\right|_{\mathrm{rel}} = -\frac{3}{2}\,C\ln\left(\frac{T}{T'}\right)\ , \qquad (2.32)$$

where T' is an arbitrary temperature.

Resonant process

If the energy $\hbar\omega$ of the phonons corresponds to the energy splitting E, absorption and emission can take place. For a significant absorption the condition $E > k_{\mathrm{B}}T$ should be fulfilled. For frequencies $f < 20\,\mathrm{kHz}$, that were used in this thesis, this can be achieved only in the μK range. As the lowest temperature is in the mK-range, the contribution of the resonant absorption to the internal friction can be neglected.

Considering the sound velocity, the resonant process for $\hbar\omega \ll k_{\mathrm{B}}T$ leads to a logarithmic increase with temperature

$$\left.\frac{\delta v}{v}\right|_{\mathrm{res}} = C\ln\left(\frac{T}{T'}\right)\ . \qquad (2.33)$$

Prediction of the standard tunneling model

If one summarizes the contributions of relaxation and resonant processes, one will get the following predictions of the standard tunneling model on the temperature dependence of Q^{-1} and $\delta v/v$:

Starting at low temperatures the sound velocity rises due to the resonant interaction of two-level systems and phonons in a logarithmic way:

$$\frac{\delta v}{v} = C \ln\left(\frac{T}{T'}\right) \quad \text{for } T < T^* \ . \tag{2.34}$$

Due to the occurrence of relaxation processes a maximum is reached at a temperature T^*, which is connected to the condition $\omega\tau_{\min} = 1$. Due to the energy splitting E corresponding to the thermal energy $k_\mathrm{B}T$, from (2.27) it follows

$$T^* = \sqrt[3]{\frac{\pi\omega\rho\hbar^4}{k_\mathrm{B}^3}\left(\frac{\gamma_\ell^2}{v_\ell^5} + 2\frac{\gamma_\mathrm{t}^2}{v_\mathrm{t}^5}\right)^{-1}} \propto \omega^{\frac{1}{3}} \ , \tag{2.35}$$

The total change of sound velocity is a sum of the two contributions from (2.33) and (2.32). In this way $\delta v/v$ decreases logarithmically at higher temperatures:

$$\frac{\delta v}{v} = -\frac{1}{2}\,C \ln\left(\frac{T}{T'}\right) \quad \text{for } T > T^* \ . \tag{2.36}$$

Plotting $\delta v/v$ on a logarithmic temperature scale, results in a characteristic signature: sound velocity rises with temperature, passes a maximum and decreases again. Hereby the expected ratio of logarithmic slopes of the frequencies at sufficiently high and low tempertures is $2 : -1$.

For the internal friction in our experiments only the relaxationary contribution is present. From low temperatures a T^3 behaviour is predicted for all frequencies, which turns into a frequency- and temperature-independent plateau for $T > T^*$.

2.3   Previous experimental data and extensions of standard tunneling model

In this section the results of former acoustic measurements are presented and compared with the predictions of the standard tunneling model. Deviations from the expected behaviour lead to possible extensions of the standard tunneling model, which are introduced.

Figure 2.7 shows the temperature dependence of $\delta v/v$ and Q^{-1} of amorphous SiO_2 (Suprasil 300) at different frequencies in the kHz range. The measurements were done with mechanical oscillators, the so-called double-paddle oscillators, which will be discussed in detail in chapter 3 [Cla00]. The results agree qualitatively with the predictions of the tunneling model: from low to high temperatures the sound velocity rises first logarithmically, goes through a maximum and then drops logarithmically. The internal friction rises with increasing temperature until it reaches a nearly frequency-independent plateau above $200\,\mathrm{mK}$. However one can observe clear quantitive deviations: The proportionality of the slopes of the sound velocity is not $2 : -1$ as predicted by the standard tunneling model ((2.34) and (2.36)), but rather $1 : -1$. In addition, the slope of the rise exhibits a clear frequency dependence. Furthermore one does not find a cubic temperature dependence for

the internal friction below the plateau, but a frequency dependent power law $Q^{-1} \propto T^{\eta}$. Here the exponent η varies monotonously with frequency from 0.8 to 2.3. An almost similar behaviour was observed in the multi-component glasses BK 7 and Fs 21 [Lay00].

The solid lines in the right side of figure 2.7 are fits according to the standard tunneling model for 0.33 kHz and 14.0 kHz, respectively. As the deviations from the standard tunneling model to experimental values become larger towards lower temperatures, additional relaxation channels are assumed to cause this behaviour. In particular, it has been suggested that the interaction *between* tunneling systems is responsible. Several theoretical approaches were developed to solve this problem and will be discussed in the following.

The first suggestion was given by Burin and Kagan [Bur94, Bur95]. Their theoretical approach is based on the elastic interaction of two-level systems which couples two two-level systems by virtual phonons. The coupling of two-level systems with similar energy splitting leads to the formation of pairs. Due to the "flip-flop" motion of these pairs, consequently there are additional relaxation channels between the pairs. The relaxation rate of the couple pairs can be estimated by

$$\tau_{\mathrm{p}}^{-1} \approx \frac{10 k_{\mathrm{B}} C^3}{\hbar} \left(\frac{\Delta_0}{E} \right)^2 T \ . \tag{2.37}$$

C is the value from the plateau of standard tunneling model. Below some crossover temperature this contribution should be larger than the one-phonon rate in (2.27). With $Q^{-1} \propto \tau_{\mathrm{p}}^{-1}$ this should lead to a linear temperature dependence of the internal friction at very low temperatures. However, numerical estimations show that the influence of τ_{p} is negligibly small in the temperature range of interest as the crossover temperature is estimated to be smaller than 1 mK. If the numerical prefactor of (2.37) has to be
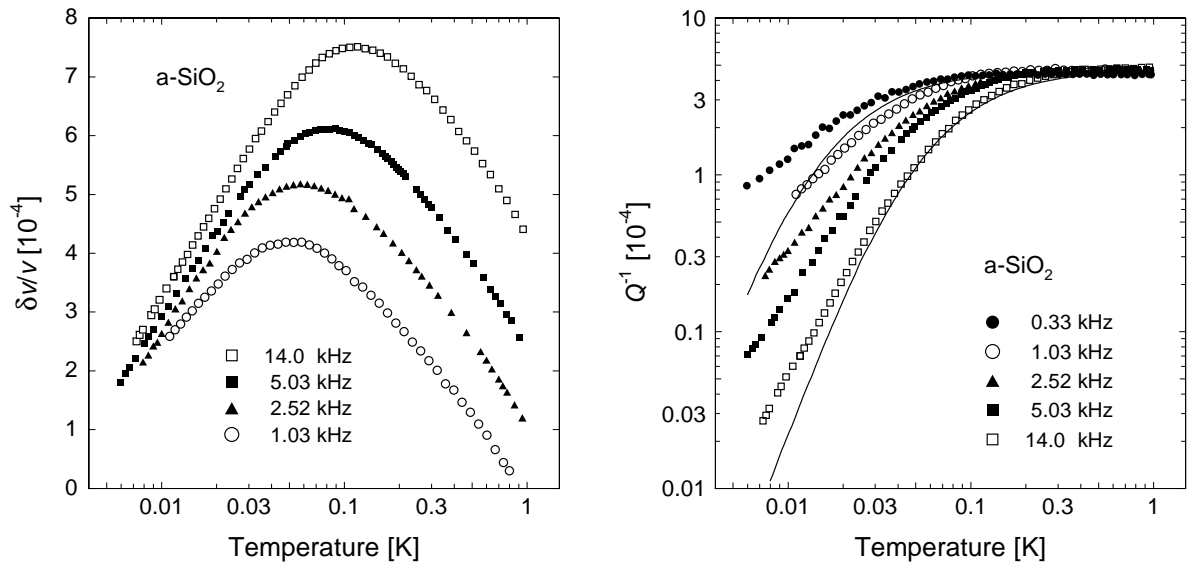
Fig. 2.7: Temperature dependence of the relative change of the sound velocity and internal friction of the amorphous SiO_2 at different frequencies. The solid lines are fits according to the standard tunneling model for 0.33 kHz and 14.0 kHz, respectively [Cla00].

increased by a factor 10^4, astonishingly the experimental data can be fitted very well
with an additional relaxation contribution of the form $\tau^{-1} \propto (\Delta_0/E)^2 T$ [Cla00]. From
this finding one can conclude that the approach by Burin is not adequate to describe the
experimental data.

Another suggestion is based on a theory by Wuerger [Wue94, Wue95, Wue97] about
the dynamics of substitutional defects in alkali halide crystals. According to this model
the coupling of tunneling systems leads to a suppression of coherent tunneling processes in
favor of an increase of incoherent processes. As a consequence the resonant contribution to
the acoustic susceptibility is decreased. Furthermore the many-body interaction coupling
of defects leads to a relaxation process and therefore opens another process. The relaxation
rate is given by

$$\tau_{\mathrm{i}}^{-1} \propto \mu^4 T \; . \tag{2.38}$$

The relationship $\mu = \overline{J}/\Delta_0$ with the average interaction energy $\overline{J}$ of the tunneling system
and the tunneling splitting Δ_0 is the central parameter of this model. Transferring this
model to glasses was suggested by Enss and Hunklinger [Ens97], where the broad distri-
bution of Δ_0 must be considered. With (2.38) the weaker temperature dependence of Q^{-1}
and $\delta v/v$ on the very low-temperature side can be understood qualitatively.

In 1998 a surprising discovery in BaO-Al$_2$O$_3$-SiO$_2$ glass was reported in dielectric mea-
surements at very low temperatures [Str98]. An abrupt change of the slope of the dielec-
tric constant in the BaO-Al$_2$O$_3$-SiO$_2$ glass at 5.84 mK could be observed. The authors
assumed that at this temperature a phase transition takes place from the uncorrelated
and incoherent tunneling motion of individual tunneling systems to a highly correlated
coherent motion. It is still an unsolved question if this kind of phase transition occurs
in all glasses. Since the dielectric and acoustic properties are closely related within the
standard tunneling model, this phase transition is also expected in acoustic experiments.

The combination of theoretical and experimental results shows that the interaction
between tunneling systems must be an indispensable component for future theories. In
addition it is necessary to accomplish measurements at temperatures as low as possible so
that interaction effects can be investigated in more detail.

3. Mechanical oscillators

Elastic properties of solids in acoustic frequency range can be tested by mechanical oscillators. The eigenmodes can be chosen by the geometry of the sample. In the first part the simplest oscillator – a thin rectangular plate (*vibrating reed*) – is presented. Then a more complicated geometry structure – the so-called *double-paddle oscillator* – is introduced. Operation of amorphous oscillators at low temperatures requires small oscillation amplitudes, due to the occurence of nonlinear effects.

3.1 Vibrating reed

Vibrating reed measurements are a common and convenient technique to investigate the low-frequency elastic properties of solids. A typical setup is shown in the work by [Ber75]. The shape of the sample is a thin rectangular plate and the sample is clamped at one end between two blocks (figure 3.1), usually made of a material with good thermal conductivity, e.g. copper or silver. It is driven electrostatically by applying an ac-voltage from an electrode located near one side of its free end. In order to get an electric conductivity and thermalization, insulating materials must be covered with a thin metallic layer. This layer should be thin enough to exclude a noticeable influence on the measured quantities. A second electrode detects the vibrations and should be placed as close as possible to the other side of the free end of the sample in order to gain maximum sensitivity of the signal.
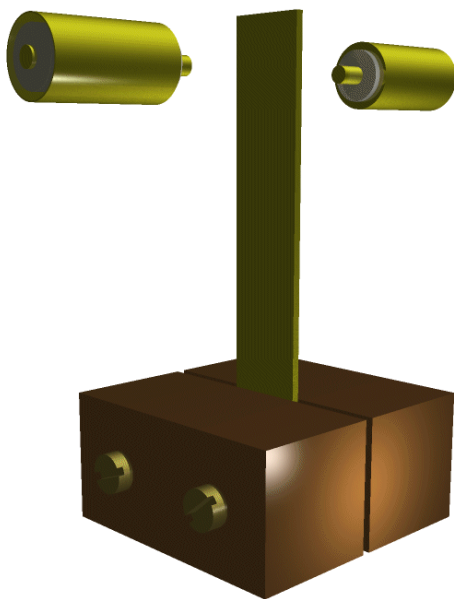
Fig. 3.1: Schematics of a vibrating reed experiment. The sample is clamped between two copper blocks. Electrodes excite and detect the oscillation [Hei02].

The principle of measurement and the electronics is the same for vibrating reed and double-paddle oscillators and will be shown in section 4.4.

The equation of motion for a reed can be deduced and the solution of the differential equation was discussed [Kin62, Sku54, Cou53]. This solution is shown straightforward and will not be discussed here. As solution one gets the following formula for the resonance frequencies:

$$f_n = \alpha_n (2n+1)^2 \frac{\pi}{16\sqrt{3}} \frac{d}{L^2} v_{\mathrm{Y}} \; . \tag{3.1}$$

with the numerical values for the different constants α_n:

$$
\begin{aligned}
\alpha_0 &= 1.424987 \\
\alpha_1 &= 0.992249 \\
\alpha_2 &= 1.000198 \\
\alpha_3 &= 0.999994 \\
\alpha_n &\simeq 1 \quad \text{for} \quad n \geq 4 \; .
\end{aligned}
\tag{3.2}
$$

The sound velocity v_{Y} is defined by the relationship from Young's modulus Y of elasticity and mass density ρ

$$v_{\mathrm{Y}} \equiv \sqrt{\frac{Y}{\rho}} \; . \tag{3.3}$$

Additionally the length L and the thickness d of the reed in (3.1) are necessary for the computation of the resonance frequencies. Typical dimensions of reeds are $5-15\,\mathrm{mm}$ in length, $2-3\,\mathrm{mm}$ in width and about $100\,\mu\mathrm{m}$ in thickness. The sound velocity is of the order of $10^3\,\mathrm{ms}^{-1}$. Thus the eigenfrequencies lie in the range between $100\,\mathrm{Hz}$ and $20\,\mathrm{kHz}$. It is remarkable that the resonance frequencies are not integers of the fundamental frequency. The first harmonic arises at $f_1/f_0 \approx 6.27$, the second one at $f_2/f_0 \approx 17.55$, and the third one at $f_3/f_0 \approx 34.39$. Neglecting thermal expansion the relation $\delta f/f = \delta v/v$ works (see chapter 3) and the change of sound velocity can be measured by the shift of resonance frequency with an accuracy of the order of 10^{-6}.

The bending motion contains transversal as well as longitudinal strain components. From [Rab86] one gets the change of sound velocity as

$$\frac{\delta v_{\mathrm{Y}}}{v_{\mathrm{Y}}} = \frac{\delta v_{\mathrm{t}}}{v_{\mathrm{t}}} \,\mathrm{g}(\mu) + \frac{\delta v_{\mathrm{l}}}{v_{\mathrm{l}}} \left[1 - \mathrm{g}(\mu) \right] \; , \tag{3.4}$$

and for the internal friction

$$Q^{-1} = Q_{\mathrm{t}}^{-1} \,\mathrm{g}(\mu) + Q_{\mathrm{l}}^{-1} \left[1 - \mathrm{g}(\mu) \right] \; , \tag{3.5}$$

where $\mathrm{g}(\mu)$ is defined as a function of the Poisson number μ

$$\mathrm{g}(\mu) = \left(\frac{4\mu - 2\mu^2}{1+\mu} \right) \; . \tag{3.6}$$

The advantage of the vibrating reed method is the simple geometry of the samples and their simple production. By mechanical processing one can make suitable samples from

many kinds of materials. Beside for glasses the technique is also used for the investigation of elastic properties of crystalline and metallic samples. However, the method has also disadvantages. In some cases only one mode can be measured with the vibrating reed, because the amplitude of the resonance is too small and hardly detectable. In addition the maximum strain takes place at the clamping.

Figure 3.2 shows the result of simulations with finite element methods (FEM) [Hei02]. Here a crucial disadvantage of the reeds becomes clearly visible: The maximum strain arises at the clamping part of the holder. This means that elastic energy is located there and be dissipated into the sample holder. As consequence an additional contribution of the damping of the oscillator arises. As the loss mechanisms are not known in detail, the magnitude of this contribution can hardly be measured. However, it seems typically of the order of $Q^{-1} \simeq 10^{-5}$, as quality factors, larger than 10^5, were not reached in reed experiments. These background losses can be usually neglected, if the intrinsic sample damping is bigger than 10^{-4}. Also with the measurement of the internal friction of the glasses at very low temperatures the reed technique reaches its limits. With SiO_2 and BK7 glasses were measured below $10\,mK$ and the internal friction is $Q^{-1} \leq 10^{-5}$ [Cla00, Lay00]. For these reasons vibrating reed technique is replaced by the double-paddle oscillators, which is described in the next section.
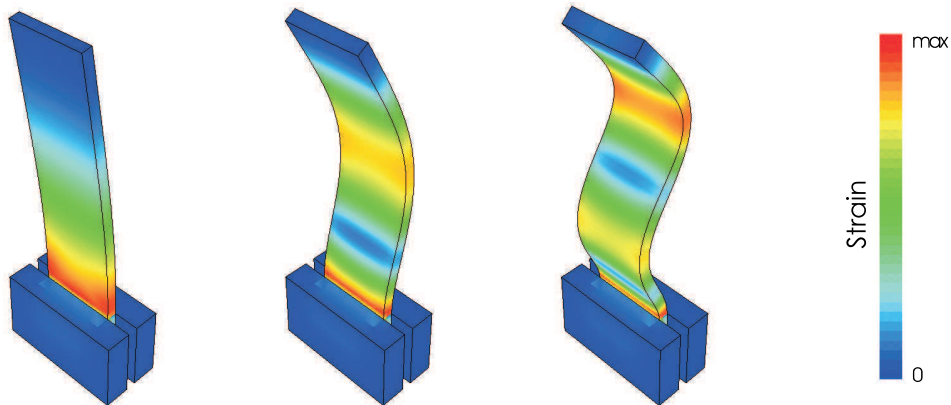
Fig. 3.2: Finite element simulation of the fundamental mode and the harmonics. The colorcode represents the relative strain of the sample. Compared to the dimensions of the sample the oscillations are strongly exaggerated [Hei02].

3.2   Double-paddle oscillator

The double-paddle oscillator (DPO) is a further development of the vibrating reed. Due to its very small background loss, the acoustic properties of amorphous solids at very low temperture can be measured more precisely. The geometry of this oscillator was developed by Kleiman *et al.* [Kle87] and later improved by Pohl *et al.* [Hes96, Whi95].

Figure 3.3 shows the geometry of the double-paddle oscillator with the notation for the different parts of the oscillator. The excitation and detection of the oscillation take place

with electrodes, which are attached in front of the wings (a detailed description of the experimental arrangement will be given in section 4.4).

For the different materials, such as crystals, glasses, superconductors, the sample can be manufactured by several methods: ultrasonic cutting, laser cutting, chemical wet etching, anisotropic wet etching. The last one can specially be used for crystalline materials.

The glass paddles, which were used in our experiment, were manufactured by laser cutting. As the samples are heated locally in this process, it is important that the thermal expansion of the sample should not be too large, otherwise the glasses might shatter.
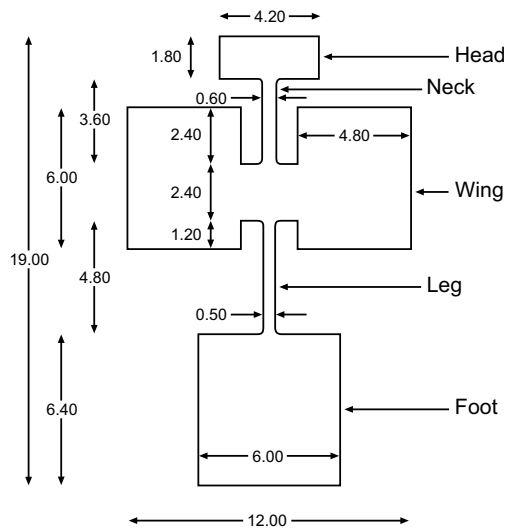

Fig. 3.3: Geometry of the paddles with the notations used in our experiment. All dimensions are given in mm, the thickness is about 0.4 mm.

In figure 3.4 finite element simulations of the experimentally relevant modes are presented [Hei02]. The upper row shows the first three bending vibrations (B1 – B3) as well as the so-called *flapping*-mode (F1), where an additional flapping – wings-knocking – arises. In the lower row one can see the symmetric torsional mode (ST) and two antisymmetric torsional modes (AT1 and AT2). The symmetric torsional mode is characterized by an in-phase vibration of head and wings. For the symmetric torsional mode (ST) maximum strain field occurs at the leg of the paddle and consequently a large amount of oscillationary energy can be dissipated. The background loss of this mode should be larger than the other two antisymmetric torsional modes. Compared to the vibrating reed the bending modes include longitudinal and transversal polarization, the torsional modes ST and AT1 represent purely transversal motion.

The vibration of the antisymmetric modes is characterized by the fact that head and wings have a phase shift of 180° with respect to each other. Furthermore the leg is hardly twisted. As the oscillation energy is localized in the range of the neck of the paddle, the vibration is strongly decoupled from the sample holder. Consequently the dissipation of elastic energy into the sample holder is minimized. And the AT modes are predestinated for the measurement of small intrinsic dampings. However, the small deflection of the wings causes a very small detection signal.

The computed resonant frequencies as well as the experimental resonant frequencies of a BK7 paddle at low temperatures lie between 100 Hz and 20 kHz and are listed in
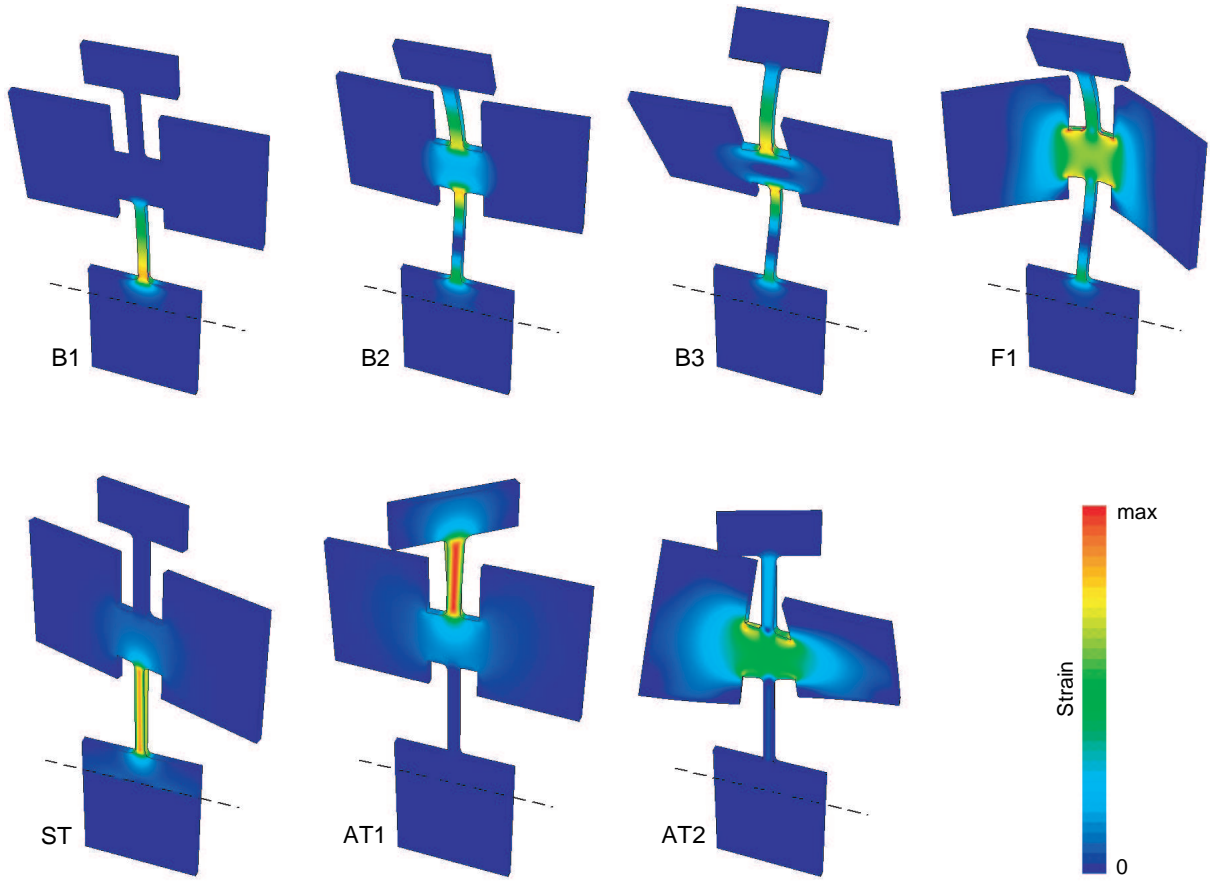
Fig. 3.4: Finite element simulations of the experimentally relevant eigenmodes of the double-paddle oscillator. The relative stress field is color-coded. The part below the dashed line represents the clamping of the paddle, in order to simulate its restraints [Hei02].

table 3.1 [Lay00]. The characteristics of the different modes are also given in table 3.1. As the vibration of AT1 mode of BK7 paddle is too small to be detected by the capacitive method (see section 4.4), table 3.1 does not show the experimental frequency of this mode. It is remarkable that the computed resonant frequencies of high frequency modes are smaller than the experimental frequencies, whereas the four low-frequency modes exhibit larger values than those of the computed frequencies. There are several reason for these deviations. Since for high frequency modes a larger distortion occurs in the neck area, only a small amount of vibrational energy is dissipated in the sample holder. So a high quality factor can be reached. Due to the tolerance in the production of the paddle, the resonance frequencies are usually different around some percent compared to the results of the simulation.

The sample is covered on one side with a 1 μm thick silver film. This ensures a good thermalization of the glass paddle at low tempertures and allows to use a capacitive excitation and detection technique. The influence of a thin film can be taken into account by considering the entire oscillation energy $E = E_{sub} + E_{film}$ and the dissipated energy $\Delta E = \Delta E_{sub} + \Delta E_{film}$ from the substrate and the film, respectively. If the thickness of the

Mode	f_{FE} [Hz]	f_{exp} [Hz]
Bending mode B1	879	754
Bending mode B2	3950	3479
Bending mode B3	8588	7980
Flapping mode F1	12495	13708
Symmetric Torsion ST	1580	1426
Antisymmetric Torsion AT1	11470	
Antisymmetric Torsion AT2	13752	15414

Tab. 3.1: Comparison between the measured eigenfrequencies of a BK7 paddle with the results of finite element method (from [Lay00]).

film d_{film} is much smaller than the thickness of the substrate d_{sub}, then it follows $E \approx E_{\text{sub}}$. From the definition

$$Q^{-1} := \frac{1}{2\pi} \frac{\Delta E}{E} \tag{3.7}$$

we can get a formula for the internal friction

$$Q^{-1} = \frac{1}{2\pi} \left(\frac{\Delta E_{\text{sub}}}{E_{\text{sub}}} + \frac{E_{\text{film}}}{E_{\text{sub}}} \frac{\Delta E_{\text{film}}}{E_{\text{film}}} \right) = Q_{\text{sub}}^{-1} + \frac{E_{\text{film}}}{E_{\text{sub}}} Q_{\text{film}}^{-1} \; . \tag{3.8}$$

Hereby E_{sub} and E_{film} depend on the experimental setup of the oscillator. The resonance frequency of an oscillator can simply be described by an effective mass m and an effective "spring constant" k:

$$f_0 \propto \sqrt{\frac{k}{m}} \; . \tag{3.9}$$

Changes by the film in Δk and Δm influence the resonance frequency as follows:

$$\frac{\Delta f}{f_0} = \frac{1}{f_0} \left(\frac{\partial f}{\partial k} \Delta k + \frac{\partial f}{\partial m} \Delta m \right) = \frac{1}{2} \left(\frac{\Delta k}{k} - \frac{\Delta m}{m} \right) \; . \tag{3.10}$$

For the torsional modes of the paddles these equations can be expressed by the shear modulus G_{sub} and G_{film} as well as the densities ρ_{sub} and ρ_{film} in the substrate and in the film:

$$Q^{-1} = Q_{\text{sub}}^{-1} + \frac{3 d_{\text{film}} G_{\text{film}}}{d_{\text{sub}} G_{\text{sub}}} Q_{\text{film}}^{-1} \tag{3.11}$$

and

$$\frac{\Delta f}{f_0} = \frac{d_{\text{film}}}{2 d_{\text{sub}}} \left(\frac{3 G_{\text{film}}}{G_{\text{sub}}} - \frac{\rho_{\text{film}}}{\rho_{\text{sub}}} \right) \; . \tag{3.12}$$

The indices stand for the silver layer (film) and for those of the substrate (sub), respectively. d is the respective thickness, G is the shear modulus and ρ is the mass density. For the bending modes, Young's modulus of elasticity energy has to be taken into account. To estimate the frequency change, the values of BK 7 and a silver layer are used. With $G_{\text{Ag}} = 2.95 \cdot 10^{10} \, \text{Nm}^{-2}$, $G_{\text{BK7}} = 3.4 \cdot 10^{10} \, \text{Nm}^{-2}$, $\rho_{\text{Ag}} = 10.50 \, \text{g cm}^{-3}$, $\rho_{\text{BK7}} = 2.51 \, \text{g cm}^{-3}$ and $d_{\text{Ag}}/d_{\text{BK7}} = 2.5 \cdot 10^{-3}$ from (3.12) one gets $\Delta f/f \approx -2 \cdot 10^{-3}$, i.e. the calculated resonant frequency is higher by about 0.2 percent.

All effects mentioned cause a correction of the resonance frequency. The deviations from experiment and simulated values can be explained within this framework.

The glass samples presented in this work are known as Suprasil and BK7. Vitreous silica is a general term for natural and synthetic glasses which are almost composed of silicon dioxide ($> 99\,\%$). The impurity concentration is as follows (all data in ppm): Al 0.05, Ca 0.05, Cr 0.005, Cu 0.01, Fe 0.02, K 0.01, Li 0.01, Mg 0.005, Na 0.05, Ti 0.05 [Her94].

The chemical composition of BK7 is appoximately given by the main ingredient SiO_2 ($60\text{-}70\,\%$), B_2O_3 ($10\text{-}20\,\%$), BaO ($< 1\text{-}10\,\%$), Na_2O ($1\text{-}15\,\%$), and K_2O ($5\text{-}15\,\%$). The residual components is less than $1\,\%$, which are ZnO, CaO, TiO_2, and Al_2O_3.

The samples of vitreous silica and BK7 used in our measurement have been cut from a flat with laser in Hannover[1].

3.3 Nonlinear effect

Acoustic experiments on glasses based on vibrating reed and double-paddle oscillator technique show a strong dependence of the sound velocity on the excitation amplitude, if the strain energy reaches the order of the thermal energy of the sample [Esq92, Cla94].

In figure 3.5 the temperature dependence of the relative change of sound velocity $\delta v/v$ of Suprasil W is presented at different excitation voltages. The behaviour of $\delta v/v$ is qualitatively the same as predicted by the standard tunneling model. The sound velocity rises first logarithmically, goes through a maximum and drops then logarithmically from low temperature to high temperature. Although the excitation voltages are different, there is no difference between the curves at high temperture. However, the deviations occur at low tempertures. The slope of the relative change of sound velocity $\delta v/v$ is strongly dependent on the excitation voltage, namely from $2:-1$ at large driving fields to $1:-1$ at small driving fields. The temperatures, at which the maximum in the sound velocity occurs, also shift to the low temperature with decreasing driving voltage.

In order to understand the dependence on the driving force one should consider the modulation of the asymmetry energy Δ due to the strain field e. Assuming an oscillatory time dependence one can get a formula for the energy splitting (see [Esq98]):

$$E(t) = \sqrt{\Delta_0^2 + [\Delta + 2\gamma e_0 \sin(\omega t)]^2} \, . \tag{3.13}$$

Averaging this expression with respect to time results in an increase of energy splitting (see figure 3.6) resulting in a occupation number difference.

$$\Delta N \propto \tanh\left(\frac{E + \delta E}{2k_{\mathrm{B}}T}\right) . \tag{3.14}$$

The occupation numbers of an ensamble of two-level systems at a finite strain field e_0 is similar to a state without strain, where the sample is at a lower temperature. Typical strain field energies γe_0 correspond to tempertures below the maximum in sound velocity.

---

[1]Laser Zentrum Hannover.
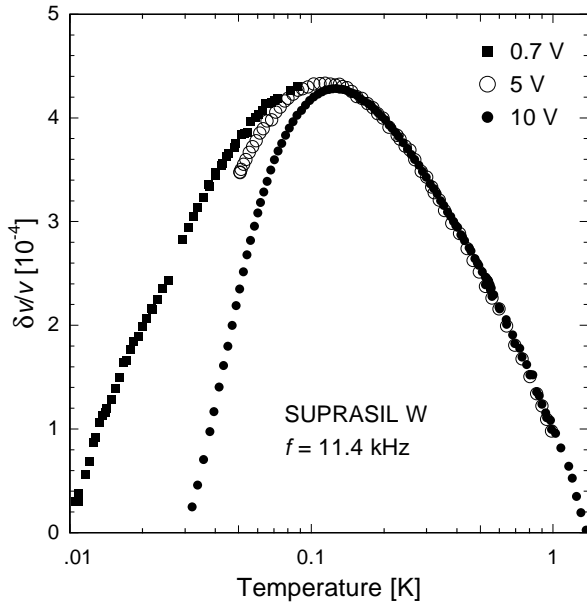
Fig. 3.5: Temperature dependence of $\delta v/v$ in amorphous SiO_2 with different excitation voltages. Below $100\,\mathrm{mK}$ a significant dependence of the sound velocity on the excitation voltage is visible. The measurements were performed with the vibrating-reed technique [Cla94].

As in this range only resonant contributions are valid, this results in a reduction of sound velocity and resonance frequency of the oscillator. A quantitative analysis of this problem is given in [Sto95].

Nonlinearities have drastic effects on the appearance of the resonance curves. In the linear case the resonance curve should be Lorentzian. However, the position of the resonance frequency decreases steadily with increasing excitation voltage, i.e. the resonance frequency moves to the "left" side.

Figure 3.7 shows this effect on the AT2 mode for an a-SiO_2 paddle. Furthermore one can see hysteretic effects arising with increasing excitation voltage: the shape of the curves depend upon the direction of the frequency sweep. Jumps occur from one branch of the resonance curve to the other at different frequencies. For the two curves at the top the
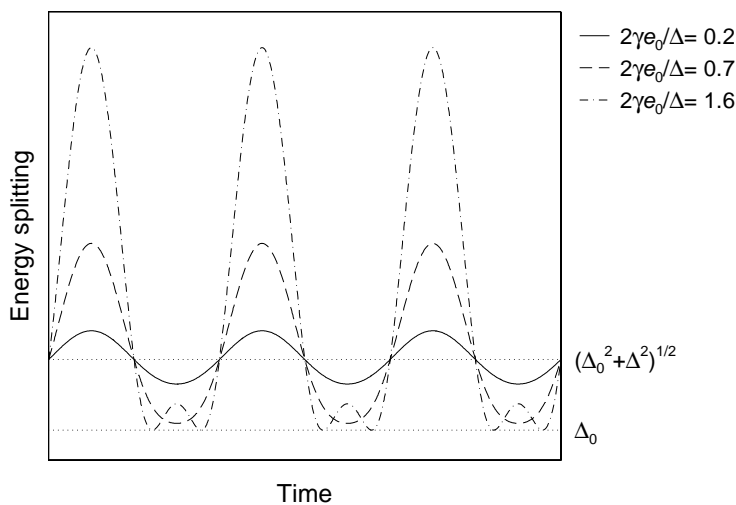
Fig. 3.6: Time dependence of the energy splitting of the tunneling systems with an elastic disturbance $\delta\Delta = 2\gamma e_0 \sin(\omega t)$.
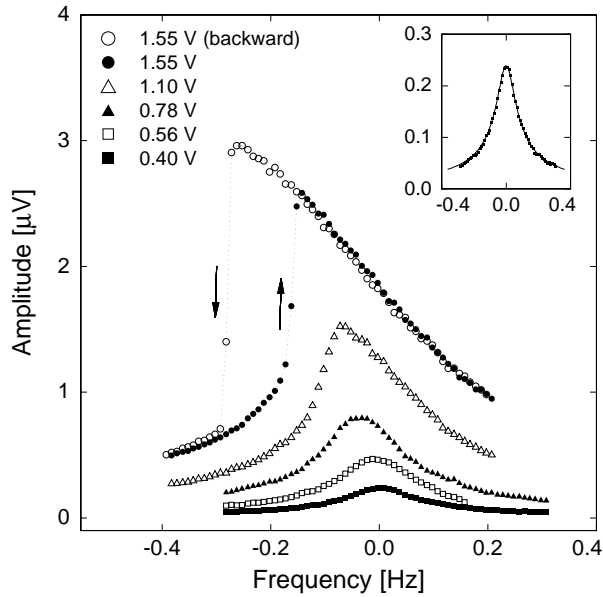
Fig. 3.7: Resonance curves of the AT2 mode ($f = 14017\,\text{Hz}$) of an a-SiO$_2$ paddle at $12.6\,\text{mK}$ for different excitation voltages. The top two curves show the dependence upon the direction of the frequency sweep with $1.55\,\text{V}$ [Cla01].

amplitude of the peak also depends on the direction of the frequency sweep.

These results show that for measurements in the linear regime the excitation voltage should be as small as possible, especially at low temperatures. However the capacitive detection technology (section 4.4) reaches its limits in this regime. With the smaller excitations the amplitude of the measuring signal goes down. For this reason within the framework of this thesis a more sensitive inductive method based on detection technology with a SQUID magnetometer is developed. This setup is described in the following chapter.

4. Experimental techniques

In this chapter the basic part of the experimental devices and techniques are presented. The experiments take place at low temperatures inside a dilution refrigerator, which is described in the first section. In the second section a low temperature device for the detection of small magnetic flux changes – a so-called SQUID is introduced, which is part of the novel inductive readout for mechanical oscillators described in detail in the next chapter as well as for the readout of a novel noise thermometer. The noise thermometer is based on the Johnson noise of the electron gas in a metal and therefore depends on the temperature of the sample which helps to improve the measurement of low temperatures. In the last section the conventional detection technique for mechanical oscillators is described.

4.1 Dilution refrigerator

The *dilution refrigerator* is a cooling device which generates temperatures down to the low milli-Kelvin range. This cooling technique has been discussed extensively in the literature (see e.g. [Pob92, Ens00b]). Therefore, only a brief sketch of the operating principle of the cryostat is given here.
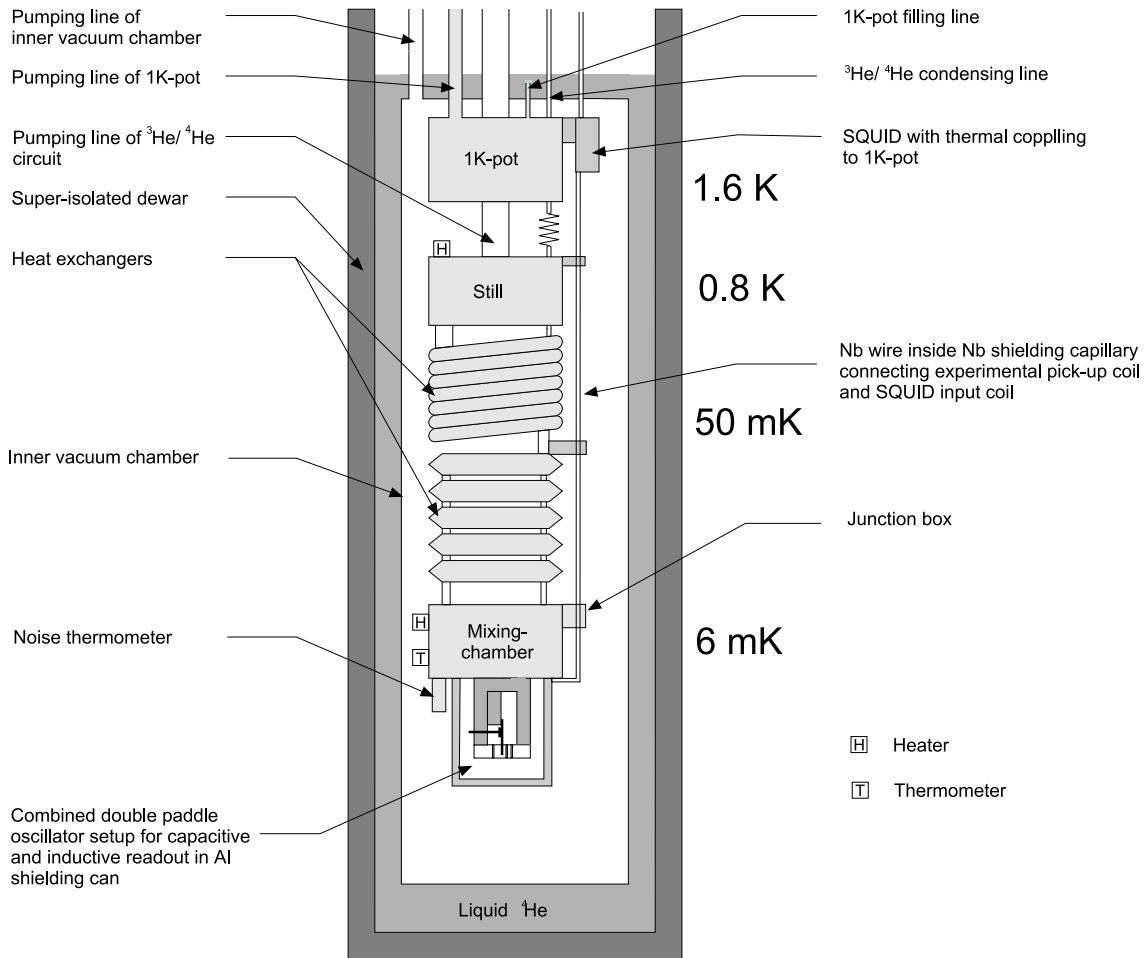
The dilution refrigerator uses a ^{3}He-^{4}He mixture and relies on the latent heat which occurs at the evaporation of ^{3}He atoms into a bordering ^{4}He phase. At temperatures above 0.87 K, the two liquids ^{3}He and ^{4}He can be mixed in arbitrary ratios. Below this temperature, the ^{3}He-^{4}He mixture separates in two phases, one rich in ^{3}He, and the other rich in ^{4}He. Due to the different densities, the ^{3}He-rich phase is on top of the ^{4}He-rich liquid. If the temperature is close to absolute zero, the ^{3}He-rich mixture is approximately pure ^{3}He. The concentration of ^{3}He in the ^{4}He-rich phase, however, does not vanish even at the temperature of absolute zero, but rather reaches a constant value of 6.4 %.

From the specific heats of pure ^{3}He and ^{4}He, we know that the enthalpy of ^{3}He in the diluted phase is larger than that of ^{3}He in the concentrated phase. When ^{3}He atoms are transferred from the pure ^{3}He phase to the diluted phase of a phase-separated mixture, a cooling effect takes place according to the enthalpy difference of the two phases.

Figure 4.1 shows a schematic of the dilution refrigerator[1] used for the experiments presented in this thesis. The system is set up in different stages which have a certain temperature distribution as indicated in the figure. The lowest part of the ^{3}He-^{4}He circuit is the *mixing chamber*. In this pot the phase transition of ^{3}He takes place. The mixed phase is connected by a tube from the mixing chamber to the *still*, where ^{3}He is evaporated and a mixture with a concentration of less than 1 % ^{3}He remains. ^{3}He from the mixture is pumped efficiently as the vapour pressure of ^{3}He is much bigger than that of ^{4}He at typical temperatures of 0.8 K. Due to the concentration gradient, an osmotic pressure

---

[1]Kelvinox 400, commercial dilution refrigerator, manufactured by Oxford Instruments (UK) Ltd., England

Pumping line of
inner vacuum chamber

Pumping line of 1K-pot

Pumping line of ^{3}He/ ^{4}He
circuit

Super-isolated dewar

Heat exchangers

Inner vacuum chamber

Noise thermometer

Combined double paddle
oscillator setup for capacitive
and inductive readout in Al
shielding can

1K-pot filling line

^{3}He/ ^{4}He condensing line

SQUID with thermal copplling
to 1K-pot

Nb wire inside Nb shielding capillary
connecting experimental pick-up coil
and SQUID input coil

Junction box

1K-pot

1.6 K

Still

0.8 K

50 mK

Mixing-
chamber

6 mK

H   Heater

T   Thermometer

Liquid ^{4}He

Fig. 4.1: Schematics of the dilution refrigerator with the experimental setup for double-paddle oscillator measurement and the noise thermometer used in this work. The temperatures of the different stages in our cryostat for ^{3}He-^{4}He circuit are indicated.

drives ^{3}He from the mixing chamber into the still and therefore forces ^{3}He atoms from the concentrated phase into the diluted phase within the mixing chamber. The flow of cold ^{3}He from the mixing chamber to the still is utilized to precool the incoming ^{3}He in the *heat exchanger*. The ^{3}He concentration in the diluted phase of the mixing chamber stays constant since ^{3}He atoms are continuously crossing the phase separation line from the concentrated to the diluted phase producing cooling due to the latent heat of mixing.

The ^{3}He gas pumped out from the still returns to the cryostat from the exit of the pump at room temperature. It is precooled by leading the condensing line through the liquid helium bath at 4.2 K. Re-condensation of ^{3}He takes place at the so-called $1\,\mathrm{K}{-}pot$. This vessel is filled with liquid ^{4}He and the vapour pressure of the fluid is reduced by pumping it to a low pressure in order to reduce its temperature. In our system the $1\,\mathrm{K}$-pot can be filled continuously through a variable impedance and reaches temperature of around 1.6 K. The precooling process goes on at the still and is accomplished in the heat exchangers before returning into the pure liquid ^{3}He phase in the mixing chamber.

The dilution refrigerator used for this experiment has a base temperature of about 6 mK. The mixing chamber can be heated by a 500 Ω heater. The temperature is controlled with PID-controller by the LR 700 AC resistance bridge[2].

Due to the similar experimental setup for the inductive readout technique of the double-paddle oscillator measurement as well as for the noise thermometer, the setup of one of them within the cooling device is presented in figure 4.1. For the readout, one SQUID is needed for each experiment. The principle of a SQUID is presented in detail in the next section. At this point only the typical working temperatures of the single experimental devices are presented. As shown in this figure, the SQUID is fixed thermally and mechanically to the 1 K-pot and therefore has a temperture of about 1.6 K. The twisted superconducting wires connect the SQUID to the experimental setup at the mixing chamber within a superconducting shield. At different temperature stages, this wires are thermally coupled to the cooling circuit. The experimental setup for the double-paddle oscillator measurement and the new type of noise thermometer, which will both be described in detail in later sections, are mounted under the mixing chamber and therefore are variable in temperature.

4.2   SQUID magnetometer

In this section the SQUID magnetometer is described. The term magnetometer stands for a device that combines a magnetic flux transformer and a flux-voltage converter – a dc SQUID.

4.2.1   dc SQUID

SQUID is an abbreviation of "Superconducting QUantum Interference Device", which facilitates a transformation of the amount of magnetic flux to a voltage signal.
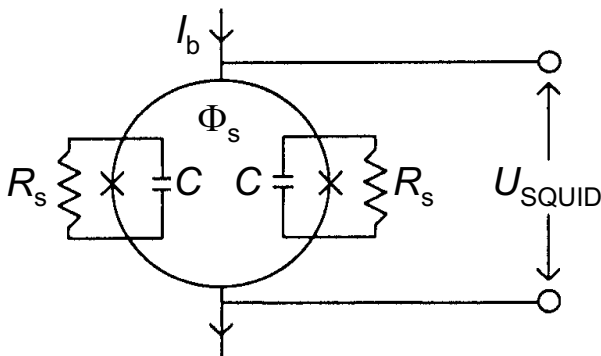
Fig. 4.2: Schematic diagram of a dc SQUID. The Josephson junctions are depicted by crosses. The capacities C are the intrinsic capacities of the Josephson junctions. The shunt resistors R_s suppress the hysteresis of the SQUID's current-voltage characteristics [Cla96].

As shown in the sketch of figure 4.2, a dc SQUID is a superconducting loop which is interrupted by Josephson junctions at two points (represented by the crosses). These Josephson junctions are thin insulating layers, which enable magnetic flux to enter the SQUID from the outside, and vice versa. The dc SQUID may be operated by applying

---

[2]LR700 AC resistance bridge was manufactured by Linear Research INC., San Diego, USA
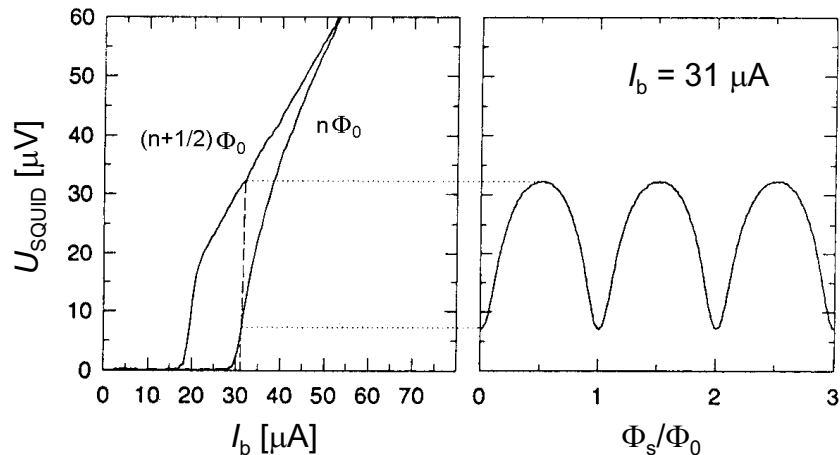
Fig. 4.3: Left side: Current-voltage characteristics of a typical dc SQUID with $\Phi_S = n\Phi_0$ and $\Phi_S = (n + \frac{1}{2})\Phi_0$. Right side: Flux-voltage characteristics for a fixed bias current $I_b > I_c$ [Cla96].

a constant bias current I_b and measuring the average voltage U_{SQUID} across the SQUID. When using constant bias current, the average voltage across the SQUID is a periodic function of the magnetic flux through the SQUID loop due to the quantum mechanical nature of the supercurrent.

The experimentally measured current-voltage characteristics of a typical dc SQUID is shown in figure 4.3. If the bias current I_b is smaller than a critical current I_c, the current flowing through the SQUID is carried by superconducting Cooper pairs, which can tunnel through the thin insulating barrier; therefore, there is no voltage drop across the SQUID. This critical current depends on the geometry of the tunneling barriers and the magnetic flux Φ_S enclosed by the SQUID loop. The left side of the figure shows the measured current-voltage characteristics of dc SQUID for magnetic flux values of $\Phi_S = n\Phi_0$ and $\Phi_S = (n + 1/2)\Phi_0$, where n is an integer and $\Phi_0 = h/2e$ is the magnetic flux quantum. If the bias current I_b is chosen to be slightly larger than the maximum critical current, the voltage difference across the SQUID will depend on the flux through the SQUID loop. From the right side of figure 4.3, it is apparent that the voltage U_{SQUID} depends on the flux Φ_S periodically. At the steepest part of flux-to-voltage curve the flux-to-voltage transfer function is greatest and almost linear for small signal. So the SQUID is most sensitive to the changes of flux.

Within the range of about $\Phi_0/2$ the voltage across the SQUID is monotonically dependent on the magnetic flux through the SQUID loop. Thus, an additional electronic circuit is utilized as a feedback technique. Then the SQUID is operated as a zero-point detector. The circuit performing this task in the present experiment is the flux-locked loop circuit, which will be described in the next section.

4.2.2   Flux-locked loop

The combination of a dc SQUID and a flux-locked loop circuit forms a linear flux-voltage transducer. To make the output linear, a flux-locked loop circuit with lock-in technique and a dc SQUID are applied, as shown in figure 4.4. This electronic circuit applies a

feedback flux to the loop to compensate any flux applied to the SQUID. In this case, the readout signal is no longer the voltage change across the SQUID. Instead, the flux-locked loop circuit keeps the working point of the SQUID by a feedback technique, and uses the voltage U across a feedback resistance R to indicate the flux change.
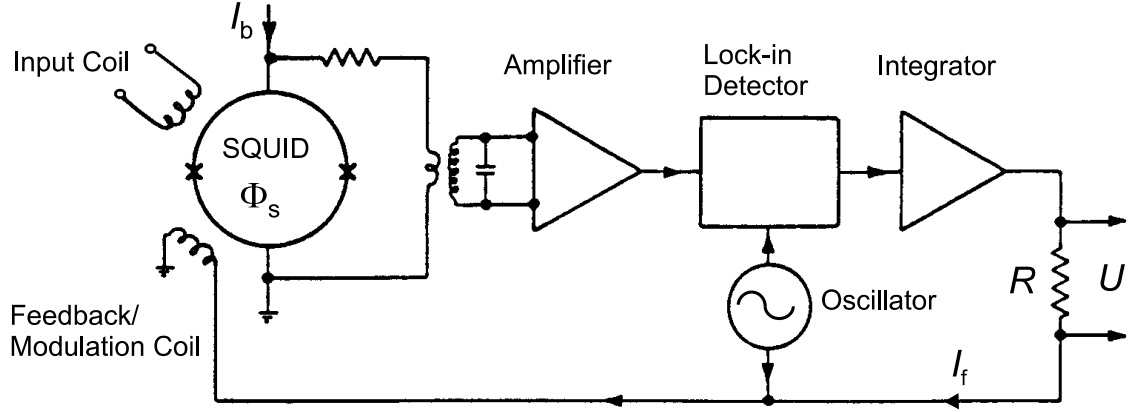
Fig. 4.4: Principle of a flux-locked loop circuit. This circuit facilitates the use of a dc SQUID as a flux-voltage transformer with a linear characteristics [Cla96].

Due to changes of the flux in the SQUID, the voltage across the SQUID is changed and is transfered into the pre-amplifier of the regulation system. A change of this voltage leads to an appropriate feedback current I_f, which will be sent through the feedback coil to compensate the change in Φ_S. To improve the sensitivity of the voltage change measurement, the lock-in technique is applied, in which the feedback current is superposed by a modulation current. The resulting modulation of the voltage across the SQUID leads to a more sensitive differential signal used to regulate the current in the feedback loop.

The feedback current I_f is proportional to the flux change in the SQUID loop and is read out by measuring the voltage U across a feedback resistance R, i.e. $\delta\Phi_S \propto I_f = U/R$. The conversion of the flux change in the experiment's pickup coils to the flux change in the SQUID loop will be discussed in the next section.

The feedback and SQUID readout electronics used in the present experiment are iMAG LTS Multi-Channel SQUID system[3]. The noise spectrum of this system is composed of mainly two contributions. One is white noise spectrum with a constant spectral density of about $2.5~\mu\Phi_0/\sqrt{\mathrm{Hz}}$. The other, the so-called $1/f$ noise, occurs only at low frequencies.

4.2.3 Transfer function of the magnetometer

In the magnetometer any change of magnetic field or magnetic gradient is detected by the pickup coils as a flux change $\delta\Phi_P$, and coupled into the SQUID via a flux transformer. Figure 4.5 shows the schematic of the magnetometer.

At low temperatures, the flux transformer circuit is entirely superconducting. Hence, the magnitude of the magnetic flux through its enclosed area is constant and is identical

---

[3]Tristan Technologies, San Diego, California, USA.
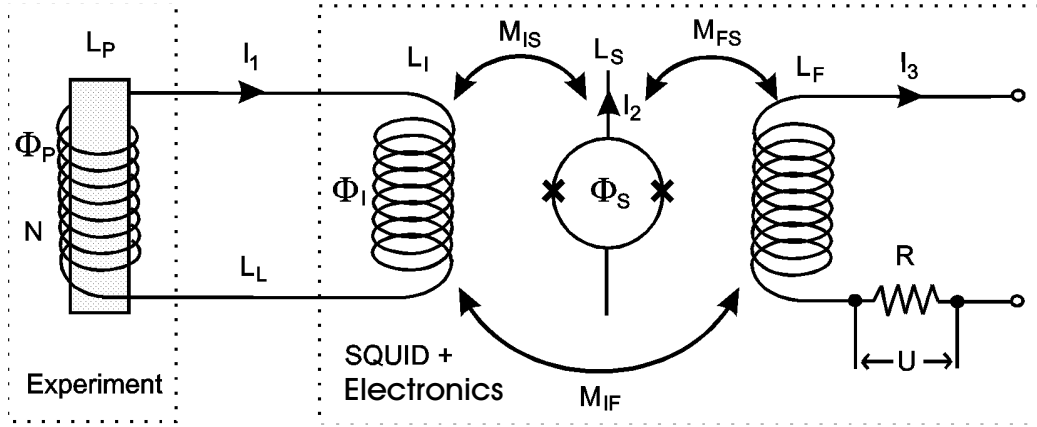
Fig. 4.5: Schematics of the magnetometer. Flux changes $\delta\Phi_{\rm P}$ detected by the pickup coil are coupled into the SQUID via the flux transformer. The quantity measured is the voltage change $\delta U = R\delta I_3$ in the feedback circuit [Fle98].
The quantities indicated are:

$\Phi_{\rm P}$	Flux through pickup coil	I_1	Current in SQUID input coil
$\Phi_{\rm S}$	Flux through SQUID loop	I_2	Bias current in SQUID loop
$L_{\rm P}$	Inductance of pickup coil	I_3	Feedback current
$L_{\rm L}$	Inductance of wires	R	Resistance in feedback circuit
$L_{\rm I}$	Inductance of SQUID input coil	U	Output voltage
$M_{\rm xy}$	Mutual inductances		

to the magnitude of magnetic flux which has been frozen in during cooling down. Any change in the magnetic flux through the pickup coil, $\delta\Phi_{\rm P}$, will therefore be compensated by changes in the currents in the input coil of the SQUID δI_1 and in the feedback circuit δI_3. The flux balance for the transformer loop from the pickup coil to the input coil of the SQUID can be written as

$$\delta\Phi_{\rm P} + (L_{\rm P} + L_{\rm L} + L_{\rm I})\delta I_1 + M_{\rm IF}\delta I_3 = 0\,. \qquad (4.1)$$

The quantities used here are explained in the caption to figure 4.5.

The magnetic flux through the SQUID loop is governed by another relation, which contains contributions from both the input coil and the feedback circuit, and from the flux noise $\delta_{\rm N}\Phi_{\rm S}$ in the SQUID. The noise contribution, however, is neglected here for simplicity. The net flux change in the SQUID loop is

$$\delta\Phi_{\rm S}^{\rm net} = \delta I_1 M_{\rm IS} + \delta I_3 M_{\rm FS}\,. \qquad (4.2)$$

If the input loop is open, i.e. $\delta I_1 = 0$, the flux change is $\delta\Phi_{\rm S}^{\rm net} = \Phi_0$, a specific current change is found $\delta I_{3,\Phi_0} = \Phi_0/M_{\rm FS}$ from (4.2). Then a characteristic quantity for the magnetometer is the specific voltage change $U_{\Phi_0} = R\,\delta I_{3,\Phi_0}$. In this case, one finds

$$U_{\Phi_0}^{\rm Open} = R\,\delta I_{3,\Phi_0} = R\frac{\Phi_0}{M_{\rm FS}}\,. \qquad (4.3)$$

In the presence of the superconducting transformer loop, however, both conditions presented by (4.1) and (4.2) have to be taken into account. The voltage change corresponding to a flux change Φ_0 in the SQUID loop is then given by

$$U_{\Phi_0} = U_{\Phi_0}^{\text{Open}} \left\{ \frac{1}{1 - \frac{M_{\text{IS}} M_{\text{IF}}}{M_{\text{FS}} L_{\text{I}}} \frac{L_{\text{I}}}{L_{\text{P}} + L_{\text{L}} + L_{\text{I}}}} \right\} . \tag{4.4}$$

This value should be greater than $U_{\Phi_0}^{\text{Open}}$ in an open input loop, if a mutual inductance $M_{\text{IF}} \neq 0$. With our commercial SQUID, we measured experimentally $U_{\Phi_0} \approx U_{\Phi_0}^{\text{Open}}$. It means that there is a negligible mutual inductance M_{IF} between the input coil and the feedback coil.

As mentioned in the previous section, due to the flux-locked loop technique the total flux Φ_{S} in the SQUID loop should be constant for a constant bias current I_2. Hence, during operation, it holds

$$\delta \Phi_{\text{S}}^{\text{net}} = 0 . \tag{4.5}$$

Combining this with (4.1) and (4.2), the voltage change δU resulting from a flux change $\delta \Phi_{\text{P}}$ in the pickup loop reads

$$\delta U = U_{\Phi_0}^{\text{Open}} \frac{\delta \Phi_{\text{P}}}{\Phi_0} \left(\frac{M_{\text{IS}}}{L_{\text{P}} + L_{\text{L}} + L_{\text{I}} \left(1 - \frac{M_{\text{IS}} M_{\text{IF}}}{M_{\text{FS}} L_{\text{I}}} \right)} \right) = U_{\Phi_0} \frac{M_{\text{IS}}}{L_{\text{P}} + L_{\text{L}} + L_{\text{I}}} \frac{\delta \Phi_{\text{P}}}{\Phi_0} , \tag{4.6}$$

i.e. δU depends linearly on the flux change $\delta \Phi_{\text{P}}$.

Table 4.1 shows the parameters of the SQUIDs used in our experiments.

$U_{\Phi_0}^{\text{Open}}$	L_{I}	M_{IS}	M_{FS}	M_{IF}
0.82 V	1860 nH	10 nH	1.3 nH	negligible

**Tab. 4.1:** Properties of the SQUIDs used in the experiment. The two SQUIDs are nearly identical.

4.3   Thermometry of the dilution refrigerator

The determination of temperature in the subkelvin range is a challenging problem. At first the widely used technique of resistance thermometry based on the temperature dependance of a carbon thermometer is introduced. To review and improve the temperature information in particular in the milli-Kelvin range, another type of thermometer – a noise thermometer was developed. An introduction to the noise thermometry and the novel setup is described. The comparison of both temperture informations leads to the conclusion that a re-calibration for the carbon thermometer has to be carried out.

4.3.1   Carbon thermometer

This type of thermometer is based on the temperature dependence of a commercial carbon resistor. It is widely used as secondary thermometer in the upper milli-Kelvin range. In our experiment the readout of the resistance is performed by a four-wire measurement with LR 700 AC resistance bridge. The carbon thermometer in our experiment is a self-made specimen and was calibrated to a second carbon thermometer used in our group. The second carbon thermometer setup was manufactured in the research group of K. Neumaier at the Walther-Meissner Institute in Munich (Neumaier 1983) and was calibrated for the temperature range between 18 mK and 4 K [Neu03]. In the temperature range between 5 and 18 mK, the calibration curve was extrapolated and verified with nuclear spin orientation thermometry [Wei95, Fle98].

   Figure 4.6 shows the calibration curve of the carbon resistor after calibration to the second carbon thermometer used in our experiment. Accurate resistances values were reached by averaging over significant time intervals and decreasing the applied measuring current. From high to low temperatures the carbon resistor shows a negative $R - T$ characteristic as expected for a semiconducting material. At about 15 mK one can see an unexpected kink in the curve, indicated by the arrow in figure 4.6. The flattening of
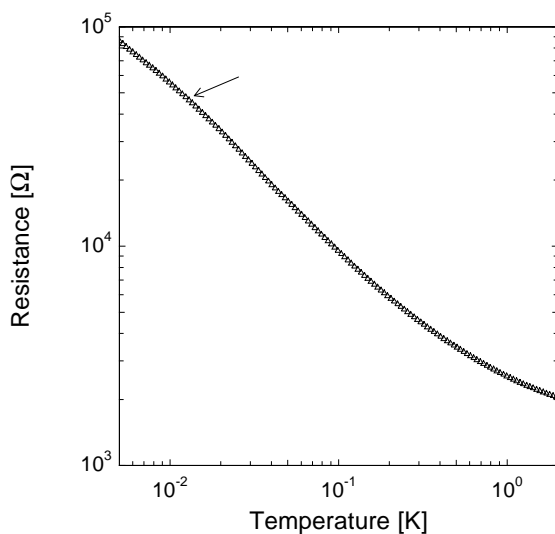
Fig. 4.6: Temperature dependence of the carbon resistor used in the experiment.

the curve in the temperature range below 15 mK might have several reasons, such as bad thermal coupling, kapitza resistance between the resistor and the mixing chamber or heat input from the heater via the connector during calibration. To improve the temperature information in particular at low temperatures, another type of thermometer – a new kind of noise thermometer – was built which is described in the following section.

4.3.2 Noise thermometer

Noise thermometry is based on the temperature dependence of the Johnson noise in a metal. The conduction electrons in a metal perform random thermal movements ("Brownian motion"), which result in statistical current fluctuation in a resistor. From elementary statistical considerations one can deduce that the mean square of noise current on the resistor $< I_N^2 >$ is proportional to the temperature, and is described by the so-called Nyquist equation [Pob92]:

$$< I_N^2 >= \frac{4k_B T}{R}\, \delta f. \tag{4.7}$$

Figure 4.7 shows the schematics of a current sensing noise thermometer setup. The resistor acts as a noise source which can be coupled via superconducting cables to a dc SQUID magnetometer. The SQUID can detect the square of the changing magnetic flux in the input coil $\Phi_I^2(T) = L_I^2 \, < I_I^2(T) > \propto T$. L_I is the inductance of the input coil and $< I_I^2 > = < I_N^2 >$. However, a problem with this type of noise thermometry at low temperatures is caused by "hot electron effects". At low temperatures, the electrons in an isolated conductor can only be cooled by transferring energy to phonons. With decreasing temperature, the number of phonons decreases rapidly. So the transferring rate can become very small at low temperatures and consequently the temperature of the electron system can be much higher than the temperature of the phonons. Experimentally the situation can be improved by electrically grounding the resistor to the place where the temperature is to be measured [Rou85, Lus01].
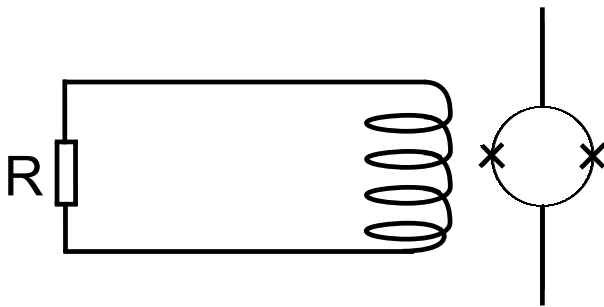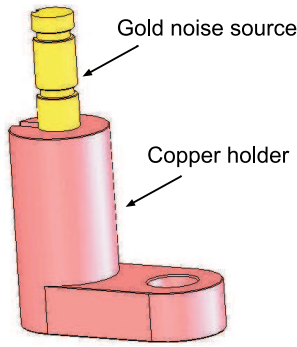

**Fig. 4.7:** Schematics of a current sensing noise thermometer.

Novel readout technique

In order to avoid the problem caused by hot electrons, a new type of noise thermometer was designed.

The Brownian motion of the electrons in a metal results in fluctuanting currents at different frequencies. These fluctuanting currents in the conductor generate flux noise, the

Fig. 4.8: Schematics of the noise thermometer setup. A gold stick (yellow) is clamped to the copper holder (pink), which is screwed to the mixing chamber.
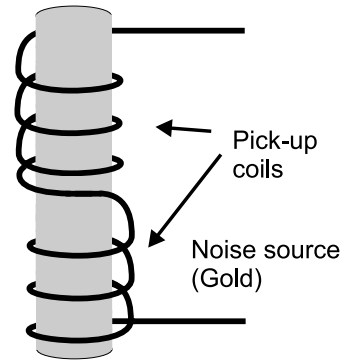
Fig. 4.9: Schematics of the novel noise thermometer. The noise source is enclosed by the pickup coils which are wounded in opposite directions. The pickup coils are connected to the input coil of the SQUID magnetometer.

so-called *magnetic Johnson noise*, depend on temperature and can be calculated with the reciprocity theorem [Har68]. The rms flux noise per $\sqrt{\text{Hz}}$ is written as

$$\sqrt{S_\Phi} \propto \sqrt{T}. \tag{4.8}$$

The design of this kind of noise thermometer is shown in figure 4.8. A gold cylinder acts as noise source. It is adapted to a copper holder, which is connected to the mixing chamber. The length of the gold sensor is about 10 mm and its diameter is about 2 mm. The whole setup is enclosed in a superconducting niobium shield to minimize external flux noise. Within the gold rod two necks are engraved for the wiring pickup coils. In order to minimize random magnetic flux noise that is coupling into the pickup coils, the niobium wire is wrapped in opposite directions around the necks, as a gradiometer indicated in figure 4.9. The pickup coils are connected to the input coil of the SQUID. As shown in figure 4.1, the twisted niobium wires are led from the pickup coil to the commercial dc SQUID via a junction box which is placed on the mixing chamber in order to easily install our experimental devices. The junction box is shielded with a niobium pot. In the box two niobium sticks with two screw eyes in each stick are mounted on the niobium base. The superconducting wire of the pickup coil is connected with the input coil of the SQUID on the sticks, respectively. Both of them are clamped between the niobium stick and niobium washers with brass screws. All parts of the setup are shielded by superconducting niobium. The signal from the SQUID is transfered to the SQUID controller. The output signal from that device is connected to a spectrum analyzer[4].

This design ensures that the noise source is electrically grounded and is thermally connected to the mixing chamber. So it can be cooled to the lowest attainable temperatures. Therefore the problem of hot electron effects in the metal can be avoided. In addition,

---

[4]Model SR 770 FFT Network Analyzer, manufactured by Stanford Research Systems, Inc., California, USA.

there is no electrical connection from the pickup coil to the sensor as the noise is measured inductively.

Results and interpretation

Figure 4.10 shows several curves of magnetic Johnson noise, which are taken with the spectrum analyzer at different temperatures in the frequency range from 10 Hz to 500 Hz. For the fit (the solid line), the 50 Hz noise is cut out. The fitting lines follow the formula [Fle03]

$$\sqrt{S_\Phi(f)} = \frac{\sqrt{S_\Phi}}{\sqrt{1 + \left(\frac{f}{f_c}\right)^\alpha}} \, . \tag{4.9}$$

$\sqrt{S_\Phi(f)}$ is the magnetic flux noise at frequency f. $\sqrt{S_\Phi}$, α and f_c are the variable parameters for the fit. $\sqrt{S_\Phi}$ is the fitted magnetic flux noise of the plateau range, which is shown in the figure. f_c is the bandwidth of the flux noise, at which the magnetic flux noise is 3 dB of the flux noise in dc frequency range. As can be seen from figure 4.10, the noise level increases with increasing temperature. The square of magnetic flux noise should follow $S_\Phi \propto T$ as predicted by (4.8).
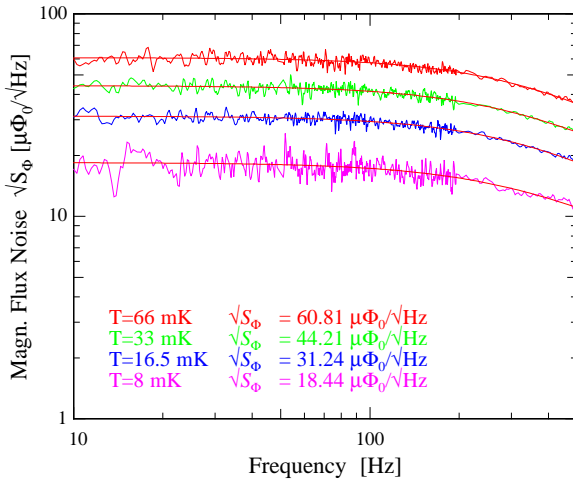

Fig. 4.10: The spectrum of the magnetic flux noise dependence on the temperature in the range from 10 Hz to 500 Hz. The data is fitted with (4.9). The relevant values of the magnetic flux noise for the plateau region at different temperatures are shown.

Figure 4.11 shows the square of magnetic flux noise as function of the temperature measured with the carbon thermometer. Qualitatively the values of S_Φ depend linearly on the temperature, which is indicated by the fitting line. However, there is a deviation between the experimental data and the fitting line below 15 mK. In figure 4.12 the temperature region below 20 mK is plotted. Towards lower temperature the deviation is clearly visiable and increases with decreasing temperature.

In view of the linear dependence of the noise thermometer, the deviation in figure 4.12 and the additional kink in the calibration curve in figure 4.6, the temperature scale of the data in our inductive measurement for double-paddle oscillator should be re-calibrated below 15 mK.
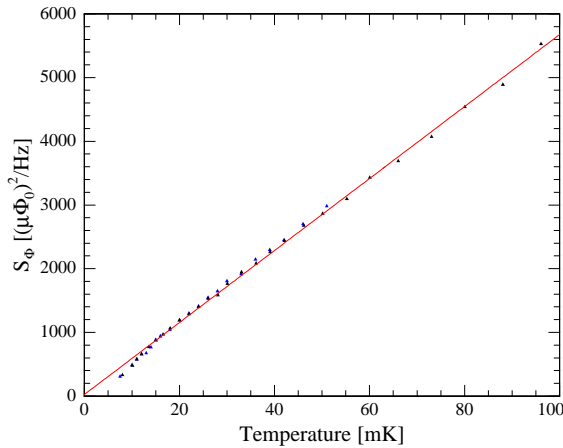
Fig. 4.11: Square of the magnetic flux noise as function of temperature measured with the carbon thermometer. The solid line is a linear fit from 15 mK to 100 mK.
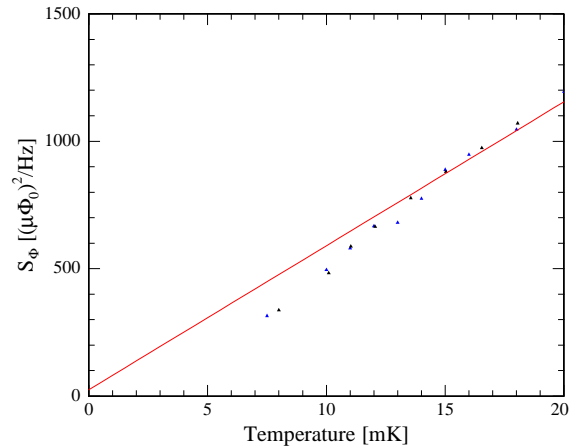
Fig. 4.12: Zoomed temperature region of figure 4.11. The offset at absolute zero is due to the SQUID white noise.

4.4   Conventional capacitive detection technique

In this section the conventional capacitive experimental setup for the excitation and detection of double-paddle oscillator is presented.

4.4.1   Conventional experimental setup

Figure 4.13 shows a schematic of a holder for a double-paddle oscillator. The paddle is clamped at its foot between two copper blocks with two brass screws. The bigger block is screwed into the sample holder, which is directly mounted under the mixing chamber of the cryostat (see section 4.1). The whole sample holder is made of copper because of its good thermal conductivity at low temperatures. The electrostatic excitation and detection is brought about with two electrodes, which are mounted behind the wings of the paddle and seperated by a copper shield. They are approximately at the same height as the wings. Each electrode and the paddle form the two sides of a capacitor. Therefore a silver film is evaporated onto the glass sample at the side facing the electrode. To provide for sufficient thermalization [Bur99] and to avoid the influence on the elastic properties of the paddle, the thickness of the silver film is about $1\,\mu$m for the presented experiments.

To get an expression for the measured signal one can start with the capacity between the electrode and the paddle surface

$$C_{\mathrm{e/d}} = \frac{\epsilon_0 S}{x_{\mathrm{e/d}}} \ . \tag{4.10}$$

The subscript indexes e and d stand for the excitation and the detection. S is the effective area of the capacitor, $x_{\mathrm{e/d}}$ is the distance between the electrode and the paddle. The

typical distance is about $100\,\mu$m and the area of the electrode surface is about $0.2\,\text{cm}^2$. The resulting capacity is around several pF.

If an excitation voltage $U(t) = U_0 \cos(\frac{1}{2}\omega t)$ is applied to one of the electrodes and the vibration amplitude is sufficiently small, the force between the plates of the capacitor is

$$F(t) = \frac{1}{2}\,C_\text{e}\frac{U(t)^2}{x_\text{e}} = \frac{1}{4}\,C_\text{e}\frac{U_0^2}{x_\text{e}}\left(1 + \cos\omega t\right)\,. \tag{4.11}$$

The frequency of the paddle is twice the excitation frequency.

The readout with the conventional technique is also done capacitively. The capacity on the detection side is modulated by the vibration of the paddle. With the oscillation amplitude $\xi(t)$ one gets

$$C(t) = C_\text{d}\frac{1}{1 - \xi(t)/x_\text{d}} \approx C_\text{d}\left(1 + \frac{\xi(t)}{x_\text{d}}\right) \tag{4.12}$$

according to $\xi(t) \ll x_\text{d}$, i.e. the displacement of the paddle due to the force can be neglected compared to the gap between electrode and paddle.

By applying a bias voltage U_B of about $300\,\text{V}$ over a high resistor $R \approx 400\,\text{M}\Omega$, the change of the capacity is transformed to a voltage. If one takes into account the capacity of the cables C_L, which is around several hundred pF, this alternating voltage can be written as [Ber75]

$$U_\text{d}(t) = U_\text{B}\frac{\xi(t)}{x_\text{d}}\frac{C_\text{d}}{C_\text{d} + C_\text{L}}\frac{\omega R(C_\text{d} + C_\text{L})}{\sqrt{1 + [\omega R(C_\text{d} + C_\text{L})]^2}}\,. \tag{4.13}$$

Fig. 4.13: Schematics of the holder and the double-paddle oscillator with the excitation and detection electrodes. The oscillator is clamped between two copper blocks [Lay00].

For the frequencies up to $15\,\mathrm{kHz}$ used in our experiments, one can set the last factor to unity. As $C_\mathrm{L} \gg C_\mathrm{d}$, (4.13) simplifies to

$$U_\mathrm{d}(t) = U_\mathrm{B} \frac{\xi(t)}{x_\mathrm{d}} \frac{C_\mathrm{d}}{C_\mathrm{L}} = U_\mathrm{B} \frac{\xi(t)}{x_\mathrm{d}^2} \frac{\epsilon_0 S}{C_\mathrm{L}} \quad . \tag{4.14}$$

The detection voltage U_d is proportional to the bias voltage U_B and the displacement of the paddle ξ during the vibration. Furthermore, U_d is inversely proportional to the square of the distance between the paddle and the detection electrode. This emphasizes that the adjustment of the electrode-paddle distance plays a crucial role for the amplitude of the detection signal. Corresponding to the typical detection voltage, which is in the range of $\mu\mathrm{V}$, one can get from (4.14) that the amplitude of the oscillation ξ is of the order of nm.

Figure 4.14 shows the schematic of the electronic setup of the conventional double-paddle excitation and detection. The synthesizer [5] produces an ac-voltage with the frequency $f/2$ at the excitation electrode, in order to induce the vibration of the paddle at frequency f. The detection voltage U_d with frequency f is connected to a lock-in amplifier[6]. A capacitor C_B acts as a filter for the constant voltage U_B. The lock-in amplifier couples the detection signal and the reference signal in the so-called $2f$-mode, i.e. only the frequency which is twice the reference frequency is detected. Any other frequency is suppressed. In particular, the electrical cross talk of the excitation voltage with the frequency $f/2$ from the excitation to the detection electrode is filtered in this way. In addition, a copper piece between the electrodes is mounted in order to minimize the electomagnetic interaction of the electrodes.

The lock-in amplifier provides two signals, $X = A\cos\Phi$ and $Y = A\sin\Phi$. A is the amplitude of the input signal and Φ is the phase difference compared to the reference signal. The amplitude A can be calculated by $A = \sqrt{X^2 + Y^2}$. When the distance of the excitation side between the wing of the paddle and the electrode shows the maximal distance, the distances of the torsional modes between the other wing and the detection electrod shows a minimum. In contrast, for the bending and the flapping modes, the distance shows a maximum. This behaviour results in a phase shift of π between the bending and the torsional modes. This phase shift is used to distinguish between torsional and bending modes. In addition, the capacitor C_B causes another $\pi/2$ phase shift for the signals X and Y. This additional phase can be compensated in the lock-in amplifier and is not considered any further in the following.

The two measured signals are transfered into an analog-digital converter (A/D card) of a computer, which stores the data and realizes a control for the excitation frequency on the resonance of the oscillator. Therefore the computer is connected by an IEC-Bus with the frequency generator. A suitable variable for the control is X: When the paddle is driven at one resonant frequency, the value of $X = A\cos\Phi$ is zero, as the oscillation has a phase delay of $\pi/2$ with respect to the driving force. The computer regulates the

---

[5]Philips PM5191 programmable synthesizer / function generator 0.1 mHz – 2 MHz, Philips GmbH, Hamburg, Germany.

[6]Ithaco Dynatrac 393 lock-in amplifier.
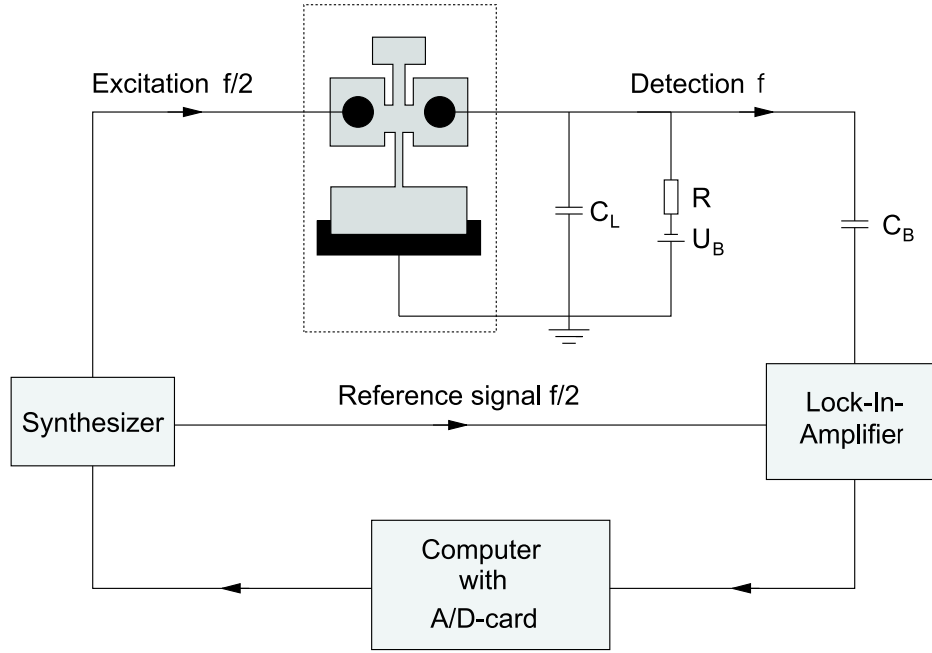
Fig. 4.14: Schematics of the electronic measurement system. The dotted line symbolizes that the part is inside the cryostat.

excitation frequency $f/2$ at each step i in the servo loop by a PID (proportional, intergral, differential) algorithm in accordance with

$$\left.\frac{f}{2}\right|_i = \left.\frac{f}{2}\right|_{i-1} + P X_\mathrm{r} + I \int_{-\Delta t}^{0} X_\mathrm{r}\,\mathrm{d}t + D \frac{\mathrm{d}X_\mathrm{r}}{\mathrm{d}t} \; . \qquad (4.15)$$

The values for P, I and D depend sensitively on the quality Q of the considered mode. With this PID controlling algorithm, the temperature dependence of the relevant parameters internal friction and relative change of sound velocity can be easily determined in the experiment.

4.4.2 Principle of the capacitive measurement

The relative change of sound velocity $\delta v/v$ can be determined directly via the shift of the resonant frequency f_0. From (3.1) one can get $f_0 \propto v$, and by neglecting thermal expansion, one gets

$$\frac{\delta f_0}{f_0} = \frac{f_0(T) - f_0(T_0)}{f_0(T_0)} = \frac{v(T) - v(T_0)}{v(T_0)} = \frac{\delta v}{v} \; . \qquad (4.16)$$

T_0 is an arbitrary reference temperature.

The internal friction can be measured with two different experimental methods. Elastic strain energy can be stored in a mechanical oscillator. In solids, absorption mechanisms occur, which cause an energy dissipation, so that the oscillation amplitude $A(t)$ will decay
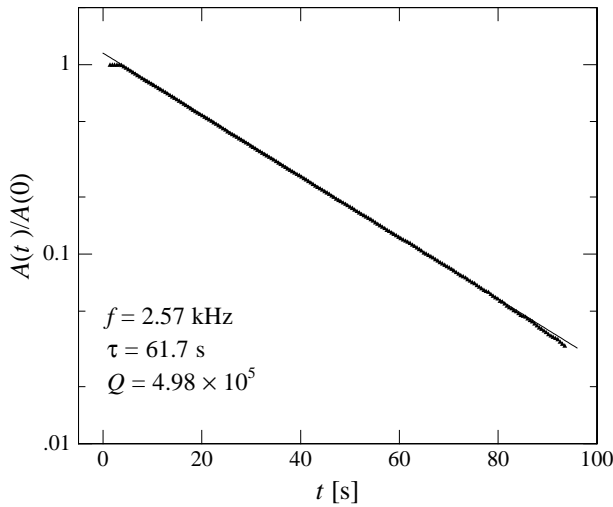
Fig. 4.15: Free amplitude decay of an a-SiO$_2$ paddle at room temperature [Bur99]. After 2 s the excitation is switched off. The fitting line is given by (4.17).

with a certain time constant τ:

$$A(t) = A_0 \mathrm{e}^{-t/\tau} \ , \tag{4.17}$$

as shown in figure 4.15. For small damping the internal friction Q^{-1} is given by [Sku54]

$$Q^{-1} \approx \frac{1}{\pi f_0 \tau} \ . \tag{4.18}$$

where f_0 is the resonant frequency and τ is the decay time.

After switching off the excitation voltage, the time constant τ can be gained from the exponential decay of the amplitude. Then the internal friction can be calculated with (4.18).

Another method is to take a resonance curve of double-paddle oscillator. In figure 4.16 the signals A, $A \sin \Phi$ and $A \cos \Phi$ depending on the excitation frequency f are shown in an interval around the resonance frequency f_0.

The frequency dependence of the amplitude is given by a Lorentzian curve

$$A \propto \frac{Q}{\sqrt{(f_0^2 - f^2)^2 Q^2 + f_0^2 f^2}} \overset{(f \approx f_0)}{\approx} \frac{Q}{f_0 \sqrt{4Q^2(f_0 - f)^2 + f_0^2}} \ , \tag{4.19}$$

f_0 is the resonance frequency of the undamped oscillator.

With the full width at half maximum Δf the quality is given by

$$Q = \frac{f_0}{\Delta f} \ . \tag{4.20}$$

Δf is the frequency difference of the full width at half maximum. In this case one has to take the full width at half maximum at $A_0/\sqrt{2}$.

Both methods produce results within a difference of approximately 1-5%. However, the measurement of the resonance curves exhibits a series of advantages. The nonlinear effect can easily be detected by a tilt of the resonance curve (see section 3.3). In addition an
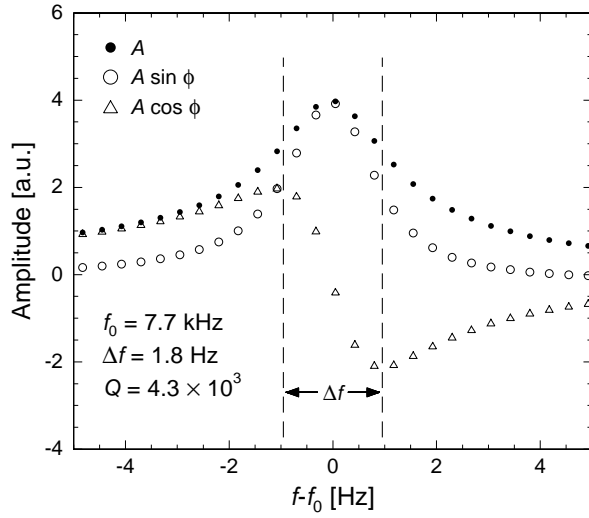
Fig. 4.16: Resonance curve of an a-SiO$_2$ paddle at $100\,$mK. The signals A, $A\sin\Phi$ and $A\cos\Phi$ are plotted as function of the resonance frequency. The full width at half maximum Δf of the Lorentzian is related to the quality factor Q of the oscillator by (4.20).

amplitude offset or an auxiliary phase shift caused by the electronic of the setup can be corrected.

However this method is time-consuming. A mode with $Q = 3 \times 10^5$ exhibits at a frequency of $14\,$kHz a settling time of $\tau \approx 7\,$sec. Taking a typical resonance curve with 50 points lasts about $30\,$min, since one has to wait for a transient time of 3τ after each frequency change.

# 5. Inductive detection technique for mechanical oscillators

In this chapter the experimental setup based on an inductive detection and dc-SQUID readout technique is introduced. At first the setup and the principles of the inductive readout technique are described in detail. In the following three sections we characterize the electronics with regard to its frequency bandwidth and discuss different noise contributions, resulting in the resolution of the SQUID based detection. A comparison between the inductive detection method and the Allegro gravitational wave detector is shown. In the last section, a comparision of capacitive and inductive measurement is given concluding in the advantages of the inductive readout technique.

5.1 Experimental setup

The resonance curves as well as the temperature dependence of sound velocity presented in section 3.3 show that the response of the mechanical oscillator becomes nonlinear when the excitation voltages are increased at low temperatures. This is due to the fact that the strain energy of the tunneling system is of the order of the thermal energy [Cla94]. To measure the temperature dependence of sound velocity and internal friction in the *linear* regime the excitation has to be sufficiently small and, as a result, the sensitivity of detection has to be as high as possible. So we set up a new inductive detection technique based on a commercial dc-SQUID. The application of SQUIDs is a well-established approach to detect very small displacements. They are used for example in gravitational wave detectors [Ric97] or in measurements of the redshift of γ-radiation in the gravitational field of the earth using Moessbauer spectroscopy [Iko91].

5.1.1 Principle of the inductive detection

Figure 5.1 shows the principle of the detection system for the inductive measurement. The setup consists of a number of electronical and mechanical pieces which are mounted inside a ^{3}He-^{4}He dilution refrigerator on platforms of different temperature (figure 4.1). The SQUID is fixed thermally and mechanically to the 1 K-pot and therefore has a working temperture of about 1.6 K. The double-paddle oscillator to be measured, as well as the pickup coil and a field coil, which is used to produce a small magnetic field around the head of the paddle, are mounted on the coldest platform of the refrigerator (mixing chamber). These parts are located inside a can made of aluminum, which is superconducting at the temperatures of interest and shields the sensitive detection circuit from external magnetic stray fields. During the measurement the field coil produces a magnetic field of a few Gauss in the vicinity of the head of the paddle. On the other hand the head of the paddle is
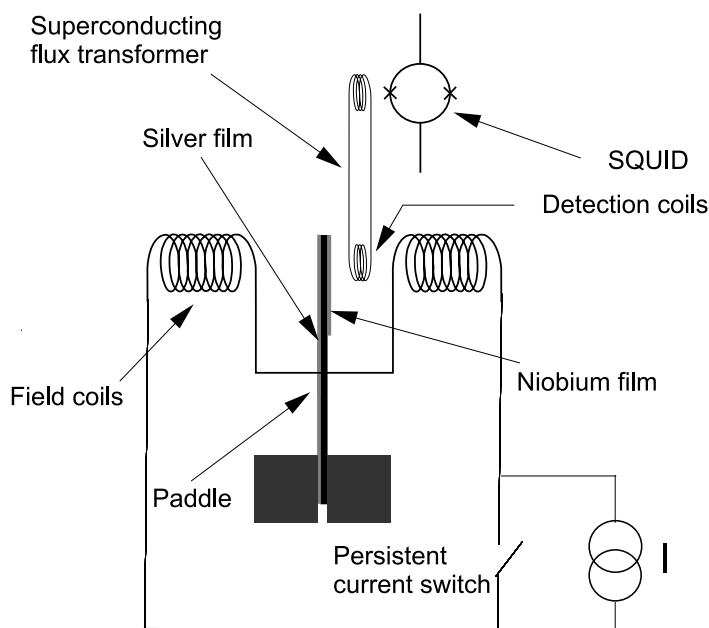
Fig. 5.1: Principle of the SQUID detection system with a persistent current switch. The electrodes for the capacitive excitation and detection is not shown here.

covered with a 200 nm thick niobium film[1], which is superconducting at the temperatures of interest and expels magnetic flux from the volume of the double-paddle oscillator. As discussed for the silver film a thickness of 200 nm should be small enough not to influence the mechanical propertics of the glass oscillator noticeably. While oscillating, the head of the paddle with the superconducting film moves within an outer permanent magnetic field. Due to the superconductivity of niobium and the resulting diamagnetism, the magnetic field produced by the field coil is pushed out by the paddle head. Therefore the movement of this diamagnet within an outer magnetic field changes the magnetic field distribution in the surroundings. This leads to clear changes of the magnetic flux through the detection coil. The detection coil is placed between the paddle head and one of the field coils. The signal which is picked up by detection coil is transformed to the SQUID by a flux transformer. Here one makes use of the conservation of magnetic flux in a superconducting circuit. The detection coil forms a completely superconducting circuit together with a second coil (input coil) which has rather large mutual inductance to the SQUID. Accordingly any change of flux in the detection coil results in a change of flux in the SQUID. This is true even at zero frequency. Best flux coupling is usually achieved if the inductances of the two coils are equal.

In order to produce a constant magnetic field the field coil is equipped with a so-called *persitent current switch*. During the measurement the field coil is run in a persistent current mode without active current supply in order to produce a low noise magnetic field. Therefore the persistent current switch made of superconducting wire is placed in parallel to the superconducting field coil. This superconducting shunt can temporarilly be driven as normal conductor by a resistive heater attached to it.

Figure 5.2 shows the schematics of the complete electronic measurement system of the double-paddle oscillator. This design combines the inductive detection technique with the

---

[1]The superconducting transition temperature T_{c} of niobium is about 9.3 K.
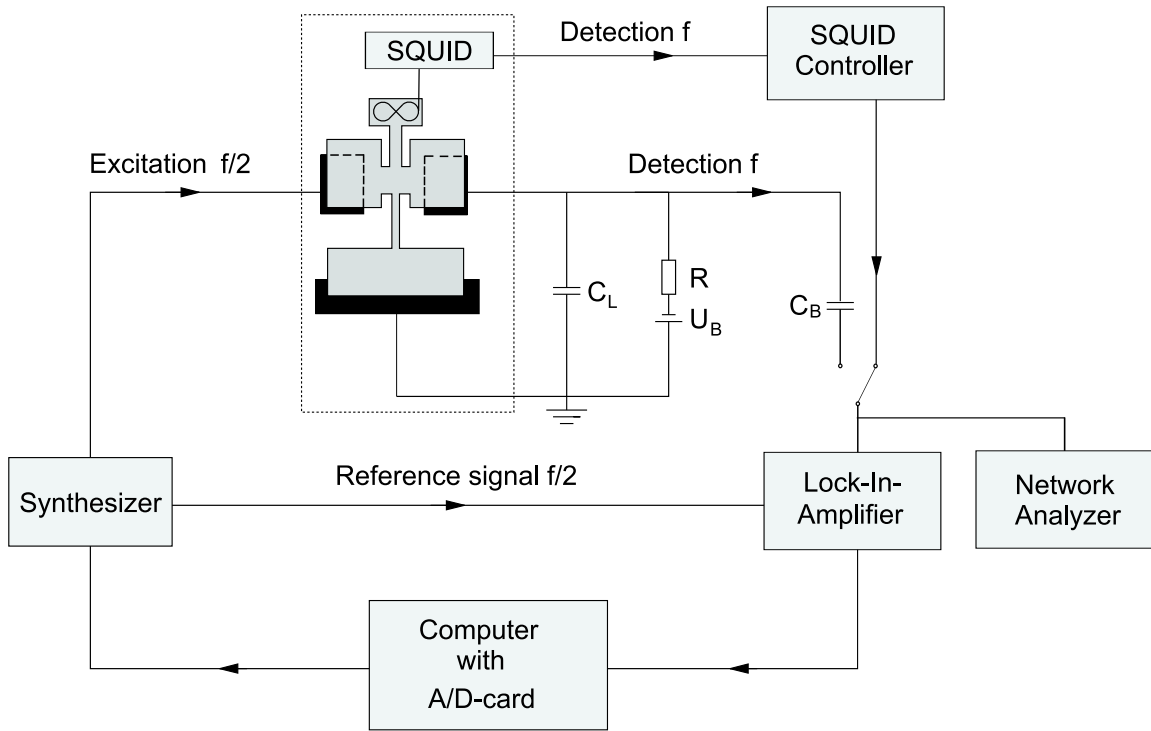
Fig. 5.2: Schematics of the new electronic measurement system. The dotted line surrounds the parts which are inside the cryostat. The two blocks behind the paddle represent the excitation and detection electrodes.

capacitive detection method. In this way the comparison of the two techniques can be carried out under the same experimental conditions. The pickup coil for the inductive readout is next to the head of the paddle and is wound like a gradiometer with two coils as "∞" shape, which is in first order sensitive to the torsional modes and will be described detailly in the following section. The two blocks behind the wings of the paddle are the counter electrodes which are used for the capacitive excitation and detection. They are on the other side of the paddle compared to the pickup coil, in order to minimize the electromagnetic influence to the inductive readout. The two electrodes are placed next to the corners of the paddle's wings, since this is where the largest displacement of the wing for the anti-symmetric torsional modes occurs. Thus, a rather large signal can be gained in the capacitive detection technique, which can be compared to the inductive detection result.

In the inductive measurement the frequency-locked-loop circuit, which regulates the driving frequency to stay on resonance, is identical for the inductive and the capacitive measurement. Only the SQUID system is used instead of the ac-voltage at the detection electrode in the capacitive measurement. The signal is transfered via the SQUID to the SQUID controller, which was already discussed in the section on the novel noise thermometer. The SQUID output signal U from the SQUID controller is used as input signal for the lock-in amplifier. At the same time the signal of each readout setup can be fed into a spectrum analyzer to monitor the noise in the frequency range of interest.

5.1.2 Experimental realization

Figure 5.3 shows a photo graph of the experimental setup. The paddle holder is developed for capacitive excitation and detection as well as for inductive readout. The lower part of the paddle holder is made of copper due to its comparably good thermal conductivity. This part includes the electrodes for the conventional capacitive excitation and detection, which is behind the paddle in the photo. The surface area of both electrodes is rectangular and they are placed as shown in figure 5.2.
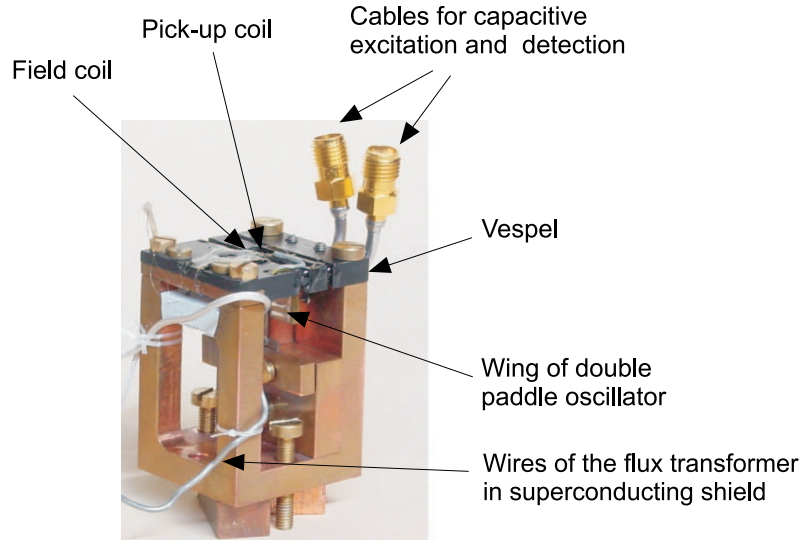
Fig. 5.3: Photo of the experimental setup for the combined detection mechanisms — inductive and capacitive readout technique. The persistent current switch is underneath the vespel part and can't be seen in this photo.

The black part on top of the paddle holder is made of Vespel[2] and is used for the inductive readout, since it is an electrical isolator. If the top part of the paddle holder were made of a metal, such as copper, instead of the electrical isolator, we were afraid that the magnetic field could generate eddy current in the metal during oscillating of the paddle. This eddy current could cause an additional damping on the paddle and influence the experimental results.

Both the field coil and the pickup coil is glued to the Vespel by Stycast 1266[3]. The field coils consists of 100 turns of NbTi/CuNi wire[4] which are wound around each of two graved necks of the Vespel part. The rectangular cross-section area of these necks is 6 mm × 3 mm, which is slightly bigger than the area of the paddle head. The two pickup coils (2.5 mm in diameter), which are shown in figure 5.2, form an "∞" shaped coil with 8 turns on each side. The two coils are wound in opposite sense wired in series and form a planar gradiometer of first order to facilitate the detection of the torsional modes and minimize the random magnetic noise. The distance from the paddle head to the pickup

---

[2]Vespel is a polyimide plastics with low thermal conductivity, which is also an electrical isolator.

[3]Stycast 1266 is a two components epoxy encapsulant and impregnant for the use at low temperatures, which has good moisture resistance, good electrical properties, good impact strength and is manufactured by Emerson and Cuming (Europe) INC., Belgium.

[4]The core of the wire consists of NbTi, which is enclosed by a CuNi matrix. The superconducting transition temperature T_c of NbTi is about 9.8 K.

coils is about 1 mm. The inductance of the pickup coils is designed to have about 1800 nH and matches the inductance of the SQUID input coil. This leads to best signal coupling to the SQUID. The flux tansformer consists of the pickup coil with the input coil of the SQUID. It is a closed superconducting circuit made of niobium wire and is surrounded by a superconducting shielding capillary made of PbSn[5].

The persistent current switch is located underneath the Vespel part and can therefore not be seen in figure 5.3. It consists of niobium titanium wires which are connected to the field coils and an additional 1 kΩ resistor as a heater. Several loops of NbTi/CuNi wire are wrapped around this resistor. When the local temperature T is smaller than the superconducting transition temperature of niobium-titanium T_c, the switch is closed. The current supplied by a current source (indicated by "I" in figure 5.1) is in both the field coil and the NbTi/CuNi wire around the resistor. When we put a current through the resistor of the persistent current switch in order to let $T > T_c$, the switch is open. The whole current applied by the current source has to flow only through the field coil. Then we stop heating and let the local temperature of the switch fall below T_c. After that the current source for the field coil can be switched off. Due to the conservation of magnetic flux completely in the superconducting circuits, a persistent current will continue to flow in the superconducting circuit consisting of the field coil and the superconducting shunt.

5.1.3 Simulation of the flux density for inductive measurement

The flux density distribution produced by the field coils was simulated using the finite element program — "FEMM"[6]. Figure 5.4 shows the simulated flux density distribution in a cross-section through the head of the paddle from the top-view of the inductive experiment. In this simulation the field coil is assumed as four independent long straight cables, which are displayed by the four rectangulars at the corners of this figure and are vertical to this planform. The currents in these four cables have the same absolute values. However, the direction of the current in the two cables on the left side is opposite to the one in the two cables on the right side. The rectangular in the center of the figure means the cross-section of the paddle's head. The four white circinal areas, which are connected by the black lines, stand for the cross-sections of the pickup coil. In this simulation, its influence is negligible due to its small cross-section area. Here the cross-section area of the wire of the pickup coil is exaggerated in order to make them easier to notice. Since the niobium coating on the head of paddle, the field coil and the pickup coil are superconducting at the temperatures of interest, the magnetic field cannot penetrate into them. The relative flux density is colorcoded and the flux lines are also shown in this simulated figure. The red line segment $\overline{MN}$ is used to simulate the distribution of the magnetic field along it, which is from one "field coil" to the other and through the center of one of the pickup coils. The magnetic fields at point M and N are strongest on the line $\overline{MN}$.

---

[5]The superconducting transition temperature T_c of PbSn is about 7.5 K.

[6]Finite Element Method Magnetics (FEMM) is a free software that provides static calculations on low-frequency electromagnetic problems in two-dimensional planar and axial symmetry.
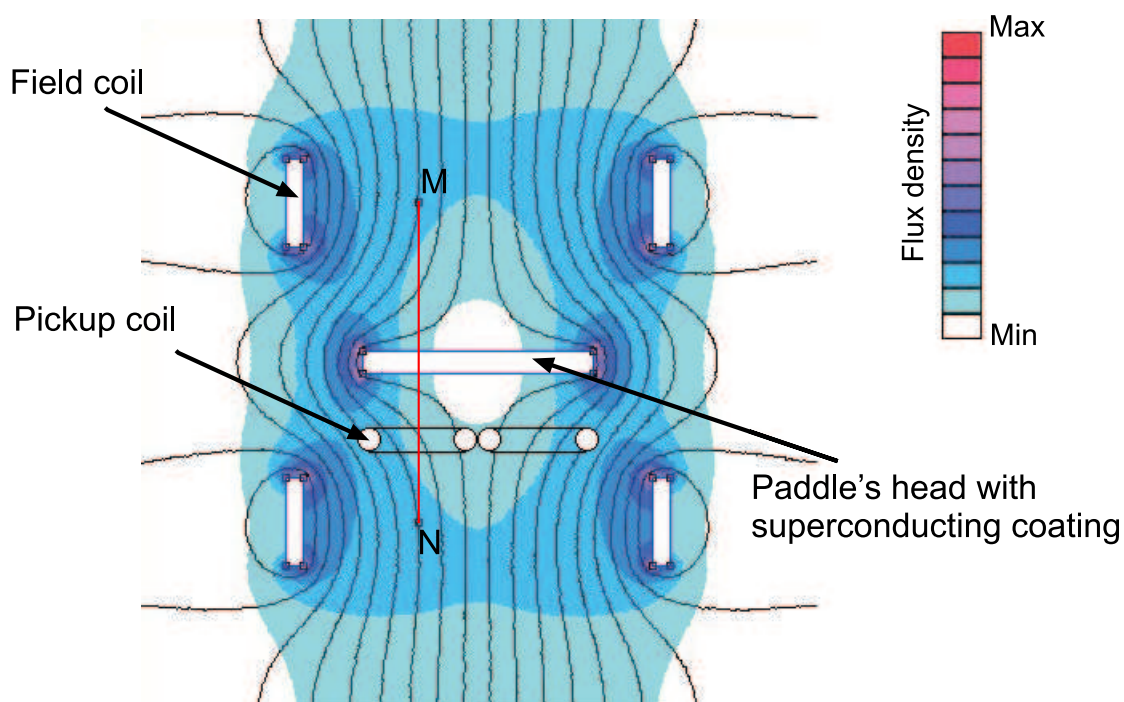
Fig. 5.4: Flux density distribution simulated with a finite element program for a geometry similar to the one used in the experiments. The size of the cross-section of the pickup coil is exaggerated.

Figure 5.5 shows the distribution of the magnetic field along the line segment $\overline{MN}$ when
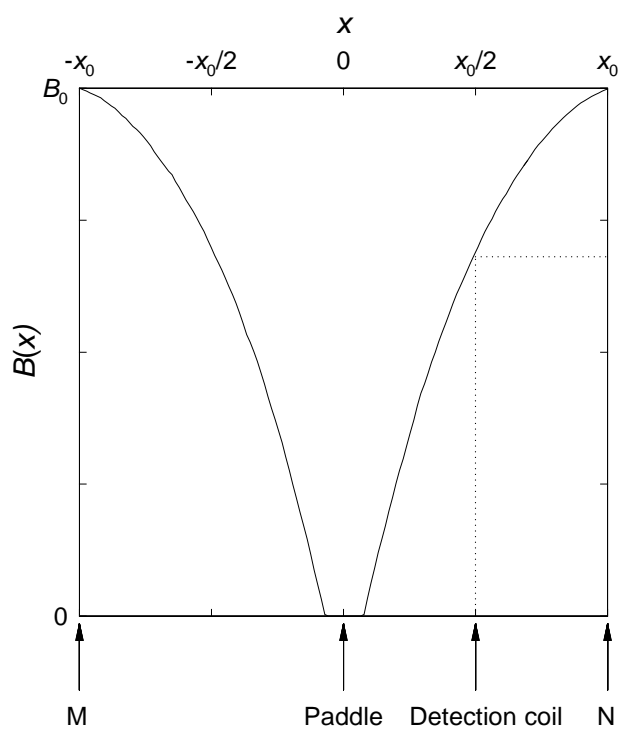
Fig. 5.5: Schematics of the magnetic field distribution along the line segment $\overline{MN}$ when the paddle is at the rest position. The positions of M, N, the paddle and the detection coil are pointed out, respectively.

the paddle is at the rest position. The positions of M, N, the paddle and the detection coil are pointed out, respectively. $2x_0$ is the length of the line segment $\overline{MN}$. The magnetic field has the value B_0 at the points M and N. The field must disappear in the head of the paddle due to the superconducting coating on it.

In figure 5.6 the two simulated curves of the distribution of the magnetic field in the region $x \geq 0$ along the line segment $\overline{MN}$ show a change of magnetic field δB in detection coil caused by the vibration of paddle's head δx. If the displacement of the head vibration is δx from the rest position, a change of the magnetic field at the center of the pickup coil is

$$\delta B = B(x_0/2 + \delta x)|_{\mathrm{P}} - B(x_0/2)|_{\mathrm{P}} = \left.\frac{\partial B}{\partial x}\right|_{\mathrm{P}} \delta x + \left.\frac{\partial^2 B}{\partial x^2}\right|_{\mathrm{P}} \delta x^2 + \ldots\ldots \quad . \qquad (5.1)$$

We find it convenient to treat the derivative of the magnetic field $\partial B/\partial x$ as being proportional to B_0/x_0 and define

$$\delta B = \left.\frac{\partial B}{\partial x}\right|_{\mathrm{P}} \delta x = \mathcal{C}\ \frac{B_0}{x_0}\ \delta x \ , \qquad (5.2)$$

where $\mathcal{C}$ is a unitless coefficient and is about 0.5. In the following this value will be applied for the estimations.
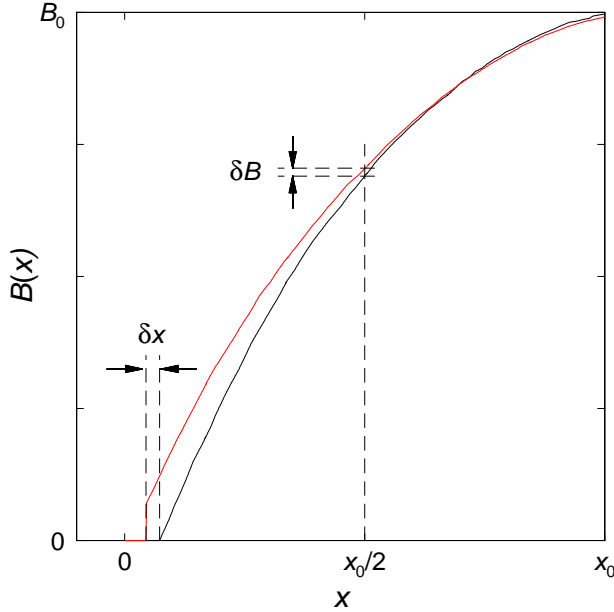
Fig. 5.6: A change of magnetic field δB in detection coil is caused by a displacement δx of the paddle's head. The black curve is the simulated distribution of the magnetic field in the region $x \geq 0$ when the paddle is at the rest position. The red curve is the simulated distribution of the magnetic field when the paddle is at the new position.

5.2   Performance of the electronics in the flux-locked-loop mode

In the readout system of the inductive detection measurement, one of the most important parameters of the SQUID electronics is the slew rate of the flux-locked-loop $\dot{\Phi}_{\mathrm{max}}$. This quantity characterizes the dynamic behaviour of the system and therefore determine the usable working frequency bandwidth f_{max}^* in our measurements.

The slew rate $\dot{\Phi}_{\mathrm{max}}$ is defined as the maximum rate of flux change, which can be applied to the SQUID by the feedback electronics in a mode of stable feedback operation:

$$\dot{\Phi}_{\mathrm{max}} := \left| \frac{\partial \Phi_{\mathrm{F}}}{\partial t} \right|_{\mathrm{max}} . \tag{5.3}$$

If the experiment produces flux changes $\Phi_{\mathrm{I}}(t)$ at smaller rate the feedback electronics is able to compensate these by applying the appropriate feedback flux $\Phi_{\mathrm{F}} = -\Phi_{\mathrm{I}}$ of opposite sign. Due to the flux modulated readout of the SQUID discussed in section 4.2, the input signal bandwidth is limited to a fixed value f_{max}. According to the discussion in [Cla04], this limit in bandwidth results in a maximum slewrate, which is given by

$$\dot{\Phi}_{\mathrm{max}} = 2\pi \, f_{\mathrm{max}} \, \Delta\Phi_{\mathrm{lin}} \, , \tag{5.4}$$

where $\Delta\Phi_{\mathrm{lin}}$ is the flux range around the working point, where the flux-voltage characteristics of the SQUID is linear in reasonably good approximation.

It is worth to notice that there are two criteria which determine the maximum frequency f_{max}^*, below which the experiment can be operated. On the one hand the frequency should not be larger than the bandwidth of the electronics[7], f_{max}. On the other hand the signal to be measured gets distorted significantly if the occuring rates of flux change exceed the maximum slew rate. For sinusoidal signals of amplitude Φ_{S} the usable bandwidth is limited to

$$f_{\mathrm{max}}^* = \frac{\dot{\Phi}_{\mathrm{max}}}{2\pi \, \Phi_{\mathrm{I}}} \, . \tag{5.5}$$

With the typical value of $\Delta\Phi_{\mathrm{lin}}$ is $\Phi_0/4$ one gets

$$f_{\mathrm{max}}^* = \frac{\Phi_0}{4 \, \Phi_{\mathrm{I}}} \, f_{\mathrm{max}} \, . \tag{5.6}$$

This dependence of the usable bandwidth on the amplitude of the signal can be demonstrated experimentally.

For this measurement we connected a network of resistors and inductors to the input coil of the SQUID, which allowed to generate magnetic flux in the SQUID. The induced magnetic flux was proportional to the voltage at the input terminals of the network. The bandwidth of the network was limited to about 1 MHz by high frequency filters in order to suppress the coupling of signals at radio frequencies to the SQUID.

Figure 5.7 shows the amplitude of the response of the SQUID electronics in flux-locked-loop mode as function of frequency for six different amplitudes of the harmonic test signal.

---

[7]iMAG LTS Multi-Channel SQUID system by Tristan Technologies, San Diego, California, USA.
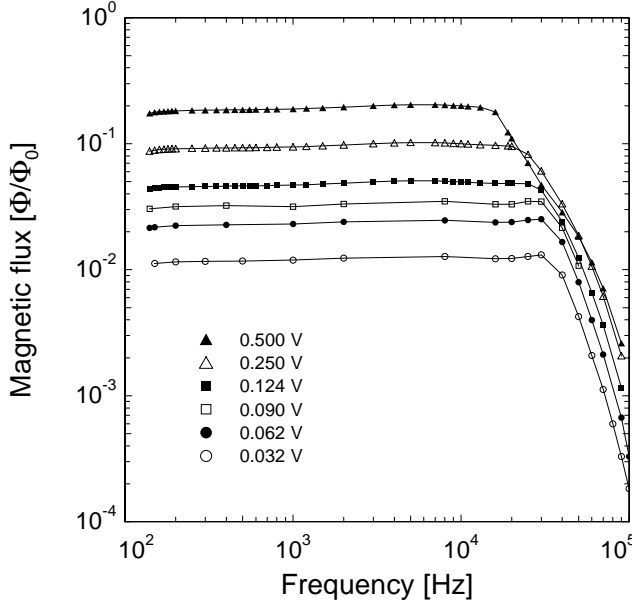
Fig. 5.7: Input magnetic flux amplitude in the SQUID as function of frequency dependent on the input amplitude. The different symbols stand for different flux amplitudes in the SQUID.

In the limit of small flux amplitudes the usable bandwidth is approximately 40 kHz and is limited by the bandwidth of the electronics, $f_{\max}^* = f_{\max}$. Towards larger signal amplitudes, the usable bandwidth decreases, $f_{\max}^* \geq f_{\max}$, due to the finite slewrate of the feedback electronics, as discussed above. This also means an important restriction to the measurement of the acoustic properties of the double-paddle oscillator. In our experiment five of the modes of the paddle have the resonance frequencies between 1 kHz and 14 kHz. From figure 5.7 we can see that the detected flux amplitude at 14 kHz should be smaller than 100 mΦ_0 to avoid the large additional phase shifts and the artifact caused by the electronics. The restriction is less severe for the resonances at lower frequency. But the small amplitude of $\Phi_I = 30$ mΦ_0 is already sufficient for a high resolution measurement, because the rms flux noise of the SQUID in a bandwidth of 1 Hz is only of the order of 5 $\mu\Phi_0$.

A change of magnetic flux in the pickup coil $\delta\Phi_P = A\delta B$, where δB is given by (5.2) and A is the total cross-section area of the detection coil.

From section 4.2.3, the flux change from the input coil into the SQUID can be written as

$$\delta\Phi_I = \frac{M_{IS}}{L_P + L_L + L_I}\,\delta\Phi_P \;. \tag{5.7}$$

So $\delta\Phi_I$ in our experiment is given by

$$\delta\Phi_I = \frac{M_{IS}}{L_P + L_L + L_I}\,A\,\frac{\partial B}{\partial x}\bigg|_P\,\delta x \;\propto\; \frac{B_0}{x_0}\,\delta x \;. \tag{5.8}$$

From (5.8) we know that one should choose the reasonalbe value of the magnetic field B_0 with a displacement amplitude δx in order to generate an appropriate flux amplitude in the SQUID.

## 5.3 Noise contributions in inductive experiments

In this section the noise contributions of the inductive detection setup are described. At first the contributions of the white noise and the $1/f$ noise are discussed in the experimentally relevant frequency range. Then contributions from mechanical vibrations at discrete frequencies are presented.

The experimental data shown in this section were acquired by a Model SR 770 FFT spectrum analyzer, which was connected to the output signal of the SQUID. The temperature of the SQUID is always about 1.6 K.

5.3.1 Frequency spectrum of the SQUID signal

SQUID signal with open and closed input circuit

Figure 5.8 shows the experimental magnetic flux noise in the SQUID as function of frequency from 10 Hz to 100 kHz. The two displayed spectra were measured for two different experimental setups. The red spectrum represents the noise of the bare SQUID, since the detection coil was not connected to the input coil of the SQUID in this measurement. The black spectrum corresponds to the SQUID signal with a closed input circuit, which consists of the pickup coil of the inductive measurement and the input coil of the SQUID. The temperature of the pickup coil of the inductive readout setup is 4.2 K and the paddle is not driven.
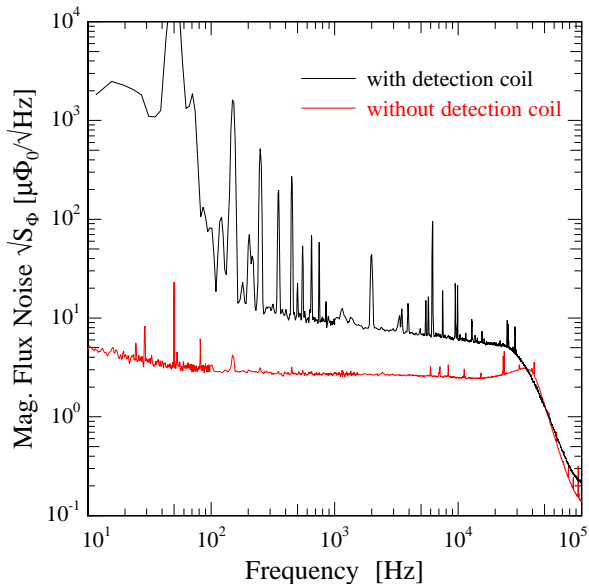
Fig. 5.8: Magnetic flux noise of the SQUID as function of frequency. In both measurements the temperature of the SQUID is about 1.6 K. The input circuit is open (red spectrum) and closed (black spectrum). The input coil of the SQUID in the closed loop is connected with the pickup coil of the inductive detection setup. The pickup coil is at 4.2 K.

In the spectrum with the open input circuit, the SQUID noise is dominated by the $1/f$ noise at low frequencies. The white noise between 200 Hz to 15 kHz is about 2.5 $\mu\Phi_0/\sqrt{\text{Hz}}$, which consists of two parts: Johnson noise in SQUID circle and the noise in the flux-locked-loop. The peak at about 40 kHz is due to the frequency response of the flux-locked-loop

electronics. In addition, some noise peaks at discrete frequencies are observed, which are mostly due to electromagnetic pickup and ground loops.

In the spectrum with the closed input circuit, only earth magnetic field is frozen in the superconducting aluminium can during the cooling down process. The whole noise level rises clearly. As the detected frequency range in our double-paddle oscillator experiment is between 1 kHz and 15 kHz, the influence of the $1/f$ noise is negligible. With increasing frequency the white noise decreases slightly. At 10 kHz the white noise has a value of $6~\mu\Phi_0/\sqrt{\text{Hz}}$, which is about two times larger than the noise of the open input circuit. In addition, many new noise peaks occur. Most of them might come from vibrations of the setup. In the following section, these disturbances at discrete frequencies of the experiment will be discussed in detail.

Temperature dependence of frequency spectrum of SQUID signal

Figure 5.9 shows the magnetic flux noise of our inductive readout setup as function of frequency at different temperatures. The input coil of the SQUID is connected to the pickup coil of the inductive readout setup. The pickup coil is at a temperature of 4.2 K (black spectrum) and 100 mK (red spectrum), respectively. There is no magnetic field generated by the field coil except the earth magnetic field. The paddle is not driven. In the low-frequency range the noise levels of white noise and $1/f$ noise at 4.2 K are higher than the ones at lower temperature. With increasing frequency the difference of the noise levels between the spectrum at 4.2 K and the spectrum at the low temperature decreases. Since the superconducting transition temperature of aluminium is about 1 K, a lot of outer electromagnetic noises are minimized by the aluminium shield when the temperature is below 1 K. Thus, it is shown in figure 5.9 that the noise level of the spectrum at 100 mK is lower than the one at 4.2 K.
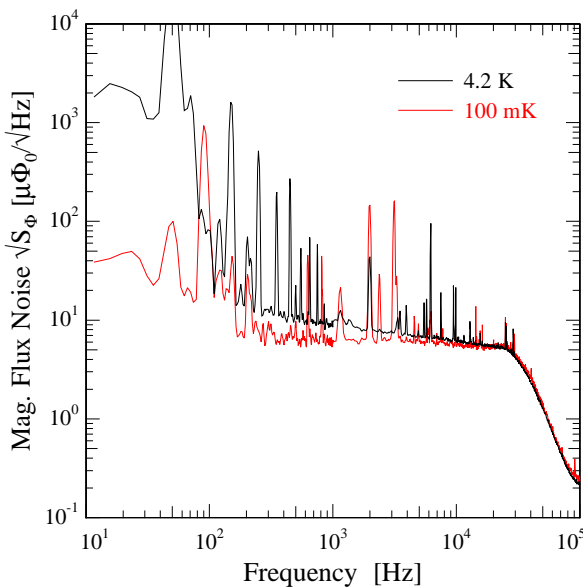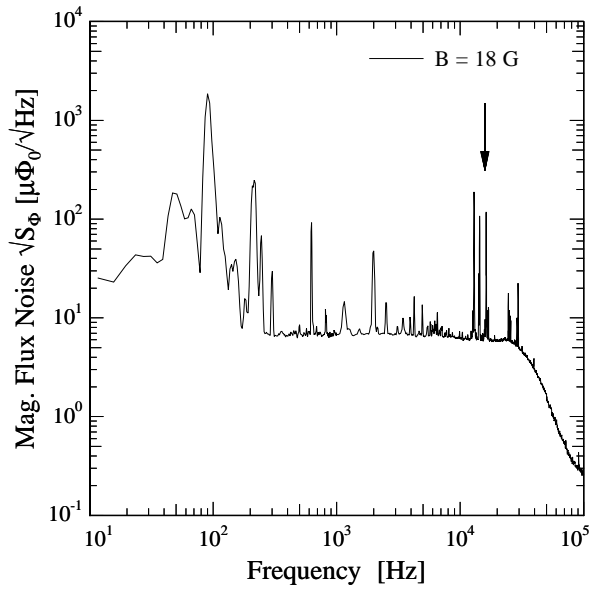

Fig. 5.9: Magnetic flux noise of the SQUID as function of frequency. The input coil of the SQUID is connected to the pickup coil of the inductive measurement. The pickup coil is at a temperature of 4.2 K (black spectrum) and 100 mK (red spectrum), respectively.

5.3.2   Disturbances at discrete frequencies

In figure 5.9 disturbances at discrete frequencies are clearly visible. In order to find the sources of these noise peaks, several experiments were done.

Figure 5.10 shows the magnetic flux noise of the SQUID as function of frequency. The input coil of the SQUID is connected to the pickup coil of the inductive readout setup. The setup is at a temperature of 100 mK and the field coil is in persistent current mode, producing a magnetic field of 18 Gauss. The paddle is not driven.

Fig. 5.10: Magnetic flux noise of the SQUID as function of frequency with the closed input coil of the SQUID, which is connected with the pickup coil of the inductive measurement at 18 Gauss. The pickup coil is at 100 mK.

Compared to the spectrum in figure 5.9 several peaks between 10 kHz to 20 kHz increased significantly. Since these peaks are close to the AT1 and AT2 modes of our glass paddles, they can strongly influence the signals of the AT1 and AT2 modes. So we give this regime more attention. When we change the magnetic field generated by the field coil, the amplitudes of these peaks show a strong dependence on the magnetic field. However, when the temperature is changed, there is no the temperature dependence of the frequency of these noise peaks. With the capacitive detection no resonance peak can be detected at these frequencies. Thus, we conclude that these noise peaks are not eigenfrequencies of the paddle.

Another experiment can be accomplished with a loud-speaker, in order to find the source of these noise peaks. The loud-speaker is connected to a frequency synthesizer and the output signal from the SQUID is monitored with the spectrum analyser. When we place the loud-speaker next to the cryostat and adjust the frequency at the frequency of one of these peaks in the spectrum, the peak increases significantly. It means that these discrete peaks in the noise spectrum are caused by vibrations within the inductive readout circuit, which can be driven mechanically from outside of the cryostat, even by sound waves through the air.

Minimization of disturbances at discrete frequencies

To solve the problem caused by these vibrations several solutions were used. We firstly glued the field coil, the pickup coil and the persistent current switch to the Vespel part using the epoxy Stycast 1266 in order to ensure the field coil is as stable as possible. Secondly, the superconducting wires in the junction box were fixed to the niobium blocks with vacuum grease. The twisted pair of wires, which connect the pickup coil to the input coil of the SQUID to form the flux transformer, were fixed within the superconducting shielding capillary by vacuum grease. The shielding capillary itself was tightly fixed to the cryostat with dental floss.

Figure 5.11 shows the magnetic flux noise of the inductive detection as function of frequency after the field coil, the pickup coil and the flux transformer were fixed. The pickup coil was at a temperature of 100 mK. The field coil was in persistent current mode, producing a field of 30 Gauss. In this spectrum we find the noise peaks from the vibration to be strongly reduced compared to those presented in figure 5.10, even if the magnetic field is stronger than before. In particular the disturbances at discrete frequencies in the frequency range from 10 kHz to 20 kHz are greatly reduced, which increases the resolution of the detected AT1 and AT2 modes.
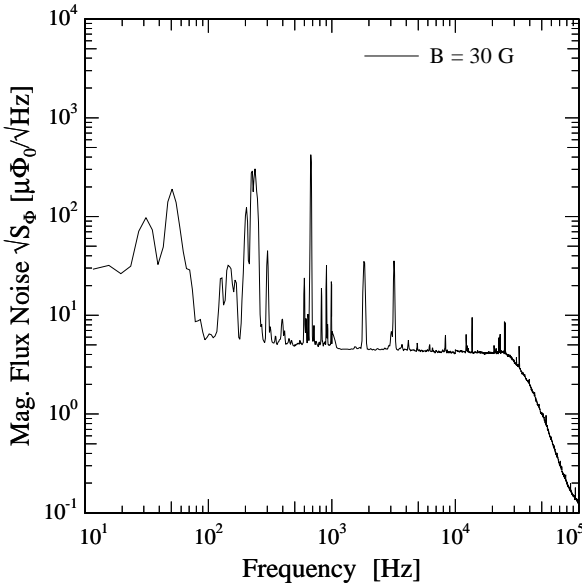
Fig. 5.11: Magnetic flux noise of the inductive detection as function of frequency after the field coil and pickup coil are fixed. The pickup coil of our inductive readout setup is at a temperature of 100 mK and the field coil produces a magnetic field of 30 Gauss.

5.4 Resolution of inductive detection based on SQUID readout

The minimum change of the flux, which can be measured with the SQUID, is limited only by its white noise of $5\ \mu\Phi_0/\sqrt{\text{Hz}}$ in principle; using the lock-in detection and a typical averaging time of 1 s, this flux noise is equal to $\delta_{\text{N}}\Phi_{\text{S}} = 5\ \mu\Phi_0$.

Now we want to estimate the displacement of the paddle δx, which can be resolved at a signal-to-noise ratio $\delta\Phi_{\text{I}}/\delta_{\text{N}}\Phi_{\text{S}}$ of 10 in the presence of the flux noise $\delta_{\text{N}}\Phi_{\text{S}}$ of the SQUID.

We assume the magnetic field to be $B_0 = 20\,\mathrm{G}$, the distance between the two field coils $2x_0 = 5$ mm and the total area of the pickup coil to be $A \approx 100\,\mathrm{mm}^2$ (one considers the 16 turns of the coil). The relevant parameters of the SQUID are listed in table 4.1. Since the flux transformer consists of the twisted pair of wire, its inductance L_L is negligible. Using (5.2) and (5.8) we see that this kind of setup should be able to resolve the displacements as small as $\delta x \approx 10^{-13}\,\mathrm{m}$.

Furthermore the sensitivity can be increased by using higher magnetic fields in principle. But if the magnetic field is too high, on the one hand the bandwidth of the whole inductive readout system will limit the resolution of these detection system. On the other hand eddy currents generated in the silver film as well as in normal metal parts in the vicinity might influence the measured acoustic properties of the paddle by increasing the damping. The eddy current contribution to the internal friction δQ^{-1} is proportional to the square of the magnetic field B [Lay00].

With the capacitive method the noise of the detection signal is typically some $10\,\mathrm{nV}$. In order to measure the oscillation of the paddle, U_d should be bigger than $100\,\mathrm{nV}$. With (4.13) and typical values $C_\mathrm{L} \approx 500\,\mathrm{pF}$, $C_\mathrm{d} \approx 1\,\mathrm{pF}$, $U_\mathrm{B} \approx 300\,\mathrm{V}$ and $x_\mathrm{d} \approx 100\,\mu\mathrm{m}$, the resolution of the displacement can be calculated to be of the order of $10^{-11}\,\mathrm{m}$. Of course, the resolution can be improved in principle by a higher preamplified voltage U_B or a smaller electrode distance to the paddle x_d. However a complex electronic system is required and on the other hand the distance between the electrode and the sample is difficult to adjust in that small distance.

A comparison of the experimental results with both methods is shown in the following section. We can easily find the advantage of the SQUID measurement.

5.5 Comparison with the inductive transformer in Allegro gravational wave detector

Theory of General Relativity predicted the existence of gravitational waves and that the gravitational waves can propagate at the speed of light and represent a time-dependent distortion of the local space and time coordinates. Furthermore the gravitational waves are predicted to be produced by the acceleration of mass. Due to the very weak gravatational field, scientists expect that a stellar collapse to a neutron star or black hole can generate a burst of detectable gravitational radiation, which can exist on the order of milliseconds. The gravitational wave can induce a stress on an elastic body. For a bar antenna, the stress from a gravitational wave causes the ends of the bar to contract and expand. With a sensitive readout technique for the change of the length, the amplitude of the vibrational motion can be detected. Until now several detection techniques have been applied in the different gravitaional wave detectors. In this section we focus only on the transformer of the gravitaional wave detector in Louisiana state university (LSU), which uses an inductive readout method for the displacement of the elastic body, and is compared with our inductive detection technique.

The cryogenic resonant detector in LSU is named *Allegro* which is an abbreviation

of "A Louisiana Low temperature Experiment and Gravitational wave Observatory". It consists of a cryogenic resonant mass detection bar equipped with a superconducting inductive transformer and a dc-SQUID amplifier all cooled to 4.2 K. Figure 5.12 shows the schematics of the Allegro antenna. The upper bar is a large mechanical isolator for decoupling the external vibration, which is about 2100 kg. The lower bar is the elastic body in the Allegro detector, which is a cylinder of aluminum alloy 5056 with 60 cm in diameter, 300 cm in length and a physical mass of 2296 kg. At the end of the detector is the secondary resonator, the so-called *mushroom*. In the zoomed plot of figure 5.12 the mushroom and the inductive transformer are shown. The mushroom resonator is resonant at the same frequency as the aluminium bar, thus making a two-mode system of coupled oscillators (referred to as the "antenna") [Pai74, Sol94]. Facing the mushroom resonator but attached firmly to the Al bar is a superconducting pickup coil carrying a persistent supercurrent. Therefore the distance between the coil and the resonator is changed by the oscillations of the mushroom resonator. Furthermore the oscillations of the mushroom resonator changes also the inductance of the pickup coil, modulating the flux through it. A dc-SQUID converts the changing flux to a voltage [Mau96].
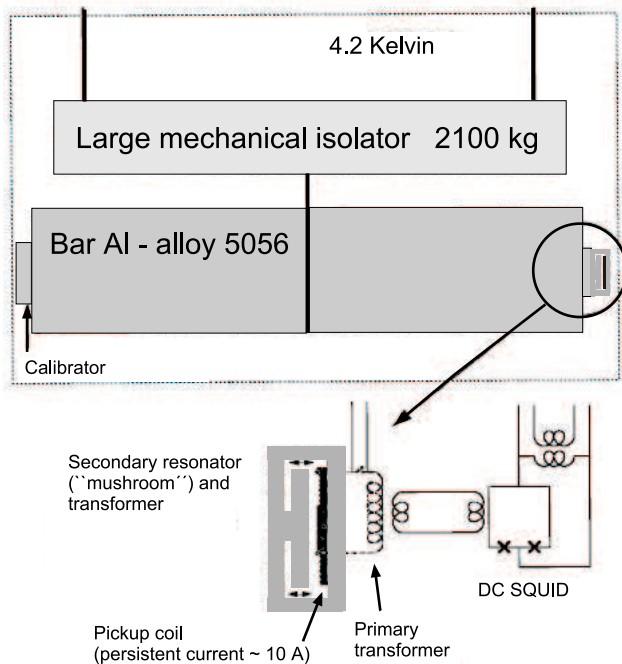
Fig. 5.12: Schematics of the Allegro antenna [Mau96].

Figure 5.13 shows the schematics of the principle for the transformer of Allegro. The mushroom resonator has a superconducting surface. A persistent current exists in the primary tranformer, which generates a constant magnetic field in the pickup coil. Thus the coil near to the mushroom resonator acts as field coil and as pickup coil at the same time. When the mushroom resonator vibrates, the change of self inductance of the superconducting pickup coil is proportional to the change of the gap spacing d between the pickup coil and the mushroom resonator. Relative motion modulates the persistent current in the inductor, since the magnetic flux $L_1 I$ must be conserved. The changing current is
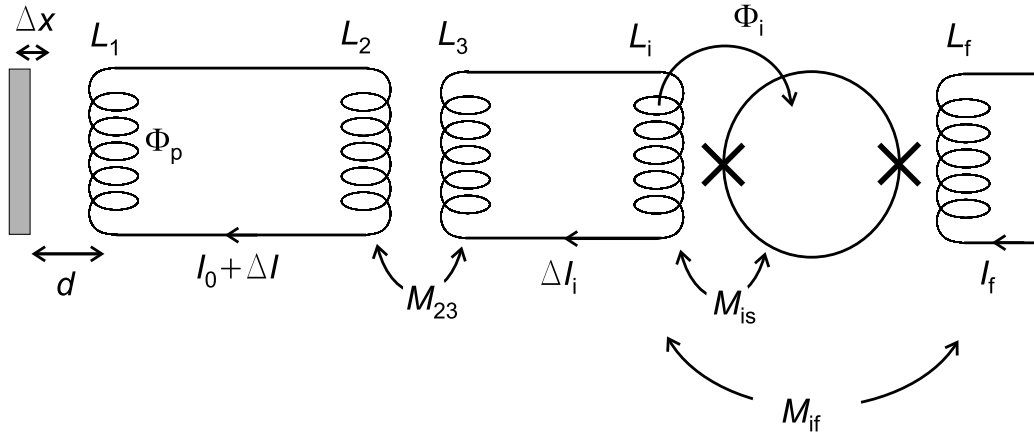
Fig. 5.13: Principle of the Allegro transformer. The quantities indicated are:

Φ_{p} Flux through pickup coil
Φ_{i} Flux from SQUID input coil into SQUID loop
L_1 Inductance of pickup coil in primary tranformer
L_2 Inductance of input coil in primary tranformer
L_3 Inductance of pickup coil in secondary tranformer
L_{i} Inductance of SQUID input coil
I_0 Persistent Current in pickup coil
ΔI Changed current in primary transformer
ΔI_{i} Changed current in SQUID input coil
I_{f} Current in feedback circuit
M_{xy} Mutual inductances
d distance between the mushroom resonator and
Δx displacement of the mushroom resonator

detected via a secondary flux transformer by a dc-SQUID.

In the following, a derivation how the input flux of the SQUID $\Delta\Phi_{\mathrm{I}}$ reflects the displacement of the mushroom resonator Δx is presented and the resolution of this technique is compared with our inductive readout method in this thesis.

At 4.2 K the flux transformer circuit is entirely superconducting. As described in section 4.2.3 and section 5.1.3, any change in the magnetic flux through the pickup coil is compensated by changes in the currents within the transformer and in the feedback circuit, respectively. The flux balance for the primary transformer loop can be written as

$$\Delta\Phi_{\mathrm{p}} + (L_1 + L_2)\Delta I + M_{23}\Delta I_{\mathrm{i}} = 0\,. \tag{5.9}$$

Here the inductance of the wire is negligible. For the geometry discussed here one can assume in good approximation, that the inductance of the superconducting pickup coil is inversely proportional to the gap spacing d between the coil and the superconducting layer on the mushroom resonator. Therefore one finds for the change of flux $\Delta\Phi_{\mathrm{p}}$ in the pickup

coil caused by a displacement Δx of the superconducting mushroom

$$\Delta\Phi_{\mathrm{p}} = -L_1 I_0 \frac{\Delta x}{d}\,. \tag{5.10}$$

The quantities used here and in the following are explained in the caption of figure 5.13.

In the secondary transformer, the flux balance can be written as

$$M_{23}\Delta I + (L_3 + L_{\mathrm{i}})\Delta I_{\mathrm{i}} + M_{\mathrm{if}}\Delta I_{\mathrm{f}} = 0\,. \tag{5.11}$$

The input flux change from the input coil to the SQUID is written as

$$\Delta\Phi_{\mathrm{i}} = M_{\mathrm{is}}\,\Delta I_{\mathrm{i}}\,. \tag{5.12}$$

If the same commercial dc-SQUID as used in our inductive detection technique is applied in the Allegro gravitational wave detector, the mutual inductance of the input coil and the feedback coil in the SQUID is negligible. Combining this with the conditions set by (5.9), (5.10) and (5.11), the input flux change $\Delta\Phi_{\mathrm{i}}$ resulting from a displacement of the mushroom resonator Δx is written as

$$\Delta\Phi_{\mathrm{i}} = M_{\mathrm{is}}\,\frac{\frac{L_1}{d}I_0}{M_{23} - \frac{(L_3+L_{\mathrm{i}})(L_1+L_2)}{M_{23}}}\,\Delta x\,. \tag{5.13}$$

With the same SQUID parameters used in section 5.4 and the typical values $I_0 \approx 10\,\mathrm{A}$, $d = 133\,\mu\mathrm{m}$, $L_1 = 51\,\mu\mathrm{H}$, $L_2 = 104\,\mu\mathrm{H}$, $L_3 = 4.6\,\mu\mathrm{H}$, $L_{\mathrm{i}} \approx 2\,\mu\mathrm{H}$, $M_{23} = 21.4\,\mu\mathrm{H}$ [Sol94], a resolution of the displacement Δx can be calculated to be of the order of $10^{-18}\,\mathrm{m}$, which is about 5 orders of magnitude better than the resolution of the inductive measurement discussed above.

It is worth to notice that there is no fundemental difference between the setup for the inductive detection of the motion of the double-paddle oscillator and the readout of gravitational wave detectors. Therefore the resolution of displacements in the double-paddle oscillator measurements can in principle be the same as the one of the gravitational wave detector. The most significant difference between the two setups is the type of inductance which gets modulated by the displacement of the superconducting object to be measured. In the case of the Allegro detector the self inductance of the pickup coil is modulated, whereas in our double-paddle oscillator experiment the mutual inductance between the pickup coil and the field coil gets modulated.

The sensitivity of the experiment discussed in this thesis could be increased by more than 4 orders of magnitude by increasing the current in the field coil, increasing the number of turns of the field coil and decreasing the distance between the two coils and the paddle. However, the incerased sensitivity also might bring about a number of potential problems:

i) The increased magnetic fields might cause significant eddy current losses in metallic parts of the setup as well as an increased heat capacity due to magnetic moments in the rather large external field.

ii) With decreasing distance between the coils and the paddle , the setup becomes more difficult to be arranged properly.

iii) One has to keep in mind that the rate of flux changes to be measured should not exceed the slew rate of the flux-locked-loop electronics. Theoretically this can always be fulfilled by driving the paddle with small forces and running the experiment with small displacement amplitudes. After all this is the motivation for the development of a setup with increased sensitivity which is discussed in this thesis.

However, in a real measurement the paddle might not only oscillate on the driven resonance frequency. Usually vibrations of the building and the pumps, which are needed to run the cryostat, can couple to the double-paddle oscillator and excite different modes.

With decreasing driving amplitudes these erratically excited oscillations start to dominate the detected signal and prevent the experimenter from increasing the resolution of the displacement by simply increasing the slope of the magnetic field $\partial B/\partial x$ at the position of the pickup coil.

As a consequence, the ultimate resolution of the inductive detection setup can only be reached if the whole experiment, including the support of the cryostat and its connection to the pumps is disigned carefully, in order to achieve the best possible mechanical decoupling of the double-paddle oscillator from its surrounding.

5.6   Experimental performance of inductive measurements

5.6.1   Comparison of capacitive and inductive measurements

In order to compare the inductive detection technique with the capacitive detection method, measurements with an a-SiO$_2$ paddle using both readout techniques are presented. In these measurements the field coil and the pickup coil were fixed carefully as described in section 5.3.2. Since the oscilloator eigenmodes show different displacements at the head and the wings, it is reasonable to use the AT2-mode for this comparison. For this mode, the displacements of the head and the wings are almost identical, as was shown in laser-Doppler vibrometry measurements [Liu01].

Figure 5.14 shows the resonance curves of the a-SiO$_2$ paddle measured with the capacitive technique and the inductive method in a magnetic field of 30 Gauss. Both of the results are fitted with Lorentzian $L(f)$, which is shown by the solid curves. The quality of the inductive measurement is much better than that of the capacitive detection. Compared to the fitting curve, the relative mean deviation $\chi_{\mathrm{rel}} = \sqrt{\frac{1}{n}\Sigma[A(f) - L(f)]^2} / L(f_0)$ of the data of the inductive measurement is about one order less than that of the capacitive measurement. $A(f)$ and $L(f)$ are the amplitudes of the data and the fitting curve, respectively. $L(f_0)$ is the maximum amplitude of the fitting curve, which is at the resonance frequency f_0. n is the number of the measured data. The full width at half

maximum shows that the quality factor Q of the internal friction is about 77000 for both measurements.
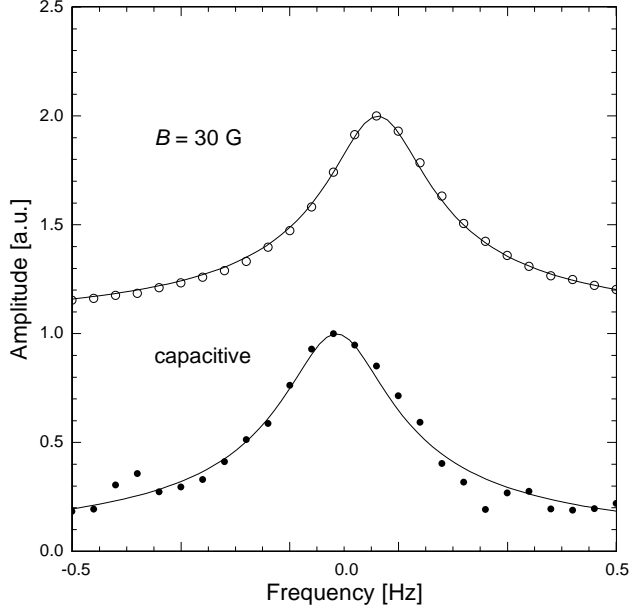
Fig. 5.14: Resonance curves (AT2) of an a-SiO$_2$ paddle measured with capacitive and inductive detection technique at 30 Gauss, respectively. The excitation voltage is 3 V and the temperature is 13.4 mK in both measurements. The resonance frequency is $f_0 \approx 14.14$ kHz.

A difference of the resonance frequency for the SQUID detection and the capacitive detection is visible in the figure, which is about 0.08 Hz. The slight shift in resonance frequency f_0 is caused by switching off the bias voltage $U = 300$ V needed for capacitive detection [Hei02].

The influence of the bias voltage can qualitatively be derived from the following consideration. The resonance frequency of the paddle can be written as the frequency of a harmonic oscillator

$$f_0 = \sqrt{\frac{k}{m}} \; , \tag{5.14}$$

where k is the effective spring constant, m is the effective mass of the oscillator. The detection electrode and the wing of the paddle form a capacitor. If the distance between the detection electrode and the wing of the paddle is x_d, the electric field force by applying a bias voltage U is given by

$$F = -k_\mathrm{mech}\xi + \frac{1}{2}\,C\frac{U^2}{x_\mathrm{d} - \xi} = -k_\mathrm{mech}\xi + \frac{1}{2}\frac{\epsilon_0 A U^2}{(x_\mathrm{d} - \xi)^2} \; . \tag{5.15}$$

Here k_mech is the mechanical spring constant, ξ is the displacement of the paddle's wing from its rest position at zero voltage $U = 0$, C is the capacitance, and A is the effective area of this capacitor.

From (5.15) one derives the effective spring constant as

$$k = -\frac{\mathrm{d}F}{\mathrm{d}\xi} = k_\mathrm{mech} - \frac{\epsilon_0 A U^2}{(x_\mathrm{d} - \xi)^3}. \tag{5.16}$$

Taking into account that the vibrational displacement of the wing of paddle ξ is of the order of nm and the distance between the detection electrode and the wing of the paddle is around 100 μm ($\xi \ll x_\mathrm{d}$), the formula can be simplified to

$$k \approx k_\mathrm{mech} - \frac{\epsilon_0 A U^2}{x_\mathrm{d}^3} \; . \tag{5.17}$$

Thus the bias voltage U causes a reduction of the effective spring constant and therefore a reduction of the resonance frequency.

To get a better understanding of the qualitative difference of the readout techniques, the different signals were monitored by a spectrum analyzer. Figure 5.15 shows the frequency spectrum from 13.8 kHz to 14.5 kHz around the AT2 mode of the a-SiO$_2$ paddle measured with the capacitive detection technique. The excitation voltage is 4 V and the temperature of the mixing chamber is 13.4 mK. The experiment was carried out under the same conditions as the measurement of the resonance curve displayed in figure 5.14, except for the slightly different driving voltage. This spectrum shows many peaks which are equidistant. From their frequencies we see that they are high harmonics of 50 Hz, which are probably coupled to the detection electrode by the bias voltage cable and power supply. Among them the one peak marked by an arrow corresponds to the driven AT2 mode of the paddle. As the frequency of these noise peaks can be very close to the resonance frequency of the double-paddle oscillator, their influence can degrade the quelity of the data significantly.
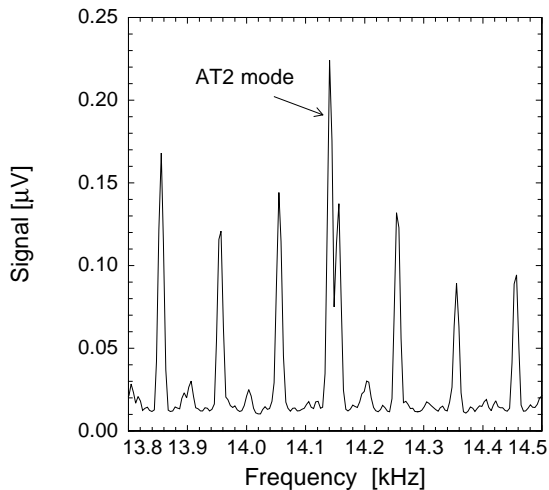
Fig. 5.15: Frequency spectrum of the capacitive detection signal in a narrow frequency range around the AT2 mode of an a-SiO$_2$ paddle. The excitation voltage is 4 V and the temperature is 13.4 mK. The peak marked by an arrow corresponds to the driven AT2 mode of the paddle.
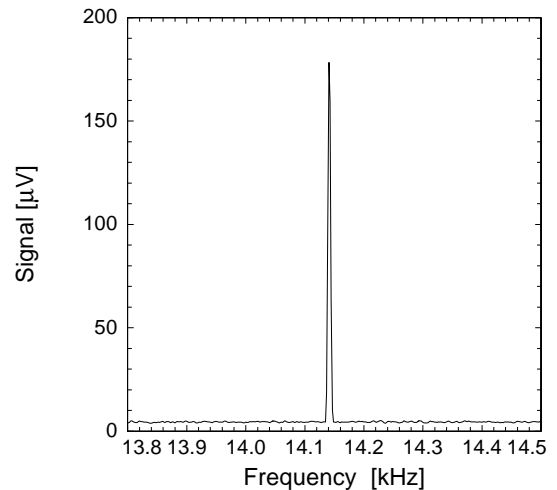
Fig. 5.16: Frequency spectrum of the inductive detection signal in a narrow frequency range around the AT2 mode of an a-SiO$_2$ paddle. In this measurement the magnetic field was 30 Gauss and the paddle was driven on resonance with an excitation voltage of 4 V. The temperature is 13.4 mK.

Figure 5.16 shows the frequency spectrum in the same frequency range as the one in figure 5.15 around AT2 mode of the a-SiO$_2$ paddle measured with the inductive detection technique in a magnetic field of 30 Gauss. The excitation voltage and the temperature is the same as used in the capacitive measurement shown in figure 5.15. The experiment was carried out under the same conditions as the measurement of the resonance curve displayed in figure 5.14, except for the slightly different driving voltage. In this figure only one peak – the resonance signal – is clearly visible. The noise level of the background is almost equal to the relevant voltage value of the white noise of the dc-SQUID. No significant noise peaks are found in the relevant frequency range around the resonance, which could degrade the signal-to-noise ratio of the measurement.

5.6.2   Magnetic field dependence of the resonance curve

In order to exclude the possible doubt that the applied magnetic field of a few Gauss has an influence on the measured internal friction Q^{-1} and the resonance frequency f_0 of the mechanical oscillator, we recorded resonance curves in different magnetic fields B with the inductive detection technique. All the other parameters of the setup remain unchanged.

Figure 5.17 shows two resonance curves of the AT2 mode measured at a temperature of 50 mK using the same excitation voltage but different magnetic fields ($B = 9$ G and $B = 18$ G). Qualitatively, one can see that the signal size increases with increasing magnetic field. The relative mean deviation $\chi_{\rm rel}$ decreases by about a factor of 2 when the applied magnetic field is increased to twice its value from 9 Gauss to 18 Gauss.
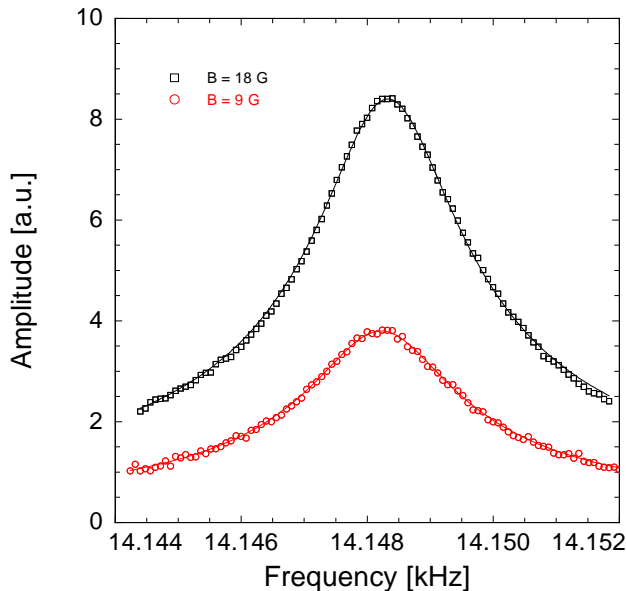

Fig. 5.17: Resonance curves of AT2 mode of an a-SiO$_2$ paddle at 50 mK measured with the same excitation voltage in different magnetic fields $B = 9$ G and $B = 18$ G.

In a quantitative analysis of the measured internal friction one finds the two values $Q^{-1} = 1.59 \times 10^{-4}$ ($B = 9$ G) and $Q^{-1} = 1.56 \times 10^{-4}$ ($B = 18$ G) for the measurements in the two different magnetic fields. The difference between these two values is relatively small and comparable to the uncertainty of the analysis. Moreover, the measured damping

seems to become smaller by 2 percent when the magnetic field is increased by a factor of 2. Thus we conclude that the contribution of eddy current damping due to the magnetic field is negligible at the present level of sensitivity.

In a quantitative analysis of the measured resonance frequency one finds $f_0 = 14148.22$ Hz ($B = 9$ G) and $f_0 = 14148.33$ Hz ($B = 18$ G) for the measurements in the two different magnetic fields. The relative small difference of $\Delta f = 0.11$ Hz is comparable to the uncertainty of our measurement and analysis. However, the resonance frequency seems to increase with increasing magnetic field. The changing direction is expected, since the effective spring constant of the oscillator increases with increasing the magnetic field.

Figure 5.18 shows the inductively detected amplitude at the resonance frequency (AT2) as function of the applied magnetic field. The excitation voltage in this measurement is 30 V and the temperature is 50 mK. The amplitude depends linearly on the magnetic field. The offset of the detected amplitude in zero applied field $B = 0$ G is due to the earth magnetic field frozen in the field coil during the cooling down process.
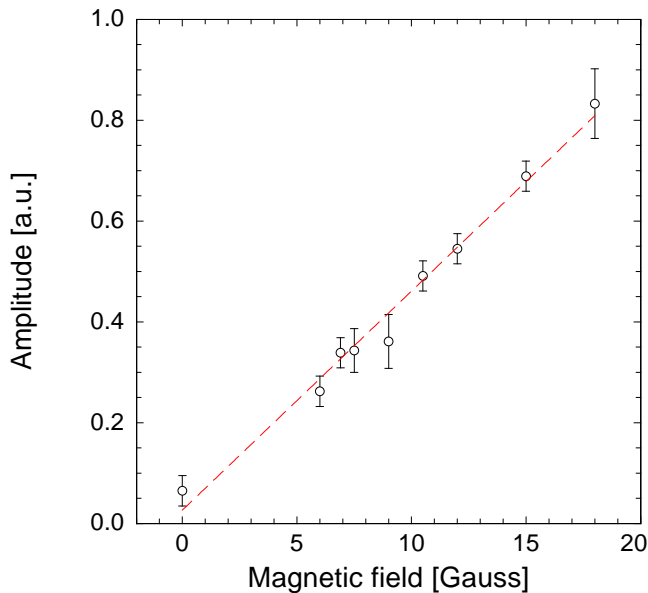

Fig. 5.18: Linear magnetic field dependence of the oscillation amplitude of AT1 mode. The excitation voltage is 30 V and the temperature is 100 mK.

5.6.3   Nonlinear effect measured with inductive technique

Figure 5.19 shows the resonance curves of the AT1 mode for an a-SiO$_2$ paddle driven with six different excitation voltages. The temperature is at 13.4 mK and the magnetic field is about 18 Gauss. The position of the resonance frequency decreases with increasing excitation voltage. The two curves for an excitation voltage of 8 V show a hysteretic effect, i.e. the shape of the resonance curve depends on the direction of the frequency sweep. This result is in good agreement with the results that were already observed in capacitive measurements [Cla01].

Figure 5.20 shows the resonance frequency as function of the excitation voltage of an a-SiO$_2$ paddle for the AT1 mode at 13.4 mK. The measurements with the SQUID detection
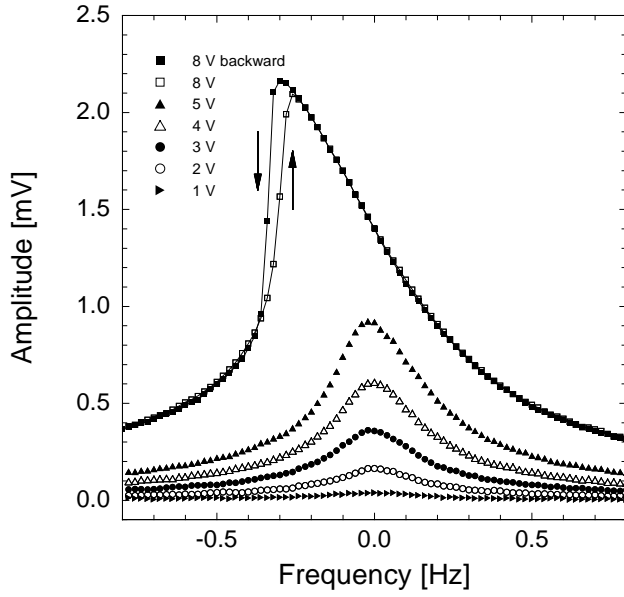
Fig. 5.19: Resonance curve of AT1 mode for an a-SiO$_2$ paddle driven at different excitation voltages. The temperature is at 13.4 mK and the magnetic field is about 18 Gauss. For a voltage of 8 V two curves are plotted on top of each other. The curves show a significant dependence on the direction of the frequency sweep.

technique are carried out in a magnetic field of 18 G. The resonance frequency f_{res} decreases with increasing excitation voltage, i.e. increasing strain field. The other modes for the a-SiO$_2$ paddle and the BK7 paddle show the same behaviour at low temperatures.

The origin of this behaviour is due to the nonlinear effects and therefore causes a shift of the resonance frequency of the oscillator. As presented in section 3.3, compared to the resonance frequency in the linear regime the resonance frequency at 5.8 V is shifted, as if the paddle were at a lower temperature, the temperature difference being about 0.4 mK. This leads to the conclusion that the excitation voltage must be selected sufficiently small, in order to accomplish measurements in the linear regime. However, in the capacitive
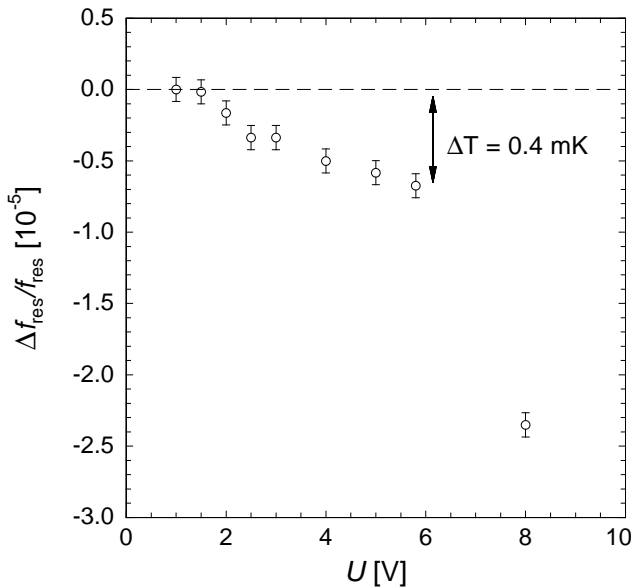
Fig. 5.20: Resonance frequency of the AT1 mode of an a-SiO$_2$ paddle as function of the excitation voltage. The measurement is carried out with the SQUID detection technique in a magnetic field of 18 G at a temperature of 13.4 mK.

measurement the excitation voltage cannot be reduced further at very low temperatures due to the limited sensitivity of the capacitive detection technique. As shown in section 5.4, in our novel inductive measurement the resolution is large enough to allow for suffiently small excitation voltage in order to avoid the influence of nonlinear effects in all the measurements presented in chapter 6.

5.6.4   Further advantages of the new setup and outlook

A big advantage of the new method is that the assembly is not as difficult as that for the capacitive detection. With the capacitive technique one must be very careful to adjust the distance between the electrodes and the paddle. The gap is typically about 100 μm, in order to be able to detect the resonances with a measurable signal. In the new setup the detection coil for the SQUID readout is mechanically fixed to the Vespel part. The distance from the pickup coil to the head of paddle is chosen and fixed to be about 1 mm. We do not need to consider the distance between the pickup coil and the paddle every time.

Another advantage is that we can detect the torsional modes with our design, especially the AT1 mode, which is hard to be detected by the capacitive detection used for the double-paddle oscillator. The AT1 mode is the most important mode for the study of the elastic properties of double-paddle oscillator, since the strain field on the paddle is far from its clamping part. Therefore one can measure the intrinsic properties of the glass with very high accuracy.

The present status of the experimental setup allows for measurements of the acoustic properties of double-paddle oscillators with a resolution which is 10 to 100 times better compared to the one in capacitive measurements. The amplitudes of the oscillation can be kept small enough to stay in the linear regime even at temperatures of a few milli-Kelvin. A further improvement of the sensitivity, which would allow for measurements at even lower temperatures, can be achieved without significant changes of the setup by increasing the bias magnetic field. However, care must be taken to avoid parasitic mechanical resonances of the detection circuit and to prevent external vibrations from coupling to the double-paddle oscillator.

6. Results and discussion

In this chapter the experimental results on acoustic measurements of a-SiO$_2$ and BK7 based on the novel inductive detection technique for double-paddle oscillators are presented. At first the re-calibration of the lowest part of the temperature scale due to the experimental findings from the novel noise thermometer in section 5.1 is exemplified for a data set of a-SiO$_2$. The studies on a-SiO$_2$ and BK7 are subsequently presented as function of the re-calibrated temperature scale. A summarizing discussion of the experimental findings is given in the last section including a comparison to measurements with the conventional capacitive detection technique and to the predictions of the standard tunneling model. The experimental findings suggest strongly an enhancement of this theoretical approach.

6.1 Temperature re-calibration by noise thermometer

In section 4.3.2 the temperature information from the carbon thermometer and the noise thermometer were shown. The comparison led to the conclusion that the curve of the carbon thermometer had to be re-calibrated in the low temperature region ($T < 15$ mK).

In figure 6.1 the re-calibration of the temperature scale is exemplified for a data set of a-SiO$_2$. In the left diagram the change of sound velocity and in the right one the internal friction at a frequency of 12 kHz are shown as function of temperature. The measurement is carried out from 5 mK to about 1 K in an outer magnetic field of 30 Gauss. The tri-
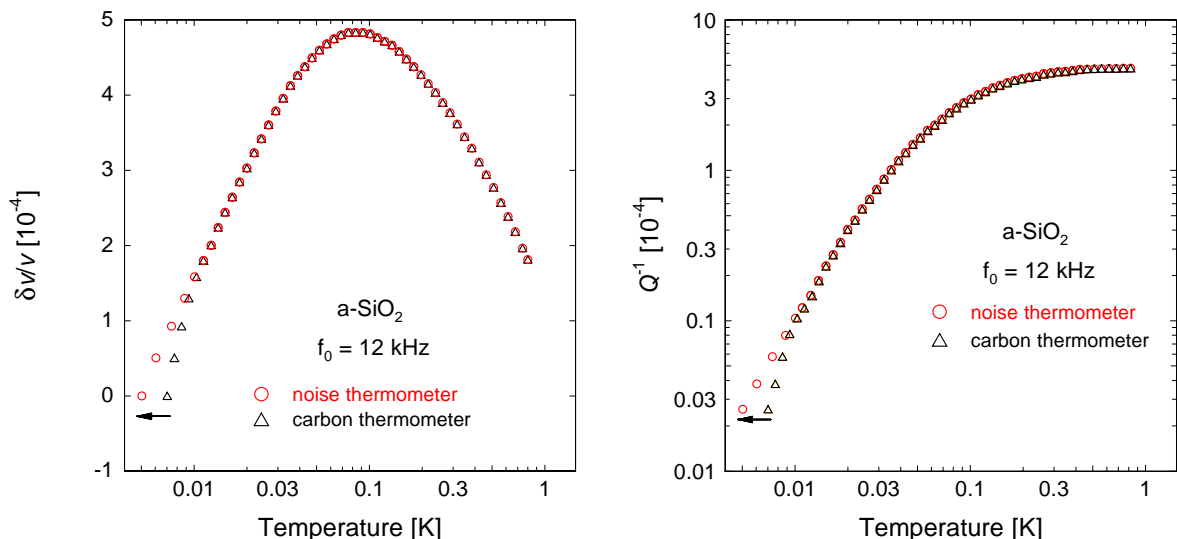
Fig. 6.1: Relative change of sound velocity and internal friction of a-SiO$_2$ at a frequency of 12 kHz as function of temperature. The triangles show the run of the curve for the old calibration curve of the carbon thermometer. The circles represent the re-calibration of the temperature scale based on the noise thermometer.

angles show the run of the curve for the old calibration curve of the carbon thermometer.
The circles represent the re-calibration of the temperature scale based on the measurments
with the noise thermometer. The arrow stands for the direction of the re-calibration. The
maximum temperature shift is about 2 mK at the lowest temperatures. In the follow-
ing sections all the experimental data of the double-paddle oscillator measurements are
presented with the re-calibrated temperature scale below 15 mK .

6.2   Experimental results of the mechanical properties of a-SiO$_2$

In this section the measurements of the relative change of sound velocity and the internal
friction of a-SiO$_2$ are presented and discussed. The inductive detection technique based
on a dc-SQUID was used to measure the temperature dependence of several eigenmodes
of the double-paddle oscillator at 1 kHz (ST), 3.7 kHz (B2), 7.5 kHz (B3), 12 kHz (AT1),
and 14 kHz (AT2) in the temperature range from 5 mK to about 1 K. The outer magnetic
field was about 30 G.

Due to some asymmetry in the setup a different flux couples into the two parts of the
pickup coil, and therefore the motion of the bending modes creates a net flux which can
easily be detected by the SQUID. The anti-symmetric torsional mode AT1 is measured as
function of temperature for the first time and shows similar temperature dependence with
the former experimental data based on the capacitive detection technique. In all of the
measurements careful attention was paid to detect the relative change of sound velocity
$\delta v/v$ and the internal friction Q^{-1} in the linear regime, i.e. at sufficiently small excitation
voltages (see section 3.3).
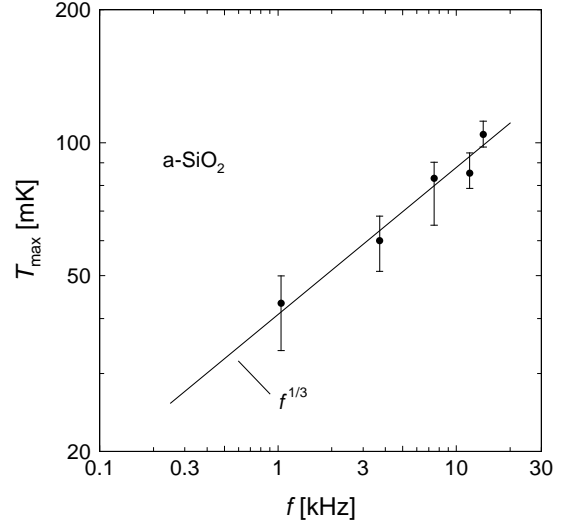
6.2.1   Relative change of sound velocity

Figure 6.2 shows the temperature dependence of sound velocity $\delta v/v$ below 1 K at five
different frequencies. For better clearness the different data sets are shifted to each other.

At low temperatures the sound velocity for all modes increases, passes a maximum and
decreases at higher temperatures. The increase of sound velocity below the maximum has
almost the same slope as the decrease above the maximum on the logarithmic temperature
scale. This behaviour is in marked contrast to the standard tunneling model where a slope
ratio of $2 : -1$ is predicted from (2.34) and (2.36) discussed in section 2.2.3. In addition one
can deduce from this figure that the slope of sound velocity at the low-temperature varies
slightly with the frequency. This behaviour seems to indicate that there is an additional
interaction process at low temperatures, which is not predicted by the standard tunneling
model.

Figure 6.3 shows for the data sets from figure 6.2 the temperatures $T_{\max}$ that correspond
to the maximum of sound velocity as function of frequency in a double-logarithmic plot.
The error bars result from the uncertainty in deducing the values for $T_{\max}$. The solid
line has a slope of $1/3$ and is therefore in accordance with the prediction of the standard
tunneling model $T_{\max} \propto f^{1/3}$ as shown in (2.35).
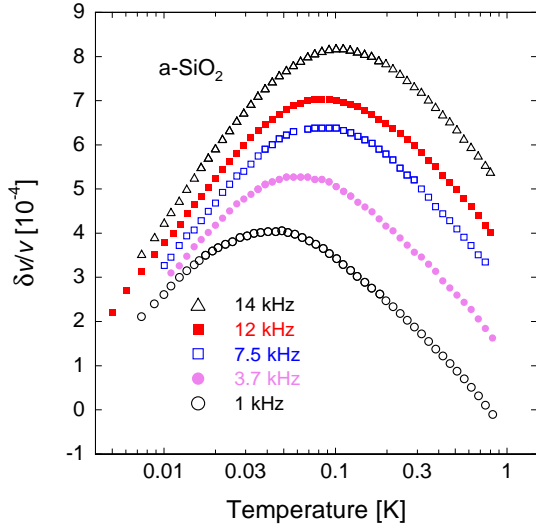
Fig. 6.2: Relative change of sound velocity of a-SiO$_2$ as function of temperature. The paddle was driven at five different frequencies indicated by the different symbols. The readout was carried out with the SQUID detection technique in an outer magnetic field of 30 Gauss.

Fig. 6.3: Temperature of the maximum in sound velocity as function of frequency for the a-SiO$_2$ paddle. The maximum temperatures scale as $T_{\max} \propto f^{1/3}$ (indicated by the solid line) and therefore follow the prediction of the standard tunneling model.

6.2.2 Internal friction

Figure 6.4 shows the temperature dependence of the internal friction Q^{-1} below 1 K at the five different frequencies on a double-logarithmic scale. The measurements were carried out simultaneously with the measurement of the relative change of sound velocity presented in figure 6.2.

While in the experiment only the *relative* change of sound velocity can be measured, it is possible to determine the absolute values of the internal friction. The temperature dependence of δQ^{-1} is deduced in two steps. The relative change δQ^{-1} is determined as function of temperture by measuring the change in amplitude at constant excitation voltage or by changing the excitation voltage at constant oscillatory amplitude. Hereby it is necessary to adjust the excitation voltage in such a way that the measurement is carried out in the linear regime. The absolute values of the internal friction at constant temperatures are deduced from resonance curves as shown in section 4.4. In the figure the relative changes δQ^{-1} are shifted to the absolute values deduced from the resonance curves.

The shape of the internal friction curves can be described qualitatively as follows: At low temperatures the internal friction rises and approaches a temperature and frequency independent plateau. At the lowest frequency the plateau is reached at about 100 mK, while the highest mode merges into this level at about 300 mK. Below the plateau, the internal friction Q^{-1} shows a strong frequency dependence. In agreement with the pre-
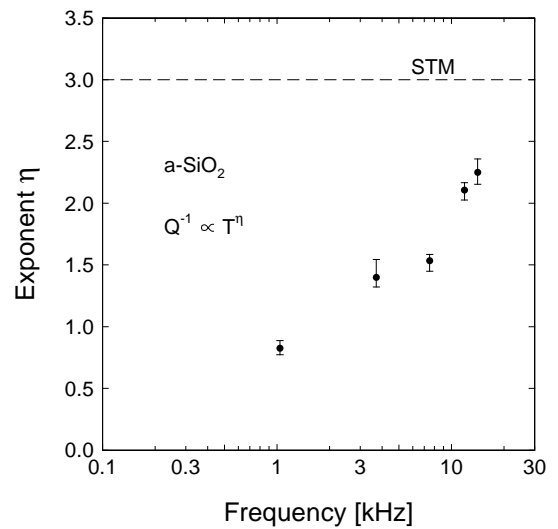
dictions of the standard tunneling model, $Q^{-1} \propto CT^3/\omega$, the internal friction rises with invreasing frequency.

However, there are qualitative and quantitative deviations of the experimental results from the prediction of the standard tunneling model. In the temperature range 5 – 30 mK, the internal friction of all modes varies in good approximation as $Q^{-1} \propto T^\eta$, with the exponent η being clearly smaller than three as the predicted by (2.29). Figure 6.5 shows the exponent η derived from the temperature dependence of Q^{-1} at low temperatures. The exponent rises monotonically with increasing frequency.

Furthermore the internal friction depicted in figure 6.4 should lie in between the two solid lines for 1 kHz and 14 kHz, which are simulated by Classen and represent the prediction of the standard tunneling model for a-SiO$_2$. The deviations from the model become more pronounced towards lower temperatures.
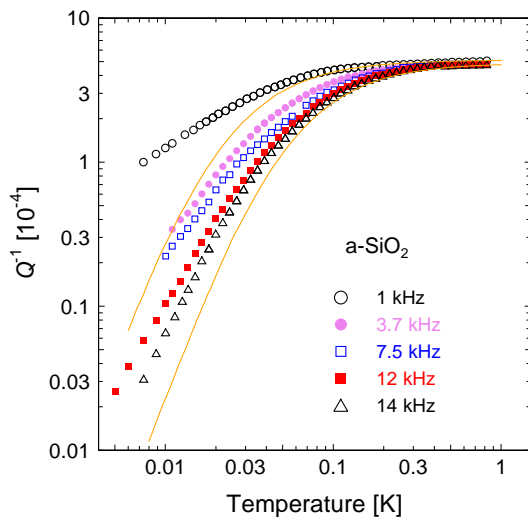
Fig. 6.4: Internal friction of a-SiO$_2$ as function of temperature on a double-logarithmic scale. The paddle was excited at five frequencies. The measurements are carried out with the SQUID detection technique in an outer magnetic field of 30 G. The solid lines represent simulated data according to the standard tunneling model for 1 kHz and 14.0 kHz simulated by Classen [Cla00], respectively.

Fig. 6.5: Exponent η as function of frequency, derived from the variation of the internal friction at low temperatures. The dashed line indicates the value of η predicted by the standard tunneling model.

6.3   Experimental results of the mechanical properties of BK7

In this section the relative change of sound velocity and the internal friction of BK7 are presented and discussed. The measurements were performed at 1 kHz (ST), 3.5 kHz (B2), 7.3 kHz (B3), 11.3 kHz (AT1) and 14.2 kHz (AT2) in the temperature range from 7 mK to about 1 K in an external magnetic field of 30 G. As in the case of a-SiO$_2$, the readout was carried out with the inductive detection technique. All the measurements were done with the same BK7 paddle at sufficiently small excitation voltages in order to avoid nonlinear effects.

### 6.3.1   Relative change of sound velocity

In figure 6.6 the relative change of sound velocity is shown on a logarithmic temperature scale in the range between 7 mK and about 1 K for five frequencies of measurement.
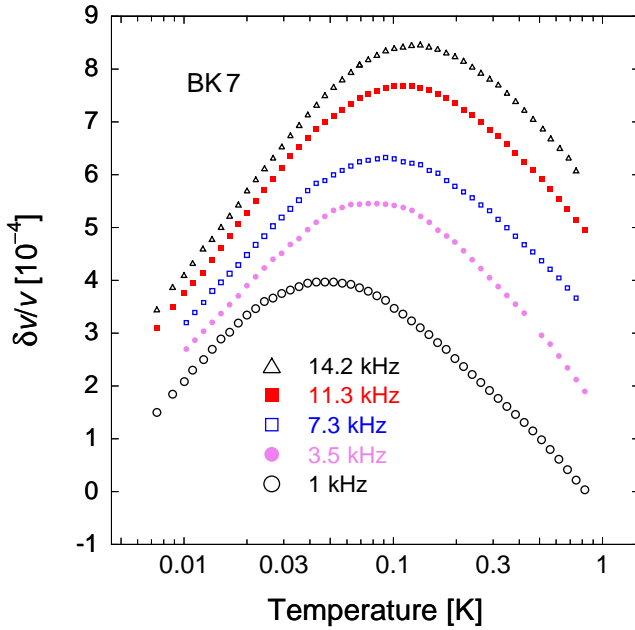
Fig. 6.6: Temperature dependence of sound velocity of BK7. The paddle was excited at five frequencies. The readout was carried out with the SQUID detection technique in a magnetic field of 30 G.

From low temperatures the sound velocity increases, goes through a maximum and decreases with increasing temperature. The ratio of the slopes of sound velocity on both sides of the maximum is approximately $1 : -1$, again in marked difference to the prediction of the standard tunneling model. A comparison with the behaviour of a-SiO$_2$ in figure 6.2 shows that the curves are qualitatively similar.

In figure 6.7 the temperatures $T_{\max}$ of the maximum in the sound velocity of BK 7 are shown as function of frequency. The prediction of the standard tunneling model $T_{\max} \propto f^{1/3}$ is indicated by the solid line. As in the case of a-SiO$_2$ the experimental data and the theoretical finding are in remarkably good agreement in the observed frequency range.
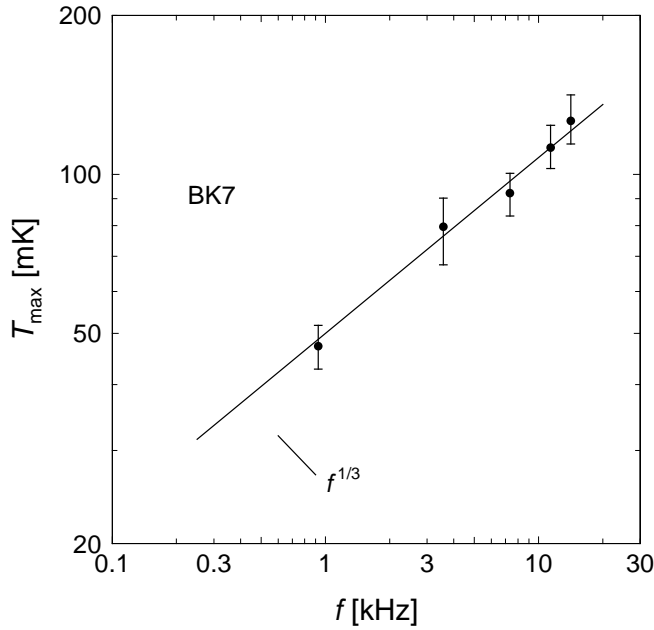
Fig. 6.7: Temperature T_{max} at the position of the maximum of sound velocity as function of frequency for BK7. The maximum temperatures scale as $T_{max} \propto f^{1/3}$ and therefore follow the prediction of the standard tunneling model.
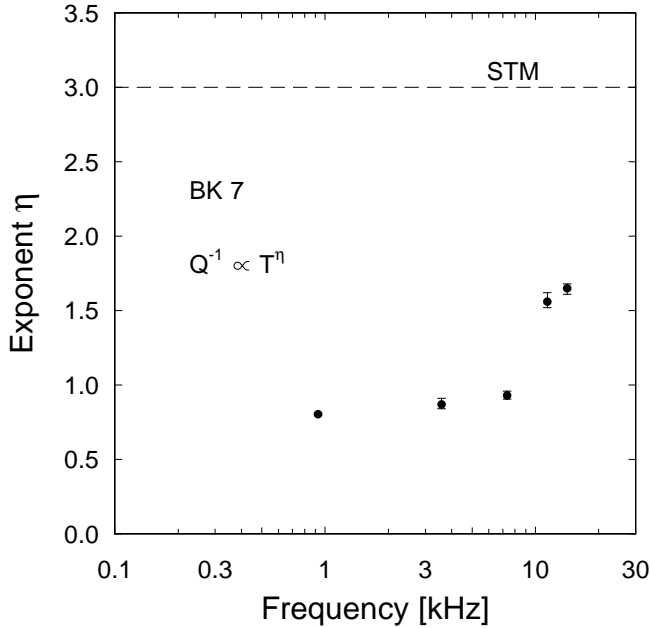
6.3.2   Internal friction

Figure 6.8 shows the temperature dependence of the internal friction Q^{-1} below 1 K on a double-logarithmic scale. The internal friction behaves qualitatively as in the case of a-SiO$_2$ shown in section 6.2.2.

As in the case of a-SiO$_2$, in the temperature range 7 – 30 mK, the internal friction is proportional to T^η. The exponents η derived from the low temperature variation of the internal fricion data are shown in figure 6.9. The values of η increase monotonically
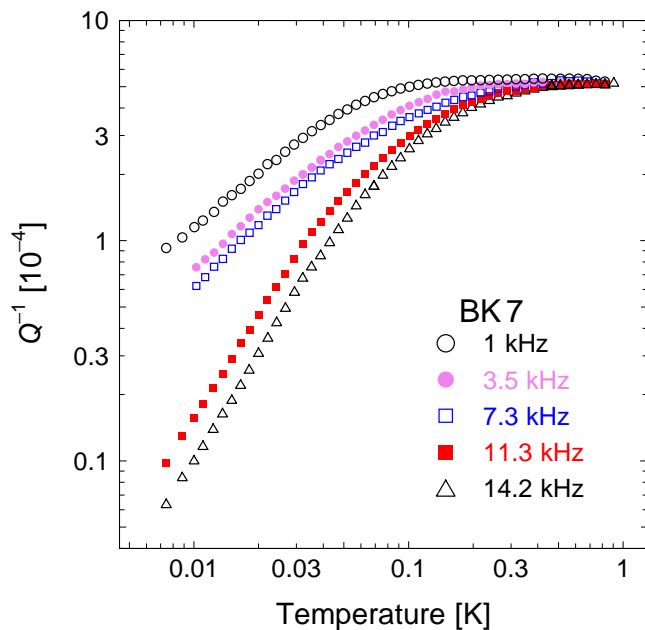
Fig. 6.8: Temperature dependence of internal friction of BK7 paddle at five frequencies, measured with the SQUID detection technique in an outer magnetic field of 30 G.

Fig. 6.9: Exponent η as function of frequency, derived from the variation of the internal friction at low temperatures. The dashed line indicates the value of η predicted by the standard tunneling model.

with frequency, but are always smaller than 3. Additionally with decreasing frequency the values of the exponent η tend to saturate to about 1. A comparison with the data of a-SiO$_2$ shows yet that in the case of BK7 the values of η are considerably smaller.

6.4 Discussion

In this section the results are compared with previous capacitive measurements and discussed within the framework of the standard tunneling model.

### 6.4.1 Comparison with previous capacitive measurements

Experimental results on a-SiO$_2$

Several years ago the low frequency elastic properties of a-SiO$_2$ were measured with the conventional capacitive readout technique [Cla00]. The experimental findings were already presented in section 2.3. In figure 2.7 the relative change of sound velocity $\delta v/v$ and the internal friction Q^{-1} as function of temperature were shown for several frequencies. The temperature dependence of sound velocity and internal friction measured with our inductive technique are in good agreement with those data.

As an example we compare the internal friction of the capacitive and inductive readout technique at low temperatures. The damping of the double-paddle oscillator varies in good approximation as $Q^{-1} \propto T^\eta$ with an exponent η that depends monotonously on the frequency.

In figure 6.10 the exponents are plotted which were derived from the previous experiments and together with the data presented here. Clearly, the exponents deduced for the

measurements are in good agreement. The values of exponent η seem also to saturate to about 1 with decreasing frequency, which is similar as shown in figure 6.9.
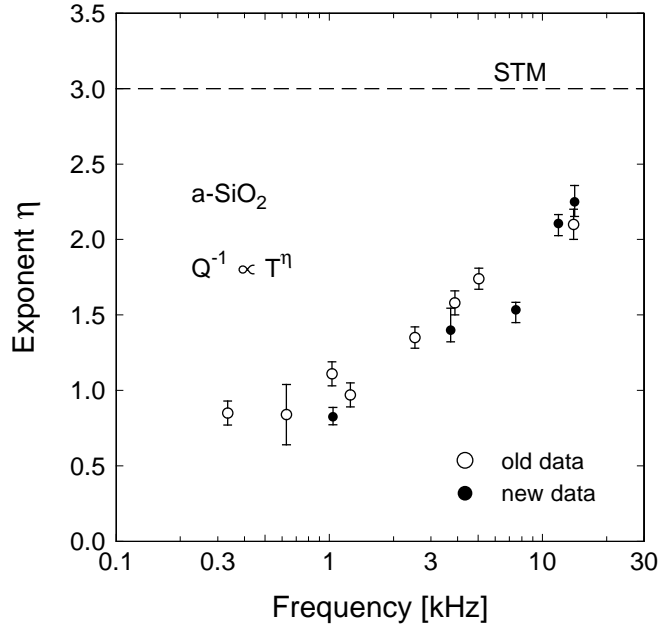
Fig. 6.10: Exponent η as function of frequency, derived from measurements using the capacitive and the inductive techniques. The dashed line represents the prediction by the standard tunneling model.

At this point we want to emphasize that we have also investigated the behaviour of the AT1 modes at about 12 kHz for a-SiO$_2$ and 11.3 kHz for BK7. This mode is hardly detectable by the capacitive detection technique due to the tiny displacement of the paddle wings. The great advantage in the use of the AT1 mode is that the main strain occurs at the neck of the double-paddle oscillator. Compared to the other modes the strain field at the leg of is small and consequently oscillationary energy will hardly be dissipated into the paddle holder at the clamping. Therefore the background loss of this mode should be much smaller than for the other eigenmodes.

As can be seen in figure 6.2 and figure 6.4, the relative change of sound velocity as well as the internal friction of this mode do hardly differ from other modes and fit well in the other data sets. Due to its strong decoupling from the clamping part of the paddle holder, the AT1 mode is predestinated for measurements of the elastic properties of glasses in the linear regime at even lower temperatures.

Experimental results for BK7

The elastic properties of BK7 below 1 K were measured by Layer *et al.* [Lay00] with a double-paddle oscillator and comventional capacitive readout technique at two different frequencies: 1 kHz (ST) and 15.4 kHz (AT2). Therefore two of our data sets for BK7 derived in our inductive measurement can be compared to the former measurements. In addition, three new modes, B2, B3 and AT1, were measured for the first time.

The comparision of the symmetric torsional modes for two different BK7 paddles does not show any significant difference in the temperature dependence of sound velocity and

internal friction. However, the behaviours of the AT2 modes of the two paddles show significant differences between the measurements with the two techniques.

The left hand side of figure 6.11 shows the temperature dependence of sound velocity of the AT2 mode for two different BK7 paddles below 100 mK. The measurements are carried out independently with the inductive detection technique and with the conventional capacitive detection method [Lay00], respectively. Due to the slightly different paddle geometry, the eigenfrequencies of the AT2 modes differ from each other by about 1 kHz. The sound velocity in our measurement shows a linear temperature dependence on the logarithmic temperature scale below 30 mK as indicated by the dashed line. In the previous measurements a slight bending was observed at the lowest temperatures made visible by the dashed line. The beginning of the deviations at about 15 mK is marked by an arrow.

The right hand side of figure 6.11 shows the temperature dependence of the corresponding internal friction for the same BK7 paddles below 100 mK. In the temperature range from 20 – 100 mK the curves of both eigenfrequencies show a behaviour that corresponds qualitatively to the prediction of the standard tunneling model. In this temperature range the relationship $Q^{-1} \propto 1/\omega$ is expected to hold. This behaviour is clearly visible at the intermediate temperatures. However, the data taken at 15.4 kHz with the capacitive technique deviate from the expected power-law variation. In contrast, in our measurements the temperature dependence of Q^{-1} follows a power-law resulting in a crossover of the two curves.

Both measured quantities, $\delta v/v$ and Q^{-1} show significant differences in their temperature dependence. Due to the analogous temperature behaviour of sound velocity and
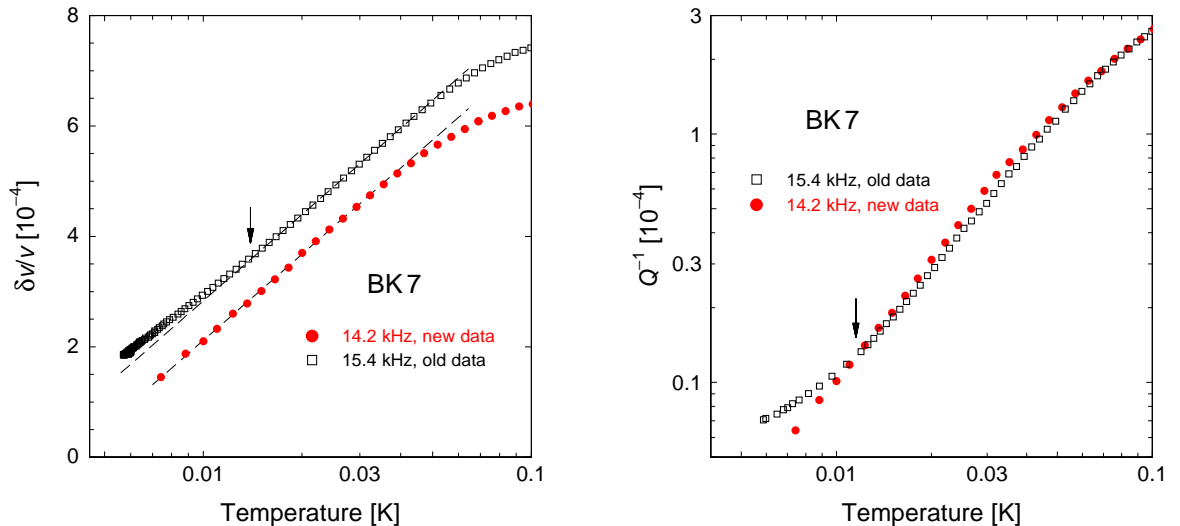
Fig. 6.11: Temperature dependence of sound velocity and internal friction of BK7. Both plots contain two data sets. One set (black) was measured capacitively [Lay00], the other set (red) with the new SQUID detection technique. Due to the different sizes of the paddles, the eigenfrequencies for the AT2 modes are different. The dashed lines in the left figure are only guides to the eye.

internal friction, several possibilities for the bending of the curves were already discussed previously. The first possibility is that the imperfect geometry of the double-paddle might facilitate the mixing of different vibrational modes. In the work of [Lay00] the paddle was manufactured by ultrasonic drilling, resulting in coarse edges and borders. In our measurements the paddle were manufactured by laser cutting, resulting in a well definded geometry. Thus the observed bending could be due to background loss. Another possibility is that additional relaxation processes give rise to additional losses, e.g. the mutual interaction between tunneling states could be such a mechanism causing a weaker temperature dependence than the one-phonon process [Bur95, Ens97]. A further possibility is that in the previous measurements a thermal gradient was presented. The former experiments were carried out inside a field coil, consisting of a 1 km long superconducting NbTi wire, fixed to a stainless steel holder. At lowest temperatures this arrangement could have acted as a heat bath for the paddle holder and therefore could have caused a thermal gradient between the sample and the mixing chamber.

6.4.2 Comparison with the predictions of standard tunneling model

The results of our measurments indicate claerly that the temperature dependence of the elastic properties of a-SiO$_2$ and BK7 is almost the same. Qualitatively the sound velocity increases at low temperatures, passes a maximum and decreases at higher temperatures, which is also predicted by the standard tunneling model. However, quantitatively the ratio of the slopes on both sides of the maximum is about $1 : -1$ on a logarithmic temperature scale, whereas the prediction from the standard tunneling model is $2 : -1$. On the other hand the experimental data in figure 6.3 and figure 6.7 on the temperature of the maximum in the sound velocity agree remarkably well with the prediction of the standard tunneling model, $T_{\max} \propto f^{1/3}$.

The behaviours of the internal friction of a-SiO$_2$ and BK7 shown in figure 6.4 and figure 6.8 exhibit a clear qualitative deviation from the predictions of the standard tunneling model. From 5 mK to 30 mK the rise of the internal friction for all modes does not exhibit the predicted cubic proportionality to temperature. The temperature dependence can rather be approximated by a power law $Q^{-1} \propto T^{\eta}$ in both cases, where the exponent η increases with frequency, as indicated in figure 6.5 and figure 6.9. However, it is always significantly smaller than 3.

6.4.3 Beyond the standard tunneling model

The nature of the discrepancies between the experimental observations and the prediction of the standard tunneling model is still an interesting but open question that is controversially discussed. However, it seems clear that an important contribution is not included within the assumptions of the standard tunneling model. This contribution becomes more pronounced for the behaviour of glasses below 100 mK. An obvious assumption is that the interaction *between* the tunneling systems should become increasingly important with decreasing temperature and hence the interaction is expected to be a relevant ingredient

for models beyond the standard tunneling model.

The effect of interaction between tunneling systems have been discussed by Burin *et al.*, considering the influence onto their density of states [Bur95, Yu88]. In this approach strain mediated pair excitations of two-level systems play an important role. The interaction between pairs with similar tunneling splitting leads to an additional relaxation contribution with a relaxation rate given by (2.37). As a consequence, a linear temperature dependence of the internal friction is expected at very low temperatures. However the amplitude of the relaxation rate τ_{p}^{-1} is not in agreement with the experimental observations, since this equation should only give a negligibly small contribution in the temperature range of our experiments. In fact the cross-over from the one-phonon dominated relaxation to the linear temperature dependence of a relaxation by pairs of two-level systems is expected to occur at a temperature of 0.6 mK [Bur95, Cla00]. For a reasonable desription of the experimental data the numerical prefactor of (2.37) would have to be increased about 4 orders of magnitude. With this magnitude, that the values of exponent η shown in figure 6.9 and figure 6.10 saturate to about 1 at low frequencies agrees with a linear temperature dependence of Q^{-1} at low temperatures.

A different approach to take into account the interaction between tunneling states was given by Enss and Hunklinger [Ens97], based on a theory by Wuerger for the tunneling of substitutional defects in alkali halides [Wue94, Wue95, Wue97]. In this model the interaction leads to an incoherence of the tunneling motion at very low temperatures. As a result, additional relaxation effects occur and modify the temperature dependencies of $\delta v/v$ and Q^{-1}. Moreover, the resonant contribution to $\delta v/v$ is expected to be significantly reduced [Ens97]. While the basic idea of this model appears to be quite promising a fully developed theory for incoherent tunneling in glasses at very low temperatures has not been worked out yet.

Recently a microscopic glass model was suggested [Kue03]. The approach uses heuristics taken from spin-glass theories with a translationally invariant approach. With this model the asymptotics of the temperature dependence of the internal friction is deduced as

$$Q^{-1} \propto \frac{\pi}{2} C \left(\frac{\hbar\omega}{k_{\mathrm{B}}T} \right)^{\frac{\varepsilon}{2}} \tag{6.1}$$

for the plateau region and

$$Q^{-1} \propto T^{3+\varepsilon} \tag{6.2}$$

for low temperatures. Hereby ε is related to the microscopic interaction strength and has a small positive value. In fact the experimentally observed height of the plateau exhibits a slight frequency dependence in agreement with (6.1) [Bur99]. (6.2) predicts an asymptotic low-temperature variation of Q^{-1} with an exponent slightly large than 3. This is not necessarily a contradiction since the crossover region from plateau to low-temperature asymptotics is so large that effective exponents in accessible temperature ranges can be still smaller than 3, this effect being stronger for lower frequencies. A comparison of theoretical and experimental findings shows that the experimentally observed effective

exponents tend to be somewhat stronger frequency dependent and to be smaller than the values within this model.

Although a truly satisfactory explanation of the low temperature results is still lacking, the suggestions have in common that the mutual interaction of two-level systems appears to play a decisive role on the dynamics and the density of states of the tunneling states. Therefore interactions among the tunneling systems have to be taken into account in future phenomenological or microscopic models.

7. Conclusion and outlook

In this work, low frequency measurements on the elastic properties of amorphous solids (a-SiO$_2$ and BK7) were carried out in the temperature range below 1 K using mechanical oscillators. At low temperatures the elastic properties are dominated by low-energy excitations, so-called tunneling systems. To ensure that the acoustic response of these systems is in the linear regime, the oscillator has to be driven with sufficiently small excitation voltages. To this end an experimental setup has been developed which facilitates a highly sensitive detection of the low-frequency elastic properties of glasses in the temperature range down to 5 mK. In our technique the motion of the double-paddle oscillator is inductively detected by a commercial dc-SQUID.

The double-paddle oscillator can be excited at its eigenmodes, including bending and torsional modes. In particular, the two anti-symmetric torsional modes, called AT1 and AT2, decouple almost entirely from the sample holder and ensure a small background loss. For these modes the strain energy is localized far away from the clamping and only a negligible amount of energy will be dissipated by the sample holder. Therefore, these eigenmodes are predestinated to measure the small intrinsic internal friction, which occurs in amorphous solids at very low temperatures.

The detection of the displacement of the mechanical oscillator is carried out inductively. Therefore the head of the double-paddle oscillator is covered with a thin niobium film which becomes superconducting at low temperatures and acts as a diamagnet. In an external magnetic field the motion of the oscillator leads to a variation in the magnetic field distribution and therefore to a change of the magnetic flux penetrating the gradiometric loop of a pickup coil. This change in magnetic flux is measured with a dc-SQUID. In combination with its electronic setup, the SQUID performs a linear transformation of the magnetic flux change to a voltage signal. The displacement of the oscillator is therefore proportional to the voltage reading of the SQUID electronics.

The excellent performance of the new inductive detection technique based on a commercial dc-SQUID was demonstrated in measurements with double-paddle oscillators made out of different amorphous materials. Within this thesis we showed, that the novel detection method worked well down to several milli-Kelvin. Its sensitivity exceeded the conventional capacitive detection technique by more than one order of magnitude already in these first measurements. The minimum detectable displacement of the oscillator is estimated to be of the order $\Delta x \approx 10^{-13}$ m.

Besides the sensitive readout of the mechanical oscillator, the absolute temperature of the cooling device is of great importance. Therefore we developed a new kind of noise thermometer. The principle of this kind of thermometry is based on the temperature dependence of the Brownian motion of electrons in a metal. The readout of the resulting magnetic Johnson noise is done inductively with another dc-SQUID. In comparison with other noise thermometers, the thermometer developed here has the advantage that it is

sensing the contact-free thus ensuring a thermalization of the sensor material even at lowest temperatures. As a result the temperature scale of the carbon thermometer used so far had to be re-calibrated below $15\,\text{mK}$.

The temperature dependence of the elastic properties for a-SiO$_2$ is in favourable agreement with previous measurements that were performed with a conventional capacitive method. In addition to several bending and torsional modes, the mode AT1 which is characterized by a low background loss was measured for the first time. The temperature dependence of this mode fits well in the data obtained at different frequencies.

The temperature dependence of the elastic properties of BK7 was measured for two bending and three torsional modes of the oscillator. The wide range of frequency completes former measurements on this material [Lay00]. In the previous measurements a clear tendency to saturation in velocity change and internal friction was visible at the lowest temperatures. Our measurements on BK7 show slight deviations from the former experimental findings, but reveal almost the same temperature dependence as for a-SiO$_2$.

Compared to the predictions of the standard tunneling model, deviations for the temperature dependencies of the sound velocity and the internal friction between $5\,\text{mK}$ and $1\,\text{K}$ are confirmed for both glasses. The slopes of the relative change of sound velocity on a logarithmic temperature scale below $1\,\text{K}$ do not scale as $2 : -1$ as predicted by the standard tunneling model, but rather $1 : -1$. For low temperatures the standard tunneling model predicts a cubic temperature dependence for the internal friction. In contrast, the measurements on both glasses can be described by a power-law dependence $Q^{-1} \propto T^{\eta}$ with an exponent η increasing with the measuring frequency, but always remaining smaller than three.

Our studies on a-SiO$_2$ and BK7 clearly show that the elastic properties of amorphous solids at very low temperatures are not sufficiently described by the standard tunneling model. Several suggestions have already been discussed to provide an explanation of the experimental results. Although these theoretical approaches are still controversially discussed, they have in common that the mutual interaction between the tunneling states plays a decisive role.

In the future additional experiments should be carried out. At first the setup can be used to study the elastic behaviour of other types of glass samples. These measurements will help to solve the question whether the observed behaviour is a universal, i.e. the same for all amorphous solids. Interesting candidate are, e.g. barium aluminosilicate glasses (AlBaSi), which are expected to exhibit a strong interactions *between* of the tunneling systems and therefore should show deviations from the expected behaviour at higher temperatures.

Another approach is to extend the available temperature range below $5\,\text{mK}$ within a nuclear demagnetization cryostat. Currently a cooling device of this type is going to be set up in our low-temperature laboratory. Therefore the developed device should be transferred to this cryostat in the near future, in order to carry out experiments down to the microkelvin range. This new cryostat will have a better decoupling from the environment than the ^{3}He-^{4}He dilution refrigerator. Therefore we expect a decrease of low-frequency

disturbancies and hence an enhancement in sensitiviy.

The combination of the highly sensitive inductive detection mechanism and the eigen-modes with low background loss of the double-paddle oscillator leads to the conclusion that the novel setup has ample potential to determine the elastic properties of glasses in the linear regime at even lower temperatures than exploited so far. Due to the increasing importance of the mutual interaction of tunneling states at lower temperatures, the elastic properties of amorphous solids are an exciting subject for theoretical studies as well as for experimental investigations.

Bibliography

[And55] O. L. Anderson, H. E. Bommel, J. Am. Ceram. Soc. **38** (1955) 125.

[And72] P. W. Anderson, B. I. Halperin, C. M. Varma, Philos. Mag. **25** (1972) 1.

[Ber75] B. S. Berry, W. C. Pritchet, IBM J. Res. Develop. **19** (1975) 334.

[Bur94] A. L. Burin, Yu. Kagan, Physica (Amsterdam) **194B-196B** (1994) 393.

[Bur95] A. L. Burin, J. Low Temp. Phys. **100** (1995) 309.

[Bur99] T. Burkert, Diplomarbeit, Universitaet Heidelberg (1999).

[Cla75] J. H. Claassen, J. Appl. Phys. **46** (1975) 2268.

[Cla76] J. Clarke, W. M. Goubau, and M. B. Ketchen, J. Low Temp. Phys. **25** (1976) 99.

[Cla91] J. Classen, Diplomarbeit, Universiteat Heidelberg (1991).

[Cla94] J. Classen, C. Enss, C. Bechinger, G. Weiss, and S. Hunklinger, Ann. Phys. **3** (1994) 315.

[Cla96] J. Clarke, in *SQUID sensors: Fundamentals, Fabrication and Applications*, H. Weinstock (Ed.), Kluwer Academic Publ., Netherlands (1996).

[Cla00] J. Classen, T. Burkert, C. Enss, S. Hunklinger, Phys. Rev. Lett. **84** (2000) 2176.

[Cla01] J. Classen, C. Enss, S. Hunklinger, Phys. Rev. Lett. **86** (2001) 2480.

[Cla04] J. Clarke, A. I. Braginski (ED.) in *The SQUID Handbook*, Wiley-VCH Verlag GmbH & Co. KGaA, Weinheim (2004).

[Cou53] R. Courant, D. Hilbert, *Methods of Mathematical Physics*, Interscience Publ., New York (1953).

[Deb12] P. Debye, Ann. Phys. **39** (1912) 788.

[Dou80] P. Doussineau, C. Frenois, R. G. Leisure, A. Levelut, J. Y. Prieur, J. Phys. (Paris) **41** (1980) 1193.

[Ens89] C. Enss, C. Bechinger, M. v. Schickfus, *Phonons 89*, Ed.: S. Hunklinger, W. Ludwig, G. Weiss, World Scientific, Singapur (1989) 474

[Ens97] C. Enss, S. Hunklinger, Phys. Rev. Lett. **79** (1997) 2831.

[Ens00a] C. Enss, A. Fleischmann, K. Horst, J. Schönefeld, J. Sollner, J. S. Adams, Y. H. Huang, H. Y. Kim, G. M. Seidel, J. Low Temp. Phys. **121**, (2000) 137.

[Ens00b] C. Enss, S. Hunklinger, *Tieftemperaturphysik*, Springer Verlag, Heidelberg (2000).

[Esq92] P. Esquinazi, R. Koenig, F. Pobell, Z. Phys. B **87** (1992) 305.

[Esq98] P. Esquinazi, *Tunneling Systems in Amorphous and Crystalline Solids*, Springer Verlag, Heidelberg (1998).

[Fle98] A. Fleischmann, Diplomarbeit, Universitaet Heidelberg (1998).

[Fle03] A. Fleischmann, Dissertation , Universitaet Heidelberg (2003).

[Har68] J. T. Harding, J. E. Zimmerman, Phys. Lett. A **27** (1968) 670.

[Hei02] M. Heitz, Dissertation, Universitaet Heidelberg (2002).

[Her94] Heraeus Quarzglas GmbH, *Quarzglas fuer Optik, Daten und Eigenschaften*, Hanau (1994).

[Hes96] J. Hessinger, B. E. White Jr., R. O. Pohl, Planet. Space Sci. **44** (1996) 937.

[Hun72] S. Hunklinger, W. Arnold, S. Stein, R. Nava, K. Dransfeld, Phys. Lett. **42** (1972) 253.

[Hun74] S. Hunklinger, Proc. Ultrasonic Symp. (IEEE) (1974) 443.

[Hun76] S. Hunklinger, W. Arnold, in Physical Acoustics **12**, Ed.: R. N. Thurston, W. P. Mason, Academic Press, New York (1976) 155.

[Hun77] S. Hunklinger, *Adv. Solid State Physics XVII*, Ed.: J. Treusch, Vieweg, Braunschweig (1977) 1.

[Hun86] S. Hunklinger, A. K. Raychaudhuri, *Progress in Low Temperature Physics, Vol. IX.*, 1986, Elsevier, Amsterdam.

[Hun94] S. Hunklinger, *Festkoerperphysik, Notizen zur Vorlesung, WS 94/95*, Universitaet Heidelberg (1994).

[Iko91] E. Ikonen, H. Seppae, W. Potzel, C. Schaefer, Rev. Sci. Instrum. **62** (1991) 441.

[Kue03] R. Kuehn, Europhys. Lett. **62** (2003) 313.

[Jae72] J. Jaeckle, Z. Phys. **257** (1972) 212.

[Kin62] L. E. Kinsler, A. R. Frey, *Fundamentals of Acoustics*, John Wiley & Sons, New York (1962).

[Kle87] R. N. Kleiman, G. Agnolet, and D. J. Bishop, Phy. Rev. B **36** (1987) 6551.

[Lay00] M. Layer, Diplomarbeit, Universitaet Heidelberg (2000).

[Las75] J. C. Lasjaunias, A. Ravex, M. Vandorpe, S. Hunklinger, Solid State Commun. **17** (1975) 1045.

[Liu01] X. Liu, S. F. Morse, J. F. Vignola, D. M. Photiadis, A. Sarkissian, M. H. Marcus, B. H. Houston, Appl. Phys. Lett. **78** (2001) 1346.

[Lus01] C. P. Lusher, J. Li, V. A. Maidanov, M. E. Digby, H. Dyball, A. Casey, J. Nyeki, V. V. Dmitriev, B. P. Cowan, and J. Saunders, Meas. Sci. Technol. **12** (2001) 1.

[Mau96] E. Mauceli, Z. K. Geng, W. O. Hamilton, W. W. Johnson, S.Merkowitz, A. Morse, B. Price, N. Solomonson, Phy. Rev. D **54** (1996) 1264.

[Neu03] M. Neumann, Diplomarbeit, Universitaet Heidelberg (2003).

[Pai74] H. J. Paik, Ph.D, Dissertation, Stanford University (1974).

[Phi72] W. A. Phillips, J. Low Temp. Phys. **7** (1972) 351.

[Phi81] W. A. Phillips (ed.), *Amorphous Solids - Low Temperature Properties*, Topics in Current Physics . Phys. **24** Springer, Berlin Heidelberg New York 1981.

[Pob92] F. Pobell, *Matter and Methods at Low Temperatures*, Springer Verlag, Heidelberg (1992).

[Rab86] T. Rabenau, Dissertation, Universitaet Heidelberg (1986).

[Rad71] V. Radhakrishnan, V. L. Newhouse, J. Appl. Phys. **42** (1971) 129.

[Ray84] A.K. Raychaudhuri, S. Hunklinger, Z.Phys.**B57** (1984) 113.

[Ric97] F. Ricci, A. Brillet, Annu. Rev. Nucl. Part. Sci. **47** (1997) 111.

[Rou85] M. L. Roukes, M. R. Freeman, R. S. Germain, R. C. Richardson, M. B. Ketchen, Phys. Rev. Lett. **55** (1985) 422.

[Sku54] E. Skudrzyk, *Die Grundlagen der Akustik*, Springer Verlag, Berlin (1954).

[Sol94] N. Solomonson, W. O. Hamilton, W. Johnson, Rev. Sci. Instrum. **65** (1994) 174.

[Sto95] J. T. Stockburger, M. Grifoni, M. Sassetti, Phys. Rev B **51** (1995) 2835.

[Str61] R. E. Strakna, Phys. Rev. **123** (1961) 2020.

[Str98] P. Strehlow, C. Enss, S. Hunklinger, Phys. Rev. Lett. **80** (1998) 5361.

[Vuk72] M. R. Vukcevich, J. Non-Cryst. Solid **11** (1972) 25.

[Wei95] R. Weiss, Dissertation, Universitaet Heidelberg (1995).

[Whi95] B. E. White, Jr., R. O. Pohl, Phys. Rev. Lett. **75** (1995) 4437.

[Wue94] A. Wuerger, Z. Phys. B **94** (1994) 173.

[Wue95] A. Wuerger, Z. Phys. B **98** (1995) 561.

[Wue97] A. Wuerger, *Springer Tracts in Modern Physics*, Vol. 135, Springer Verlag, New
         York (1997).

[Yu88]   C. C. Yu, A. J. Leggett, comments Condens. Matter Phys. **14** (1988) 231.

[Zel71] R. C. Zeller, R. O. Pohl, Phys. Rev. B **4** (1971) 2029.

Thanks

I would like to thank all the people who have supported me while I pursued my doctor project. In particular I would like to express my thanks to

- Prof. Dr. Siegfried Hunklinger for offering me the opportunity and the means to perform this exciting project in his research group. I thank him for the support and advice that he has provided. His passionate research attitude impressed me very much.

- Prof. Dr. Christian Enss for his encourage and interest in my project, in particular at the beginning of my work. His suggestions and experience were an assistance in the development of the inductive detection technique.

- Dr. Andreas Fleischmann for his introduction to the SQUID and for providing constant guidance throughout the project. His highly effective ideas facilitated the solution of many problems.

- Dr. Marc Layer for extremely pleasant co-operation during three years. I learned much practical knowledge about cryogenics and glass physics from him. On a large extent my success is due to his patience and experience. In addition I would like to thank for his support during the measurements as well as the critical revision of the manuscript.

- Dipl. Phys. Astrid Netsch for the measurements with the novel type of noise thermometer and the helpful discussion about the temperature calibration.

- Dr. Markus Heitz for his guidance of my work in the first one and a half year. Although he was not member of our group anymore, he still answered my questions as soon as possible.

- Dr. Hsin-yi Hao for her permanent suggestions and discussions during my experiments.

I thank our current laboratory colleague Marc Layer, Astrid Netsch and Andreas Rost for the pleasant research atmosphere in our laboratory. By discussing with them, I improved my physical experimental skills and enriched my knowledge a lot.